Volatile Bubble Resorption in Silicate Melts & Magmas via Diffusive Mass Transfer

JACKSON, LUCY,EMMELINE

Volatile Bubble Resorption in Silicate Melts & Magmas via Diffusive Mass Transfer

A numerical and observational study of volcanic and analogue systems

Lucy Emmeline Jackson

Department of Earth Sciences,
Durham University
2022

A thesis submitted in fulfilment of the requirements
for the degree of Masters by Research (MScR) in Volcanology.

Abstract

Bubble growth in magmas is a first-order control on volcanic eruption style, with changes typically resulting from re-equilibration in non-isothermal-isobaric conditions, or diffusive mass transfer of volatiles across the bubble interface. The latter process is well understood for bubbles coupled to high-viscosity liquids such as rhyolitic magmas associated with Plinian and Dome-forming eruptions, but two significant gaps remain: (1) changes to decoupled bubbles in lower viscosity fluids like basaltic magmas typical of Hawaiian or Strombolian eruptions, and (2) bubble resorption and magma regassing resulting from reverse volatile mass transfer into the magma.

Using two new definitions of Péclet number for coupled and decoupled bubbles (Pe_s and Pe_b), and Sherwood number (Sh), these two complexities are explored through the relative timescales of diffusion and advection in analogue and magmatic bubble-melt. Numerical simulations find that in basaltic systems, spherical bubbles are almost always decoupled with resorption limited by diffusion ($\mathrm{Pe}_b \gg 10^5$ or Sh>10), meaning they resorb at the rate of diffusive mass transfer. By contrast, spherical bubbles in rhyolitic melts have restricted buoyancy making them coupled and their resorption limited by the high melt viscosity ($\mathrm{Pe}_s \ll 10^5$). In both melt compositions, resorption of the smallest bubbles ($R_0 < 1\mu$m) becomes limited by surface tension effects.
Experimental observations of decoupled bubbles show that larger bubbles described by high values of Pe_b resorb at a faster rate than smaller bubbles in lower Pe_b systems. This is attributed to larger bubbles rising faster to continually encounter new melt with a renewed concentration gradient.

These findings have great significance to the modelling of eruptive volcanic processes, providing support for theories on the formation of bubble-free material, or dynamic magma regassing. Whilst a numerical model for decoupled bubble resorption in magmas is not yet complete, this thesis quantifies the onset of different bubble regimes for magmas of contrasting compositions.

Table of Contents

Statement of Copyright

Acknowledgements

First and foremost I must thank my primary supervisor Fabian Wadsworth. It has been a pleasure to work with you, not just this year but previously for my undergraduate work too, which helped capture my interest to pursue this research project. I have learned so much from you, from how to approach complex numerical problems and thinking about things in a whole new way, to writing in a much more eloquently, and knowing the only acceptable drink to order in Whitechurch. Also, my secondary supervisor Ed Llewellin, who's knowledge of a vast range of volcanological topics sometimes seems endless. Thank you for all your support and guidance this year, especially with navigating the world of experimental work.

Thanks must go to the Durham University Department of Earth Sciences and University College for awarding me the Stephen Mills Studentship and Pemberton Scholarship respectively. Completing this research whilst exiting a world of pandemics and lockdowns provided significant challenges, but with this funding I was still able to gain a huge range of invaluable experiences, highlights of which include presenting at EGU22 in Vienna and taking my undergraduate work to publication.

Next, a thank you to the wider volcanology reseacrh group at Durham University. I will miss the weekly Volc Coffee discussions that help to see the place of your work in a wider context, and seeing the exciting work that everyone gets up to. As well as this there is the extended postgraduate community in Durham Earth Sciences (Honor, Madeleine, Janina, Annabelle, Elouise, Bex and Sean to name just a few!).

Finally I must thank my wider Durham network and those even beyond that, including my close family, for always supporting me through the ups and downs. Research really is a roller-coaster ride, even in just this twelve month taster of a research Masters. I really am thankful for them being able to pick me up and encourage me even when all seems lost and the challenges insurmountable.

I have loved working on this project, being able to build my knowledge of the subject far beyond what I imagined when starting out. Armed with plenty of other skills from the learning opportunities of this year, I am moving onto pastures new, but there will always be a place in my heart for volcanoes, and even more so for Durham.

Thesis Rationale & Structure

The work presented in this thesis aims build upon previous studies of bubbles in highly viscous fluids by Hadamard (1911), Rybczynski (1911), Doremus (1960), Pigeonneau (2007; 2009; 2011), McIntosh (2013; 2014) and Pereira et al. (2020), to name but a few. This wide collection of work has already provided many solutions and models for bubble behaviours and dynamics, including bubble nucleation, coalescence and rise. The latter has most recently been developed for non-isothermal systems in a paper written in conjunction with but distinct separation from this thesis *(Jackson et al., 2022)*. Work on this type of bubble system is included in discussion for completeness but is by no means the primary focus of this study.

More specifically, following examination of the predominant endmember cases for bubbles in viscous fluids, this thesis aims to to gain further insight into the process of bubble resorption, extending the dynamics and consequences of this process to natural volcanic systems. Investigation of this is done through both numerical and observational analysis of the combined advection - diffusion problem in real-world volatile-magmatic melt systems and analogue gas-melt systems.

The work concludes with the presentation of several regime diagrams which it is hoped, can be used to make interpretations about bubble dynamics and resorption in both magmatic melts and other viscous fluids. These diagrams provide an insight into the current understanding of bubble resorption dynamics as well as showing where there is room for significant future work following the completion of this thesis.

Nomenclature

Variable	Notation	Units
System Parameters		
Lengthscale	x	m
Time	t	s
Bubble Radius	R	m
Initial Bubble Radius	R_0	m
Acceleration due to Gravity	g	ms^{-2}
Molar Mass	M_m	-
Gas Constant	R_g	$\mathrm{Jmol}^{-1}\mathrm{K}^{-1}$
Boltzmann Constant	k	$\mathrm{m}^2\mathrm{kgs}^{-2}\mathrm{K}^{-1}$
Jump Distance	l	m
Moles	n	mol
Velocity	u	ms^{-1}
Terminal Bubble Rise Velocity	u_∞	ms^{-1}
Melt Velocity	u_0	ms^{-1}
Melt Density	ρ_m	kgm^{-3}
Bubble Phase Density	ρ_b	kgm^{-3}
Melt Viscosity	μ	Pa.s
Bubble Phase Viscosity	μ_b	Pa.s
Diffusion Coefficient	D	$\mathrm{m}^2\mathrm{s}^{-1}$
Diffusion Lengthscale	L	m
Initial System Pressure	p_0	Pa

Surface Tension	Γ	Nm^{-1}
Melt Solubility	S_0	wt.%
Heating/cooling rate	q	Ks^{-1}
Timescales		
Advective Timescale	λ_A	s
Bubble Rise Timescale	$\lambda_b = \frac{R_0}{u_\infty} = \frac{3\mu}{R_0 g \Delta\rho}$	s
Melt Shell Response Timescale	$\lambda_v = \frac{4\mu}{p_0}$	s
Diffusive Timescale	$\lambda_D = \frac{L^2}{D}$	s
Dimensionless Quantities		
Reynolds Number	$\mathrm{Re} = \frac{u_\infty \rho R_0}{\mu}$	-
Eötvös Number	$\mathrm{Eo} = \frac{R_0^2 g(\rho_b - \rho)}{\Gamma}$	-
Density Ratio	$\Pi_b = \frac{\rho_b}{\rho}$	-
Morton Number	$\mathrm{Mo} = \frac{Eo^3}{Re^4}$	-
Stokes Number	$\mathrm{Stk} = \frac{u_\infty}{u_0} = \frac{R_0^2 g \Delta\rho}{u_0 \mu}$	-
Péclet Number	$\mathrm{Pe} = \frac{\lambda_D}{\lambda_A}$	-
Buoyant Péclet Number	$\mathrm{Pe}_b = \frac{\lambda_D}{\lambda_b}$	-
Stationary Péclet Number	$\mathrm{Pe}_s = \frac{\lambda_D}{\lambda_v}$	-
Sherwood Number	Sh	-

List of Figures

List of Tables

The earth has bubbles, as the water has,
And these are of them.
- Macbeth I.III -

Introduction

Volcanoes and eruptive products have had a huge impact on the world around us over geological time. From the proposed role of volcanic vents in the origins of life, providing vital energy and nutrients for growth in the early oceans *(Corliss et al., 1981; Martin et al., 2008)*, to acting as the major delivery mechanism of stored gas species to Earth's atmosphere *(Dasgupta, 2013; Brune et al., 2017; Fischer et al., 2019)*, the ability of volcanoes to influence our world means they have long captured the imagination of the public and scientific communities alike. The subsurface processes that drive volcanic eruptions are often impossible to observe, leaving many questions in the field of volcanology unanswered or open to wide interpretation. Volcanologists must instead make use of erupted products or surface level observations to try and understand the sequence of subsurface processes that occur in the build-up to an eruption.

The dynamics of magmatic melts and their interaction with gases in the plumbing system is thought to be pinnacle to understanding how volcanic eruptions vary in style and evolve over time *(Sparks, 1978, 2003; Gonnermann and Manga, 2007)*. These interactions and transitions between gaseous and melt phases have the ability to affect both the material and chemical properties of magma, thus promoting or impeding its ascent and ultimately altering the eruptive behaviour of the volcano *(Woods and Koyaguchi, 1994; Dingwell, 1996; Edmonds and Herd, 2007; Castro et al., 2012; Oppenheimer et al., 2018; Mittal and Richards, 2019)*.

Gas-melt interactions also represent a key control on the emission of gases into Earth's atmosphere, as the ability for a dissolved gas to be held within a melt changes over time as conditions within the volcanic system change. As a result, gas species are able to outgas (exsolve) from the melt phase to nucleate a bubble phase which can then decouple from the degassed melt and, driven by density and pressure differences, rise though the system towards the surface. This is one of the key processes that makes volcanoes the primary natural delivery method of gases to Earth's atmosphere, accounting collectively for several hundred mega-tonnes of gas emissions each year *(USGS, 2018, 2019; Halmer et al., 2002; Kilbride et al., 2016)*.

This work aims to investigate the micro-physics behind a single aspect of volcanic gas-melt interactions: the ascent and volume change of bubbles formed in magma via exsolution. In particular, the possibility for a bubble to be resorbed either when stationary or moving dynamically through magma. This concept is currently considered by very few in the field of

volcanology, despite there being evidence for its occurrence in basaltic *(Carey et al., 2013; McIntosh et al., 2014)* and rhyolitic systems *(Yoshimura and Nakamura, 2008, 2010; Watkins et al., 2012)*. The potential significance bubble resorption has to influence chemical or rheological alterations to magma could notably change eruptive style or evolutions, warranting a need to develop understanding in this area.

1.1 Volcanic Gas-Melt Systems

Surface-level observations show there is a vast range in the style and products of volcanic eruptions around the world. Some volcanoes produce effusive, foamy lava eruptions *(Jaupart and Vergniolle, 1988; Vergniolle and Jaupart, 1990)* whereas others give extremely explosive eruptions fuelled by the dynamics of rapid and extensive bubble nucleation and growth *(Burgisser and Degruyter, 2015)*. Some even display aspects of both, such as effusive eruptions interrupted by sudden explosive bursts, or initially explosive eruptions decaying away to be more effusive and long-lived *(Pallister et al., 2013; Swanson et al., 2014)*. These differences and evolutions in eruptive style occur as a direct result of gas-melt interactions as mass and heat are transferred between the two phases, influencing magma properties and the dynamics of the wider volcanic system they sit within *(Burgisser and Degruyter, 2015; Castro and Gardner, 2008)*.

1.1.1 Gas-Melt Interactions

At depth, all magmas contain dissolved volatile species in varying quantities. These volatiles are typically water (H_2O), carbon dioxide (CO_2) and sulphur (mainly as SO_2 or H_2S), although several other species can also be removed from the melt as a gaseous phase, such as the hydrogen halides (HCl, HF and HBr). Under the right conditions, volatiles are able to migrate out of the melt to nucleate a bubble phase, evidence for which is observed at the surface during eruptions or preserved in ejected materials like pumice or scoria. Volcanologists use these observations to hypothesise the different processes that must occur to take these dissolved volatiles out of the melt and up through the system as a bubble phase to be released at the surface or captured within erupted material.

1.1.1.1 Exsolution of Bubbles

The process by which dissolved volatiles are removed from a melt to form a bubble phase is exsolution: the separation of a previously homogeneous phase into two or more phases without the removal of material. In volcanic systems, exsolution has the potential to affect the properties of the remaining magma and as exsolution acts to reduce that supersaturation toward equilibrium. This chemical alteration could impact further interactions the magma has with other material as it moves within the volcanic system. Followng exsolution, the system contains two (or three) physically distinct phases; a gaseous bubble, a liquid melt and depending on conditions a solid crystal phase, creating a multi-component magma that will behave dynamically differently to a bubble-free melt.

1.1.1.2 Degassing & Outgassing

In lower viscosity basaltic melts, once bubbles are exsolved from the melt phase, the density contrast with the magma means they are able to rise buoyantly in the process of closed-system degassing *(Colombier et al., 2021)*. The rate of this bubble rise depends most significantly on the size of the bubble and viscosity of the surrounding melt. If sufficiently large enough or in a low-enough viscosity melt, a bubble will be able to rise free of the magma it exsolved from. The bubble is then able to re-distribute both mass and heat (gas sparging) around the volcanic system as it moves between different magma stores *(Bachmann and Bergantz, 2006; Annen et al., 2008; Dungan et al., 2010; Edmonds and Wallace, 2017)*. The magma left behind by the rising bubble would also become denser over time due to the removal of the buoyant bubble phase. This denser, bubble-free magma might then sink within the system to greater depths where temperatures increase, sparking processes such as magma cycling via convection currents. If a degassing bubble rises significantly close to the surface, open-system degassing may take place. The gas held within the bubble is then expelled into the atmosphere, a process referred to as outgassing.

In higher viscosity rhyolitic melts, outgassing takes place via a different mechanism. Exsolved bubbles grow within the melt until they become large enough that they interact and connect up to form a bubble network. Inter-connectivity of this bubble network then allows gas to rise buoyantly upwards towards the surface to be outgassed into the atmosphere. This mechanism doesn't require any bubble buoyancy or convection of melt.

1.1.1.3 Bubble-Melt Coupling

In natural magmatic systems, the magma surrounding the bubble might also be migrating upwards in conjunction with the bubble. Therefore, the degree to which bubbles and magma in natural systems are coupled needs to be considered. Coupling describes the relative motions of two phases, with two end-member scenarios: coupled and decoupled. In this case, it describes the relative ascent velocities of rising bubbles and magma in a volcanic system *(Gonnermann and Manga, 2013)*.

1. Coupled Bubbles
   When bubbles and the surrounding magma move with the same or very similar ascent rate, they are said to be coupled. This means the relative velocity of the two phases is close to zero.

2. Decoupled Bubbles
   When bubbles rise much more rapidly than the surrounding magma, they are described as being decoupled or separated. The relative ascent velocity of the phases is much greater than zero.

There are numerical limits for the formation of a decoupled system that can be defined using the dimensionless Stokes number (Stk); the ratio of bubble rise velocity to melt ascent velocity, where Stk$<<$ 1 indicates a coupled system and Stk$>>$ 1 a decoupled system. Detail on the mathematical definition of Stokes number is outlined further in **Section 2.1.2**. The large variety in dynamics of natural volcanic systems means they are described by a wide range

of Stokes number values, with it being most significantly influenced by bubble size and melt composition *(Degruyter et al., 2012; Gonnermann and Manga, 2013; Mader et al., 2013)*.

1.1.1.4 Coupling & Eruptive Style

The degree of bubble-melt coupling influences the eruptive style of a volcanic system *(Degruyter et al., 2012; Mader et al., 2013)*. Surface observations show there are variable outputs of magmatic material and gases from different volcanoes, with some eruptions being extremely gas and material rich but others varying between gas dominant or material dominant. This hints to the interactivity between the gases and magma prior to eruption that occurs to create this spectrum of activity.

Figure 1.1 shows different regimes of eruption style derived from functions of magma ascent rate and viscosity for a wide range of volcanic systems, from low-viscosity basalts through to high-viscosity, silicate-rich rhyolites. Envelopes for several transitional processes are also shown, including that for the onset of a decoupled (separated) flow for the size of bubble typically found in natural systems. This envelope marks the divide between coupled and decoupled natural bubble-melt systems, indicated by the respective blue and red regions on the figure. **Figure 1.1** therefore provides numerical evidence of the link between the degree of bubble-melt coupling and the eruptive style observed for a volcano.

Explosive Plinian eruptions are associated with coupled systems, where high-viscosity melts rise very rapidly, limiting the degree of outgassing prior to eruption. Any gases exsolved to bubbles cannot then move freely of the melt, meaning the limit on bubble exsolution is reached quickly and the surrounding magma becomes supersaturated in volatiles. This results in processes such as brittle fragmentation and the formation of large gas slugs that rise alongside extremely viscous melt to produce highly explosive eruptions. The 1980 eruption of Mount St. Helens, USA was thought to have been fuelled by processes such as this *(e.g. Sparks, 2003; NASEM, 2017)*.

More effusive eruptions such as Hawaiian or weak Strombolian are associated with decoupled systems, where lower-viscosity magmas ascend several orders of magnitude slower through the volcanic system. Consequently, it is much easier for exsolved bubbles to degas through the low-viscosity melt, and there is much more time for these bubbles to outgas at the surface. As a result, the bubbles and melt are decoupled. These Strombolian eruptions tend to produce high levels of gas emissions at the vent (10^2-10^4 m^3s^{-1} *(Greenland et al., 1985; Del Bello et al., 2012; Ishii et al., 2019)*) and emit material much more effusively, such as in the 1983 eruption of Kilauea, Hawaii *(e.g. Swanson et al., 2014; NASEM, 2017)*.

The work in this study looks at bubble-melt processes in a wide range of natural magmatic systems, from basaltic to rhyolitic composition, in order to better understand the similarities and differences in bubble dynamics such melts. As **Figure 1.1** demonstrates, large variation in magma viscosities and ascent velocities means both basaltic and rhyolitic magma systems sit on both sides of the separated flow envelope. Consequently, the bubbles and melt can be coupled to varying degrees, which is taken into account in analysis throughout this study in addition to exploring the implications of coupling on bubble resorption.

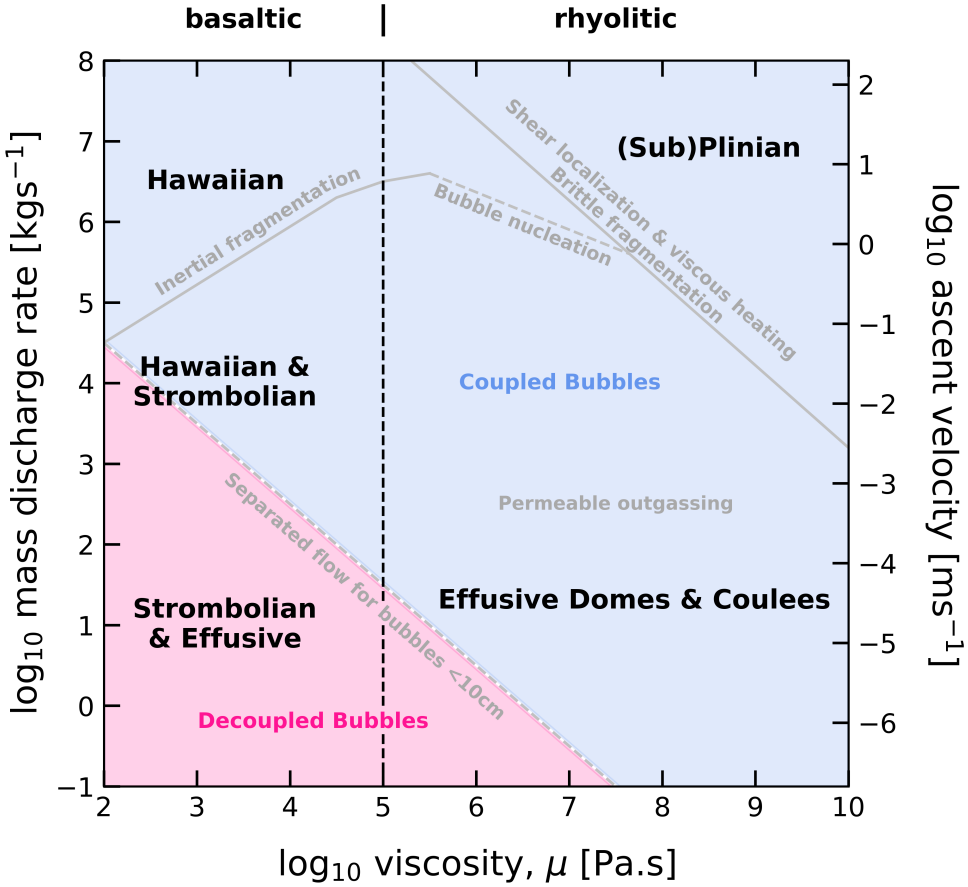

Figure 1.1: Adapted from Gonnermann and Manga *(2013)* and NASEM *(2017)*. Eruptive regimes of volcanic systems represented as functions of magma ascent velocity, discharge rate and viscosity. Envelope lines in grey dictate the onset of several transitional processes including brittle fragmentation, bubble nucleation and outgassing. The envelope for the onset of a separated flow is also shown, marking the divide between coupled bubble systems (blue shaded region) and decoupled bubble systems (red shaded region). The regimes of interest in this work, in basaltic melts, are shown by the purple shaded region to the left of the black dashed line. This region contains a range of different eruptive regimes with both coupled and decoupled systems present.

1.2 Bubble Growth & Resorption in Volcanic Systems

In natural volcanic systems, it is widely accepted that volatile bubbles nucleate from magma at depth. This occurs as the surrounding pressure at depth is much greater than at the surface due to the weight of material sitting above (magmastatic overburden).

Once nucleated, bubbles can undergo growth or shrinkage as a result of changes to the physical conditions of the system, or chemical processes such as diffusion. Since the presence of bubbles can affect the buoyancy of a magma, its ascent velocity within a volcanic system and therefore the eruptive dynamics at the vent *(Sparks, 1978; Gardner et al., 1999; Degruyter et al., 2012)*, it is important to understand how bubble sizes evolve in various magma compositions and system conditions.

1.2.1 Growing Bubbles

Isolated bubbles suspended in any fluid will grow if there is a reduction in pressure of the surroundings, referred to as decompressive expansion. This reduction in pressure is

experienced in volcanic systems if (1) the bubble rises from depth to a shallower, lower pressure region, or (2) if the system becomes open to atmospheric pressure for example during an eruptive phase.

In both cases, the initial gas pressure of the bubbles is in equilibrium with the surrounding fluid. As surrounding pressure then drops, the gas within the bubbles becomes overpressured to the point that the gas will expand to try and re-equilibrate with the fluid pressure.

The latter case described above, where bubbles are exposed to an open-system and atmospheric pressure, is observed for a volcanic setting in the inflation of connected bubble networks in pumices, pyroclatics and rhyolitic flows *(Shea et al., 2012; Manley and Fink, 1987)*. Interconnectivity from the coalescence of multiple bubbles provides channels for degassing straight to the surface and a sudden drop in pressure that causes bubbles in the network to expand and coalesce further. This process has been observed in natural samples and recreated experimentally in various decompression experiments *(eg. Westrich and Eichelberger, 1994; Shea et al., 2012)*. However, the relevance of this bubble expansion case to this study is limited due to it involving multiple interconnected bubbles as opposed to singular, isolated bubbles.

The former case, where singular bubbles are rising within a system is more relevant to the work of this study. Described as ascent-driven decompression *(Gonnermann and Manga, 2007)*, it has been very well studied for volatile bubbles in various compositions of magmatic melt. Decompression experiments *(Westrich and Eichelberger, 1994; Liu and Zhang, 2000; McIntosh, 2013; McIntosh et al., 2014; Ryan et al., 2015; Coumans et al., 2020)* where samples of bubble-baring volcanic material are subjected to pressure or temperature changes at varying rates have shown that bubbles will expand or contract in line with gas laws.

Analytical *(Prousevitch et al., 1993; Lensky et al., 2004)* and numerical *(Huber et al., 2014; Coumans et al., 2020)* bubble growth models, validated by the experimental results, have been developed to give models for bubble radius evolutions in non-isothermal and non-isobaric conditions. These models are also applicable to the scale of natural systems meaning they are useful in developing understanding of bubble dynamics and the effects of these on wider volcanic processes.

A second mechanism by which bubbles in a magmatic system may grow is through the transfer of mass from dissolved volatiles in the melt to a gas phase within the bubble. This process is driven by a difference in concentration between the surrounding melt and bubble gas composition. If the surrounding magma is sufficiently oversaturated in a volatile species, there will be a large concentration gradient with the bubble. As a result, the volatile species will move down the concentration gradient, and transfer diffusively into the bubble. The additional mass now contained within the bubble then has to be equilibrated by a volumetric growth in line with gas laws, observed as an expansion of the bubble.

Models now begin to take this additional mass transfer growth mechanism into account *(Prousevitch et al., 1993; Blower et al., 2001; Chernov et al., 2018; Coumans et al., 2020)* to allow for a much more complete model of bubble evolutions. The most recent study by Coumans et al. (2020) builds upon and experimentally validates the solution by Blower et al. (2001) for

bubble growth in magmatic melts that accounts for both pressure-temperature changes, mass transfer and the secondary effects of mass transfer on the surrounding melt. These secondary effects are changes to physical properties such as melt viscosity and density as a result of mass being removed. They successfully show through their model and accompanying experiments on vesicular rhyolite from Hrafntinnuhryggur, Krafla (Iceland), that diffusion of water across the boundary of a bubble will firstly result in its growth, and secondly increase the viscosity of the remaining melt as H_2O is removed from its composition. More widely, their results again demonstrate the interconnectivity of bubble and melt dynamics and confirm that changes to bubble size must be considered alongside changes to magma properties if comprehensive models of volcanic systems are to be developed.

1.2.2 Shrinking Bubbles

A less widely explored idea in volcanology is that of bubble resorption, mainly due to it requiring the timescale for resorption to be faster than that for decompressive expansion, as highlighted by Gardner et al. (2019). Understanding the role and impacts of resorption in these settings could help explain some of the volcanic phenomena observed.

1.2.2.1 Shrinking or Resorbing?

As with bubble growth there are several mechanisms by which bubbles may shrink within a fluid, principally being (1) when pressure-temperature conditions change such that the gas volume shrinks in line with gas laws in response, or (2) when pressure-temperature changes induce diffusion of the gas back into the melt by changing the saturation state of the melt resulting in bubble resorption. It is likely that these two processes could occur simultaneously, however case (1) may also be able to occur in isolation.

It is important to highlight here the difference between a shrinking bubble and a resorbing bubble. Shrinking bubbles merely change size without there being any transfer of mass between the bubble and fluid. This is most likely observed in case (1), where a gas is insoluble with the fluid and simply expands or contracts in response to pressure or temperature changes to achieve equilibrium with the surroundings.

In a slightly more complex scenario, bubble shrinkage without distinct resorption is observed in the Ostwald ripening of bubbles *(Ostwald, 1896; Markworth, 1985; Stevenson, 2010; Huang et al., 2017)*, where smaller bubbles shrink and transfer mass diffusively into larger bubbles via the fluid in order to enable the growth of the larger bubbles. This process has been observed in a range of fluids including rhyolitic melt *(Lautze et al., 2011)*. Despite the gas species transferring between bubbles by diffusion, here, this process is not considered to be resorption as the overall gas volume fraction remains the same throughout and the gas species is not held within the melt. This work instead chooses to define resorbing bubbles as those that transfer mass diffusively into a fluid where it is then stored as a dissolved species, resulting in a decrease in gas volume fraction as it does so.

For resorbing bubbles (case (2)) where pressure and temperature are changing, the rate of mass transfer and therefore bubble shrinkage is controlled by changes to solubility of the gas species with the fluid. A higher solubility means the fluid is more able to accommodate the

mass from the bubble so that resorption is more likely. For magmas, pressure-temperature changes can alter solubility by several orders of magnitude, making it a major control on the plausibility of volatile bubble resorption **(see Section 2.3.1.3)**. Whilst dramatic changes to pressure that would favour a solubility increase are unlikely in natural systems, changes to temperature as material is erupted or moves between stores in the volcanic system, could generate a scenario where solubility increases to promote bubble resorption.

In both cases 1 and 2, the shrinkage of a bubble must be accommodated by motion of the melt into the space left by either the volume change of the gas (case 1), or the removal of mass of gas from the bubble (case 2). Therefore, an important consideration on top of the equation of state of the gas phase and the solubility of the gas phase is the relative ease with which the melt can move, controlled significantly by the viscosity of the melt. Therefore, it is clear that shrinking bubbles are controlled by a range of inter-linked processes that need to be understood both individually and collectively in order to understand this process.

For a volcanic system, the resorption of volatiles into a magma (or regassing) via any mechanism would have profound impacts on both the chemical and physical properties of the magma. By extension, this re-gassed magma could have altered dynamic behaviours as an increased volatile content and reduced bubble volume would affect properties like density, viscosity, and compressibility.

1.2.2.2 Studies of Resorbing Bubbles

Resorption of bubbles has been extensively researched in non-magmatic silicate melts and molten glasses *(Greene and Gaffney, 1959; Greene and Kitano, 1959; Žlutický and Němec, 1977; Pereira et al., 2020)* due to its significance to industrial processes and glass manufacture, where bubbles need to be removed to produce 'flawless' materials. Alongside experimental observations, Doremus *(1960)* developed an analytical solution from bubble dynamic theory to describe the observed resorption of apparently stationary oxygen bubbles and silicate glass. Cable & Frade *(1986)* later presented several further, more general analytical solutions for the controlled growth and dissolution of spheres in viscous fluids. An extension of these ideas on stationary, resorbing bubbles forms the focus of **Chapter 5** in this work where application to magmatic melts is also made.

More recently, numerical investigations have also been completed *(Pigeonneau, 2007, 2009, 2011)*, to produce a numerical model for buoyant bubble resorption with simultaneous redox reactions. Tested against experimental observations of a resorbing oxygen bubble in an iron-doped silicate melt, the scenario dexcribed by this model is much more complex, as the dynamics of the decoupled bubble have to be combined with the diffusive mass transfer process to achieve a complete model. The idea of decoupled, resorbing bubbles forms much of the work presented in **Chapter 6** of this study where again it is extended to consider magmatic melt systems.

Investigations of bubble resorption in magmatic melts or glasses are less extensive, but two experimental studies have been able to such direct observations. Yoshimura & Nakamura *(2008)* used an open degassing system to look at the resorption of water into highly-silicic

rhyolitic obsidian from Wada Pass, Japan. They found the applied pressure difference resulted in bubble resorption along the margins of the obsidian samples.

Further similar work *(Yoshimura and Nakamura, 2010)* looking at the relative movements of H_2O and CO_2 found that H_2O diffused rapidly from the bubble into the undersaturated melt causing shrinkage; but then CO_2 in the melt began to diffuse in the opposite direction, into the bubble. Therefore, the initially observed bubble shrinkage was only temporary on the timescale of their experiments and didn't result in complete resorption. Watkins et al. *(2012)*, studied the concentration of H_2O and CO_2 in the material surrounding bubbles in samples of obsidian from Mono Craters, USA. They similarly found an increased concentration of H_2O in the melt directly surrounding the bubbles and attribute this to resorption immediately prior to eruption.

A third study by Carey et al. *(2013)* presents more indirect evidence of bubble resorption from erupted clasts. Basaltic clasts from the 2008 eruption of Lake Halema'uma'u, Kilauea, Hawaii, show distinct 'haloes' of high water concentration around bubble edges, indicating that water had transferred diffusively back into the melt during its downwards convection.

Each of these three studies attribute the resorption of volatiles to be principally driven by pressure changes; either from open-system degassing or movement of material to different depths. In each case, an increase in pressure results in an increase in solubility of the species to the melt, enabling it to undergo diffusive mass transfer observed as bubble resorption. von Aulock et al. (2017) and Weaver et al. (2022) Weaver more recently explained processes of bubble resorption to be driven by pressure differences between the bubble and surrounding melt, rather than just the effects of pressure on solubility. This is of particular significance when describing processes of outgassing, where bubbles may experience extreme pressure contrasts.

McIntosh *(2013; 2014)* alterantively begins to explore the role of temperature changes on bubble resorption in magma. They observe partial resorption of water from bubbles into volcanic glasses. This resorption mainly occurs above glass transition, when the magma is still mobile, but increases during rapid cooling (quenching) of the glass due to solubility of H_2O with the glass increasing with decreasing temperature.

Collectively, this previous work demonstrates that bubble resorption in both highly-viscous non-magmatic and magmatic systems is possible, and that it is mainly driven by changes to solubility as a result of variations in the surrounding conditions. They also each make the case for using observations of bubble resorption as a tool for reconstructing pre-eruptive conditions or eruptive histories. However, something not yet considered is the potential for volatile bubbles to resorb whilst simultaneously moving within a wider magmatic system. Building on the work by Yoshimura & Nakamura *(2010)*, this could mean that rising bubbles consistently encounter different magma compositions, some of which may be undersaturated in volatiles. As a result, bubbles may undergo complete resorbtion to re-gas the melt.

1.2.3 Secondary Effects of Bubble Resorption

Evidence of the chemical changes to surrounding melt composition that result from resorption from these previous studies *(Watkins et al., 2012; Carey et al., 2013; McIntosh, 2013; McIntosh et al., 2014)* justify why the wider impacts of bubble resorption on the dynamics of volcanic systems need to be hypothesised on. If coupled with the potential for bubbles to rise buoyantly through a volcanic system, it may be that these bubbles are repeatedly recycled around the volcanic system in cycles of exsolution, degassing and regassing. On a large enough scale, such cycling will enable the transfer and re-distribution of mass and heat within the plumbing system, which could bring the potential to trigger an eruption. The extreme significance of these re-distributions to existing models of volcanic dynamics and the ability to explain several volcanic phenomena is something this work aims to explore. Here, some of the potential secondary effects of bubble resorption and magma re-gassing are described in more detail.

1.2.3.1 Melt Density

On the scale of a body of magma, bubble resorption via diffusive mass transfer will reduce the bubble volume fraction of a magma and thus produce a denser melt packet. If instead the melt is considered on a smaller, more individual scale, an increased proportion of volatiles will decrease the melt density *(Wallace and Anderson, 1999)*. CO_2, due to its greater molecular weight, reduces the density of melt to a lesser degree than H_2O, but either way, melt regassed with volatiles will have a lower density than a degassed melt. However, overall, the larger-scale density increase from the loss of buoyancy will be more significant than the density decrease due to compositional changes, and therefore regassed magma is likely to be denser than degassed magma.

Considering this in a wider context, denser regassed magma has the potential to overturn and sink down to greater depths where pressure and temperature are increased. Overturn of magma like has the potential to establish convection cycles. Such cycles are thought to be associated with unusually high gas emissions from some deep chamber volcanoes (eg. Strobmoli, *Stevenson and Blake (1998)*), and it has been suggested that if able to take place on a large scale, convective overturn could be enough trigger an eruption of the volcano *(Yoshimura and Nakamura, 2010)*. This links a potential secondary effect of bubble resorption to surface-level phenomena observed at several different volcanoes.

1.2.3.2 Melt Viscosity

The viscosities of magmas can vary over fifteen orders of magnitude and are significantly affected by both temperature and composition *(Dingwell, 1996; Gonnermann and Manga, 2013)*. Magmas display an inverse temperature-viscosity relationship, with melts at high temperatures having a lower viscosity in comparison to those at low temperatures. Considering the potential that bubbles within a volcanic system have to transfer heat via gas-sparging as well as mass, suggests that regassed magmas can gain heat and as a result, decrease in viscosity.

Magma viscosities are also heavily sensitive to dissolved volatile content, especially dissolved

H_2O due its interaction with the molecular framework of a magma. Increasing H_2O in the melt composition by just a few weight percent can decrease magma viscosities by several orders of magnitude *(Hess and Dingwell, 1996)*.

In the context of magma regassing, the combined effects of heat and volatile mass transfer from a resorbing bubble would reduce the viscosity of a magma as a secondary effect. Consequently, the regassed magma would be much more mobile, and could have different dynamic behaviour that would add to explanations of the different eruptive styles observed ay volanoes around the world.

1.2.3.3 Magma Compressibility

The volume of an exsolved bubble phase within a degassed affects the magma's compressibility. Described by the 'magma sponge' model, an increased bubble volume increases compressibility of the magma, allowing it to expand or contract with relative ease in response to fluxes of material within the volcanic system *(Voight et al., 2010; Edmonds and Wallace, 2017)*.

Applying this to the context of magma regassing, a reduced bubble volume from bubble resorption would reduce compressibility of the magma. Therefore, the ability of the magma compensate volumetric changes in the volcanic system via expansion or contraction would be limited. At surface level, this may lead to observations such as increased ground deformation prior to and in response to an eruption, as the dynamics of the magma are altered as a secondary effect of bubble resorption.

1.3 Hypothesised Scenarios of Bubble Resorption

Throughout the previous sections, several different volcanic processes or scenarios relating to bubble resorption have been alluded to. Here, scenarios where volatile bubble resorption into magma is plausible are set out more specifically along with thoughts on the potential secondary effects of this resorption. These consequential effects have been scarcely examined in previous literature despite having the potential to significantly impact magma dynamics or the eruptive style of a volcanic system.

The scenarios presented are divided into settings where bubbles are coupled and apparently stationary, and those where bubbles are decoupled and move buoyantly through the melt (similar to **Figure 1.1**). In both cases, the assumption is made that any change to bubble size driven by localized pressure or temperature changes occurs on a timescale much longer than that resulting from diffusive resorption. Secondly, diffusive mass transfer is only considered in a single direction, from the bubble into the melt, whereas in reality, different volatile species may also be transferring into the bubble from the melt phase. Finally, each scenario assumes bubbles are un-coalesced and therefore move and interact with melt independently of one-another to simplify the dynamics discussion.

1.3.1 Coupled Bubble Scenarios

Possible volcanic scenarios for bubble resorption in coupled systems are considered to occur chiefly silicic rhyolitic systems, where melt viscosities are significantly higher than in less silicic (basaltic) systems, restricting bubble rise to result in an apparently stationary diffusion dominated system. The two scenarios outlined in more detail here, both rely on the ability for bubbles to become suspended in very-high viscosity melt following an eruptive degassing event. Such an event leave the melt depleted in volatiles and therefore able to accommodate those from within the suspended bubbles. Therefore, mass is transferred diffusively to regas the highly-viscous magma and the apparently stationary bubbles shrink in response to equilibrate. Under some conditions, the bubbles may be able to undergo complete resorption.

This idea is now applied to two more specific volcanic scenarios where it is plausible that coupled volatile bubbles could undergo resorption via diffusive mass transfer.

1.3.1.1 Foam Collapse

One setting where coupled bubbles are thought to exist in a volcanic setting is in rhyolitic melt following foam collapse. Following this collapses, bubbles can become isolated within a melt with a gas pressure lower than the surrounding magma, and subject to cooling once that would result in the thermal resorption of bubbles as magma solubility would increase with the temperature decrease.

Originally, Eichelberger et al. (1986), suggested that bubble shrinkage and resorption could also occur at this point due to undersaturation of the melt. They proposed that the magma would be undersaturated in volatiles following their removal through the permeable foam. They use this idea to explain observations in nature of completely bubble-free obsidian such as that cored from Obsidian Dome, California (USA). Furthermore, Westrich and Eichelberger (1994) completed a series of high-temperature decompression experiments on pumice samples to show that the re-pressurisation of decompressed rhyolitic foams resulted in a decrease in volume of up to 50% and production of samples that tended towards being bubble-free (Figs.4-5 in Westrich and Eichelberger (1994)).

Despite these results, the foam collapse model and its role in influencing eruption transitions in rhyolitic systems is disputed *(Friedman, 1989; Fink et al., 1992; Castro et al., 2014; Gardner et al., 2017; Wadsworth et al., 2020)*. It is thought that bubble entrapment of collapsed magma foams is more likely to yield material with vesicularity 30vol.% rather than being completely bubble-free. However, bubble resorption could help explain models where completely bubble-free material remains.

1.3.1.2 Welded Pyroclastic Deposits

A second scenario where coupled bubbles could undergo resorption occurs within welded layers of pyroclastic density current (PDC) deposits. These deposits are typically layered with a range of different textures that vary from loose, unconsolidated material to porphyritic with large crystals embedded in a glassy groundmass (vitrophyres). Within a vitrophyre there can be further sequences of material textures including variably vesicular pumice and devitrified

rhyolite glass.

These rhyolite glass (obsidian) pyroclasts often contain low quantities of isolated bubbles formed as material accumulates and welds together *(Sparks et al., 1999; Manley and Fink, 1987)*. As material continues to accumulate the increased lithostatic load on top of the still molten obsidian leads to the shrinkage or complete collapse of bubbles.

Temperature changes could also result in bubble resorption due to an increased solubility of the obsidian glass melt. This idea was first suggested to explain observations of dense, bubble-free obsidian by McIntosh et al. (2014) and has been further investigated by other since *(Gardner et al., 2019; Allabar et al., 2020; Weaver et al., 2022)*. As the PDC cools following eruption, solubility of volatiles into the rhyolitic glass layers will increase by several wt.% *(Newman and Lowenstern, 2002)* leading to the thermal resorption of bubbles as volatiles diffuse into the glass melt *(McIntosh et al., 2014)*.

Gardner et al. (2019) used experimental results and order of magnitude estimates of timescales for diffusion and viscous flow around a bubble to propose that if rapid cooling of the pyroclast took place, the glass would be immobile before any significant diffusion or bubble shrinkage could occur. However, if much slower cooling took place, the time available for diffusion would be much greater and therefore significant enough for thermal resorption of bubbles to occur. They suggest that if cooling was significantly slow enough, volatile bubbles may undergo complete resorption, leaving behind densely welded, bubble-free obsidian. Therefore, resorption of stationary bubbles within cooling PDC deposits is a plausible natural scenario.

1.3.2 Decoupled Bubble Scenarios

In contrast to coupled bubble scenarios, the volcanic systems where resorption of decoupled bubbles is plausible are more likely to be basaltic. This results from bubbles requiring a relatively fast rise velocity, which, whilst not always the case, is more plausible in lower-viscosity basaltic melts. Multiple scenarios are outlined here, each of which applies a similar underpinning process to more specific volcanic settings on various scales. In each case, the decoupled bubbles rise through the systems away from the melt they were exsolved from, to interact with magmas of different compositions. Under certain conditions, the rising bubbles may enter a magma that has been previously degassed and can therefore take up volatiles via diffusive mass transfer. The magma will then be regassed and the bubbles will shrink in response to the removal of volailtes. This process will carry on as the bubble continues to rise through previously degassed magma until the bubble has either undergone complete resorption or is small enough that it is no longer buoyant and therefore no longer decoupled from the magma. At this point, the mass will be transferred until an equilibrium state with the melt is reached.

The following scenarios outline in more detail, volcanic settings where decoupled volatile bubbles could undergo resorption to regas the surrounding magma.

1.3.2.1 Intrusion & Magma Mixing

Magma mixing following intrusion events is known to transfer heat (gas sparging) as well as affect the melt composition and crystal content *(e.g. Sides et al. 2014; Rossi et al. 2019)*.

Bubble enhanced mingling has also been investigated *(e.g. Manga and Stone 1995; Wiesmaier et al. 2015)* however, the effect on bubbles in the latter stages of mixing has not been widely discussed. Here, it is proposed that during mixing, bubbles can become decoupled from the melt and interact with the surrounding melts following the intrusion of two compositionally different magma bodies.

In the case that a hot buoyant body of gas-rich magma rises to meet a cooler previously degassed magma body resulting, turbulent mixing will cause both heat and mass to be transferred, and bubbles could become decoupled. This leaves them free to interact with both the degassed melt and the new mixed-composition melt, both of which would have a lower volatile saturation than original buoyant melt. A volatile concentration gradient between the bubble and distal melt down then enables the transfer of mass via diffusion **(see 1.3.2)** and the bubble is resorbed **(Fig.1.2a)**.

Regassing of the melt through bubble resorption would act as a further alteration mechanism to the melt composition following intrusion and mixing. This suggests bubble resorption could occur in tandem with physical mixing effects *(Manga and Stone, 1995)* to aid the mixing of two distinct melts into a single homogeneous melt composition.

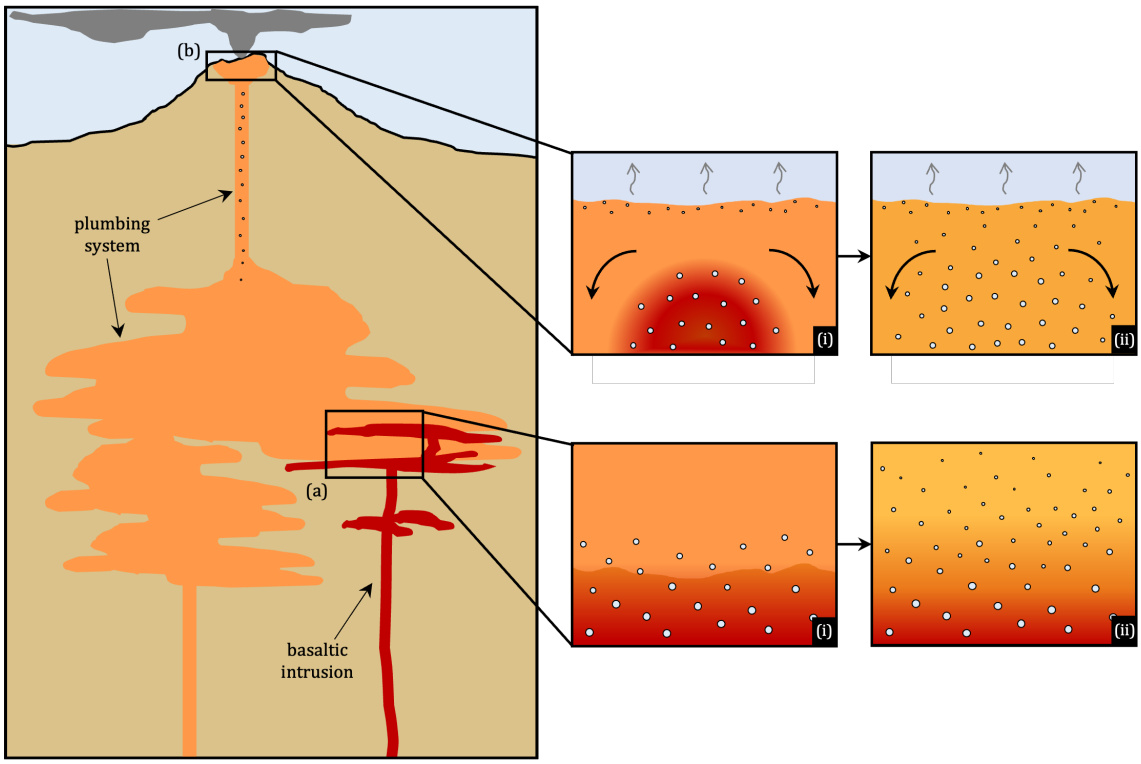

Figure 1.2: Cartoon diagrams showing some of the hypothesised scenarios where decoupled bubble resorption may take place within a volcanic system. **(a)** Intrusion and mixing of two magma bodies with different compositions. **(ai)** A hotter more buoyant bubbly magma body rises to interact with a cooler, denser magma that have previously been degassed. **(aii)** Bubbles become decoupled and migrate through the degassed magma, transferring mass diffusively as they do. **(b)** Convection cells within an open lava lake. **(bi)** Bubbles rising within a hot body of magma will move directly past downwelling, cooler melt that has been degassed at the lake surface. **(bii)** This direct interaction results in diffusive mass transfer between the rising bubbles and downwelling melt. **(c)** Foam drainage at during open-system degassing.

1.3.2.2 Convective Cells

The theory that magmatic melts and volatiles can be continuously cycled has been used to explain observations from open lava lakes such as those at Mount Nyiragongo, D.R.Congo, Etra Ale, Ethiopia, or Kilauea, Hawaii. In these lakes, convection of material is though to enhance degassing processes leading to phenomena such as spattering and fountaining within the lake *(e.g. Harris 2008; Patrick et al. 2018; Valade et al. 2018)*.

Considering this scenario on bubble-scale, melt that has undergone a comination of passive and active degassing at the surface of the lake will now be denser and depleted in volatiles. This increased density from loss of the bubble phase causes the magma to downwell back to a greater depth in the system. As it does so, the degassed magma will move directly past volatile bubbles rising within a less dense upwelling magma. This interaction of the sinking degassed melt and decoupled bubbles could result them being resorbed as they rise, via the mechanism outlined in **Section 1.3.2 (Fig.1.2b)**. Consequently, the downwelling melt becomes regassed, having implications for melt density that could influence the convection itself, as well as the rates of movement via its influence on viscosity.

1.3.2.3 Mafic Underplating

Mafic (or basaltic) underplating is a larger scale scenario that considers more of the secondary impacts of bubble resorption and how these could aid the triggering of an eruption. Underplating is the process by which the base of an older, cooler silicic magma body comes into contact with a hotter, buoyant, volatile-rich mafic magma *(Bachmann and Bergantz, 2006)*. The silicic body is likely to be sitting at the saturation point, ready to vesculate bubbles if surrounding conditions change. By contrast, the hotter mafic magma is more gas-rich, having degassed volatiles to become a buoyant multi-phase magma. When the mafic magma underplates the silicic magma, the melt is unable to rise at the same rate due to a large viscosity contrast. However, bubbles within mafic melt continue to rise, becoming decoupled from the melt to rise towards the mafic-silicic boundary.

From here, two main scenarios are hypothesised *(Bachmann and Bergantz, 2006)*; one where the bubbles remain trapped beneath the silicic melt and a second where the bubbles are able to migrate across the melt interface **(Fig.1.3)**.

In the first case **(Fig.1.3a)**, the bubbles collect into a foamy layer along the boundary, gaining buoyancy over time. Eventually, this increased buoyancy and the associated low density of the foamy layer falls out of equilibrium with the overlying silicic melt, resulting in large-scale overturn and mingling of the two melt bodies *(Bergantz and Breidenthal, 2001; Bachmann and Bergantz, 2006; Edmonds and Wallace, 2017)*. As a result, the bubbles become decoupled in the turbulent mix of magmas and could end up being resorbed similarly to **Section 1.3.2.1**. Such large-scale overturn events that occur as a result of large density contrasts are thought to be responsible for triggering eruptive behaviour *(Yoshimura and Nakamura, 2010)*.

In the second case **(Fig.1.3b)**, the viscosity contrast of the two melts is high enough that the two melt remain separated but simultaneously low enough that the more buoyant bubbles can be transferred across the boundary. These bubbles then rise, decoupled from the surrounding silicic melt, and could potentially resorb via the mechanism **(section 1.3.2)**.

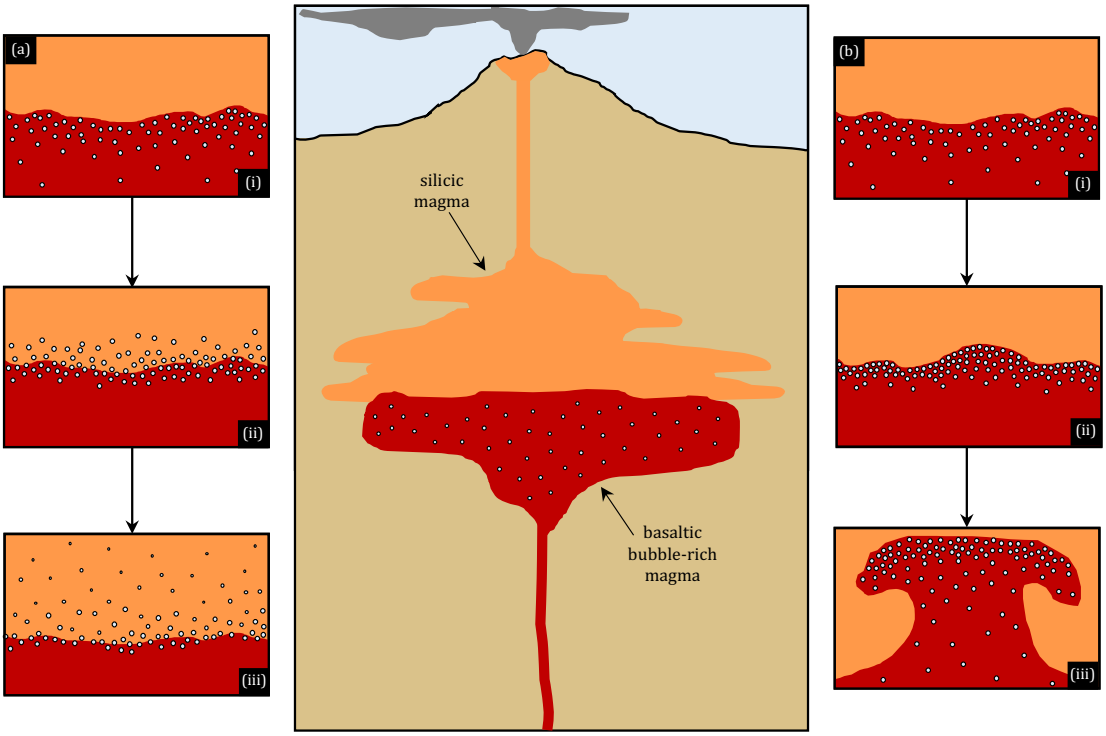

Figure 1.3: Cartoon diagrams showing the two different scenarios that can result from mafic underplating of a silicic magma but a less viscous, bubbly basaltic magma. **(a)** Bubble migration. **(ai)** Bubbles rise towards the melt interface **(aii)** and transfer across the melt boundary. **(aiii)** Bubbles continue to rise into the previously degassed silicic melt where they can be resorbed by diffusive mass transfer. **(b)** Large scale overturn. **(bi)** Bubbles rise towards the melt interface **(bii)** and become trapped at the melt interface. **(biii)** The trapped bubbles increase buoyancy in a concentrated layer leading to large-scale overturn and mingling of the two melts.

The dynamics of bubble migration and heat transfer following underplating have been previously considered by Bachmann and Bergantz (2006), however the potential for mass transfer in such a setting has not. Including the effects of diffusive mass transfer from bubble resorption into the melt migration model for underplating **(Fig.1.3b)** could help explain the differences in melt composition or gas emissions observed at the eruptions of Soufriere Hills, Montserrat or Fish Canyon, Colorado, USA *(Bachmann and Bergantz, 2003, 2006)* where large scale overturn is not the likely cause of eruption.

Theoretical Background

This chapter introduces the theory that underpins work in the later chapter of this thesis. The combined problem of bubble coupling and resorption is set up numerically using a series of dimensionless quantities, introduced to describe the parameter space that that applies to the modelling of singular, spherical bubbles in high viscosity fluids.

A further dimensionless group, the Péclet number, is also introduced. A crucial concept throughout the whole of this work, different modifications of Péclet number are set out to create a suite of dimensionless expressions to describe coupled and decoupled bubble-fluid systems. These Péclet numbers will be used in later chapters to analyse what can enhance or limit resorption in bubble-melt systems.

Following the numerical background, material properties of different gas-melt systems are introduced to obtain an understanding on their controls. Magmatic melts are discussed alongside several analogue melts which are used in experimental studies discussed later on.

2.1 Bubble Regimes

Rising bubbles in any fluid system can occupy many different behavioural regimes depending on the conditions. In each regime, the effects of different parameters dominate to differing degrees, impacting the geometry of the bubble and dynamics of the combined bubble and fluid. In a volcanological context, these variations can affect the stability and interations of two-phase bubbly magmas, whcih in turn could impact eruptive style or explosivity.

2.1.1 Dimensional Quantities to Describe Bubble Regimes

Bubble regimes can be defined through dimensionless quantities. These quantities take into account the effects that inertia, viscosity, gravity, and surface tension can have on the bubble, showing which effects are dominant on the system *(Clift et al., 2005)*.

Applying the conditions for a typical basaltic gas-melt system to these dimensionless quantities will enable the specific bubble regimes investigated in this work to be defined. As a result, this allows the combined effects of bubble coupling and resorption via diffusive mass transfer to be described in dimensionless space, and will justify the application of certain assumptions and models in the following chapters.

Much of the theory presented here is applicable to wider applications than just gas-melt systems. Therefore the background theory is discussed with respect to bubble-fluid systems rather than any one specific system. If bubbles in a volcanic setting are being discussed in more detail, a bubble-melt or bubble-magma system may be referred to instead.

2.1.1.1 The Reynolds Number

The first dimensionless quantity to consider is Reynolds number Re. This describes the balance between viscous and inertial effects in the fluid surrounding a bubble. Re can be expressed as,

$$\mathrm{Re} = \frac{u_\infty \rho R_0}{\mu} \tag{2.1}$$

where R_0 is the initial bubble radius, ρ is the fluid density, u_∞ is the terminal rise velocity of the bubble and μ is the fluid viscosity. When $\mathrm{Re} \gg 1$, inertial effects dominate in the surrounding fluid, whereas, when $\mathrm{Re} \ll 1$, viscous forces are induced instead.

2.1.1.2 The Eötvös Number

A second dimensionless quantity, Eötvös number, Eo describes the ratio of gravitational and surface tension effects on a bubble in a fluid as,

$$\mathrm{Eo} = \frac{R_0^2 g(\rho_b - \rho)}{\Gamma} \tag{2.2}$$

where g is acceleration due to gravity, ρ_b is the density of the gaseous bubble phase and Γ is the surface tension. Higher values of Eötvös number ($\mathrm{Eo} \gg 1$) indicate that gravitational forces dominate the system, whereas at lower values ($\mathrm{Eo} \ll 1$), surface tension forces dominate.

2.1.1.3 The Density Ratio

The density ratio Π_b is a further dimensionless quantity, the value of which dictates the relative buoyancy of a bubble-fluid system. It is expressed as the ratio of the gaseous bubble phase and fluid phase densities.

$$\Pi_b = \frac{\rho_b}{\rho} \tag{2.3}$$

When $\Pi_b \gg 1$, the bubble is equivalent to a solid particle and will therefore sink in the surrounding fluid. When $\Pi_b \ll 1$, the bubble is buoyant and will rise instead.

2.1.1.4 The Morton Number

A final dimensionless quantity to take into consideration is Morton Number Mo. This can be defined from Eo and Re to give a value that is independent of lengthscale or timescale, and instead depends only of material parameters of the bubble-fluid system.

$$\mathrm{Mo} = \frac{Eo^3}{Re^4} = \frac{\mu^4 g(\rho_b - \rho)}{\rho^2 \Gamma^3} \tag{2.4}$$

The exact interpretation of Morton number for bubble-fluid systems is as of yet quite unclear, however it is included here for completeness in a similar way to other studies in this field.

2.1.2 Coupled & Decoupled Regimes

The Stokes number, Stk is another dimensionless quantity used to identify if a bubble-fluid system is coupled or decoupled. It is expressed as the ratio of the characteristic times for bubble and fluid motion, defined as,

$$\mathrm{Stk} = \frac{t_0 u_b}{l_0} \tag{2.5}$$

where t_0 is the relaxation time of a fluid, l_0 is the characteristic lengthscale of the fluid and u_b is the velocity of the of the particle in the fluid.

This expression leads to second definition for Stk, which instead considers the ratio of the bubble and fluid velocities, u_b and u_0 respectively.

$$\mathrm{Stk} = \frac{u_b}{u_0} \tag{2.6}$$

Equation 2.5 and **2.6** are equivalent to onanother when t_0/l_0 is given by $1/u_0$.

If u_b is taken to be the bubble velocity, for the case of bubbles in a highly viscous melt such as magma u_b can be replaced with the terminal rise velocity u_∞, leading to a further expression for Stokes number,

$$\mathrm{Stk} = \frac{u_\infty}{u_0} = \frac{R_0^2 g \Delta\rho}{u_0 \mu} \tag{2.7}$$

where R_0, g, $\Delta\rho$ and μ are system parameters as previously defined, and u_0 is the velocity of the melt *(Clift et al., 2005)*.

High values of Stokes number, $\mathrm{Stk} \gg 1$, indicate that a system is strongly decoupled, meaning a bubble would rise freely through the fluid with a large relative velocity. Low values of Stokes number, $\mathrm{Stk} \ll 1$, instead indicate the system is strongly coupled. In this case, the bubble appears stationary in the fluid as it has no rise velocity relative to it.

In natural magmatic systems, relatively high melt viscosities which confine the setting to the low Reynolds number regime, mean that bubble rise velocities (u_∞) vary only within a few orders of magnitude compared to the ascent rate of the surrounding melt (u_0). By contrast, u_0 can vary over several orders of magnitude. As a result, values of Stk for natural melt systems vary over significant orders of magnitude, suggesting that there are huge variations in the degree of bubble-melt coupling from system to system.

This variety is confirmed by surface-level observations of different volcanic systems around the world that display many different eruption styles as a consequence of the differences in bubble-melt coupling, which influences other processes in the build up to an eruption.

2.1.3 Bubble Regimes of This Work

Each of the dimensionless quantities outlined above to describe bubble-fluid systems, is now considered with respect to the systems of interest in this work. More specifically, a gaseous bubble within either a basaltic or rhyolitic magma. Order of magnitude estimates for the typical value of the different parameters *(Gonnermann and Manga, 2013)* are used to calculate each dimensionless quantity can be made. This allows the most likely bubble regime of the system to be found. In addition, an upper limit is estimated to find the largest bubble that could exist in the fastest rising, lowest viscosity form of each magma, whilst still remaining in this same bubble regime. **Table 2.1** shows these estimates for both basaltic and rhyolitic melt compositions.

	Order of Magnitude Estimate log(10)						Dimensionless Quantity log(10)			
	μ_0 Pa.s	u_∞ ms^{-1}	ρ_0 kgm^{-3}	ρ_b kgm^{-3}	Γ Nm^{-1}	R_0 m	Re	Eo	Π_b	Mo
B	3	-2	3	-1	-1	-3	-5	-1	-4	17
R	8	-2	3	-1	-1	-3	-10	-1	-4	37

Table 2.1: Order of magnitude estimates of the system parameters for a typical basaltic (B) and rhyolitic melt (R). Dimensionless quantities: Reynolds number, Re, Eötvös number, Eo, Density ratio, Γ and Morton number, Mo are calculated from these estimates and values coloured according to relative size to allow for interpretation. Blue = < 1, orange = ≈ 1 and pink = > 1. Values for Morton number are included for completeness but do not yield much other interpretation for the type of bubble regime or behaviour of the bubble-melt systems.

The estimates in **Table 2.1** show that for a typical basaltic system, each of Reynolds number, Eötvös number and the density ratio have values less than one. This places a typical basaltic system towards the upper limit of the viscous and surface tension dominated regime where spherical bubbles will rise buoyantly through a reasonably low viscosity melt. Estimates for a typical rhyolitic system similarly yield values of Re, Eo and Π_b all less than one. The significantly lower value of Reynolds number can be attributed to the much greater viscosity of a rhyolitic melt compared to a basaltic melt. In consequence, all bubbles considered in this thesis will be buoyant and dominated by viscous and surface tension effects, making them spherically stable.

Estimates for Stokes number of these systems have not been made here as varying degrees of bubble-melt coupling can exist in both basaltic and rhyolitic magmas **(Figure 1.1)**. As a result, values of Stk vary significantly across systems of the two different melt compositions. The range of Stokes numbers accessible in a basaltic melt system means varying degrees of bubble-melt coupling would be observable; from completely decoupled, high-Stokes number systems, through to completely coupled, low-Stokes number systems. In the next section of this chapter, the relationship between this degree of coupling and the rates of diffusion or advection for bubble-melt systems is outlined along with how further regimes of dynamic bubble behaviour can be distinguished from these relationships.

2.2 Péclet Numbers

The Péclet number (Pe) is a class of dimensionless numbers used in the study of fluid dynamics to represent a ratio of timescales. Péclet numbers can define timescale ratios for lots of different processes, but are most commonly used to describe heat or mass transfers. Most significant to this study is mass trasnfer, for which a Péclet number can be expressed that is the ratio of advective transport rate to diffusive transport rate *(Levich, 1962; Patankar, 1980)*.

$$\mathrm{Pe} = \frac{\text{advective transport rate}}{\text{diffusive transport rate}} \tag{2.8}$$

Considering the transfer of mass in or out of a bubble phase, this Péclet number can also be defined using the relative timescales for advection and diffusion instead of with rates. With this approach, Péclet number can be expressed as,

$$\mathrm{Pe} = \frac{\text{diffusive time}}{\text{advective time}} = \frac{\lambda_D}{\lambda_A} \tag{2.9}$$

where λ_D is the diffusive timescale and λ_A is the advective timescale.

The differing degrees to which a bubble may be coupled to a fluid means the definition of advective used to find λ_A in **Equation 2.9** can be thought of in two distinct ways, (1) the movement of melt material around the interface of a bubble as it rises buoyantly through the packet of melt, or (2) the movement of melt material into the space previously occupied by a stationary, shrinking bubble.

Case 1 describes advection in a decoupled high-Stokes number system, where the bubble has a buoyant rise velocity relative surrounding melt. By contrast, case 2 describes advection in a coupled system, where there the apparent relative velocity between the bubble and the melt is zero. This system would sit in the low-Stokes number regime.

2.2.1 Diffusive Timescale (λ_D)

The diffusive timescale, λ_D depends significantly on the value of the diffusion coefficient, D, of the system. This diffusion coefficient, also known as mass diffusivity, is the proportionality factor in Fick's Law to describe how far a mass of a substance will diffuse over a given timescale *(Mostinsky, 2011)*. Values of D vary between systems depending on concentration gradient, temperature, pressure and the exact substances used. In gas-glass systems, some glasses are more accommodating of certain gases based on solubility and particle size *(Schaeffer, 1984; Bansal and Doremus, 1986; Brehens, 2010)* **(see 2.3)**).

Diffusivity is measured in meters squared per second, and so can be expressed as a ratio of lengthscale, L squared over a timescale t. Rearranging this yields an expression for the diffusion timescale λ_D.

$$D = \frac{L^2}{t} = \frac{L^2}{\lambda_D} \tag{2.10}$$

For the context of gases diffusing from a spherical resorbing bubble into a surrounding fluid, the diffusive lengthscale L can be thought of as the largest radial distance around the bubble which can be saturated by the total number of moles of gas originally in the bubble. Therefore, the diffusive lengthscale is dependent on the original size of the bubble and components of the ideal gas equation for the diffusing gas, such as molar mass, M_m , system pressure p_0 and temperature, T. A complete derivation for this diffusive lengthscale is shown in **Appendix II**, with the final expression being,

$$L = \frac{100 M_m p_0}{3 R_g T \rho_m S_0} \cdot R_0 \tag{2.11}$$

where ρ_m and S_0 are the melt density and solubility, and R_g is the ideal gas constant. Applying this to **Equation 2.10** means the characteristic diffusive timescale of gas diffusing from a bubble into melt can be expressed as,

$$\lambda_D = \left[\frac{100 M_m p_0}{3 R_g T \rho_m S_0} \right]^2 \cdot \frac{R_0^2}{D} \tag{2.12}$$

suggesting λ_D has a strong dependence on the specific gas species through its equation of state, and as well as the initial radius of the bubble.

2.2.2 Advective Timescale (λ_A)

Given that bubble-fluid systems can either be coupled or decoupled, there are two possible definitions for advective timescale λ_A as set out in **Section 2.2**. This means two different numerical experssion of λ_A can also be made.

For the case of coupled bubbles, the advective timescale refers to the time required for surrounding fluid (or melt) to respond to a shrinking bubble, defined as the melt shell response timescale λ_v. For the case of decoupled bubbles in the high-Stokes number regime, the advective timescale refers in essence to the time taken for a bubble to rise through a lengthscale of melt, defined in this work as the bubble rise timescale λ_b.

2.2.2.1 Melt Shell Response Timescale (λ_v)

As a bubble grows or shrinks within a viscous melt, the rate of growth is heavily controlled by viscosity of the melt near to the bubble interface, sometimes referred to as the melt shell. This shell exerts a viscous resistance which needs to be overcome in order for the bubble to change size *(Blower et al., 2001; Coumans et al., 2020)*. Once this resistance is overcome, the melt will undergo viscous relaxation, meaning it is able to move (advect) around the bubble interface. In the case of a growing bubble, the melt is pushed away to accommodate the expanding gas phase. However, in the case of a shrinking or resorbing bubble, the melt shell advects inwardly to occupy the space held by the previously larger bubble.

A key driver of changes to bubble size in this setting is over or under-pressure of the gas phase relative to the surrounding melt pressure, p_0. Combining the effects of this and viscosity, μ a characteristic timescale for the viscous relaxation response can be defined. This melt shell response timescale, λ_v can also be thought of as the time over which the melt advects towards

or away from the bubble interface *(Navon et al., 1998; Lensky et al., 2004)*.

$$\lambda_v = \frac{4\mu}{p_0} \tag{2.13}$$

λ_v is proportional to the melt viscosity yet inversely proportional to melt pressure. Therefore in higher viscosity melts, the melt shell will be much more resistive to movement meaning it won't relax as easily and thus the system will have a longer response timescale. Alternatively, in high viscosity melt systems where pressure is extremely high, the bubble would collapse rapidly in on itself because of the large pressure contrast with the gas inside the bubble.

2.2.2.2 Bubble Rise Timescale (λ_b)

The buoyant rise of bubbles in glassy or magmatic melts is best described by the Hadamard-Rybczynski (H-R) equation for terminal rise velocity u_∞,

$$u_\infty = \frac{2}{3}\frac{R^2 g \Delta\rho}{\mu} \cdot \frac{(\mu + \mu_b)}{(2\mu + 3\mu_b)} \tag{2.14}$$

where R is bubble radius, μ_0 is melt viscosity, μ_b is viscosity of the bubble species, g is acceleration due to gravity and $\Delta\rho$ is the density contrast between the melt and bubble phases (Hadamard, 1911; Rybczynski, 1911). This equation highlights the significance of melt viscosity and bubble size on the rise velocity, which has been confirmed experimentally in previous work for both isothermal and non-isothermal conditions *(Hornyak and Weinberg, 1984; Li and Schneider, 1993; Jackson et al., 2022)*.

When the contrast between the melt and gas viscosities is very large, the secondary term in **Eq.2.14** tends to $\frac{1}{2}$, meaning the H-R equation can be simplified to,

$$u_\infty = \frac{1}{3}\frac{R^2 g \Delta\rho}{\mu} \tag{2.15}$$

which is more appropriate for magmatic gas-melt systems. Applying this simplified expression for terminal rise velocity a simplified problem where the lengthscale of bubble rise is equal to its initial radius, R_0, the timescale for buoyant advection, λ_b, can be defined.

$$\lambda_b = \frac{R}{u_\infty} = \frac{3\mu}{Rg\Delta\rho} \tag{2.16}$$

λ_b is proportional to the melt viscosity, meaning that in a system where bubble size and melt density remain constant, increases in viscosity will result in a slower terminal rise velocity of the bubble and thus a longer advective timescale. Similarly, smaller bubbles will have a longer rise timescale owing to a slower rise velocity driven by the inverse relationship between λ_b and R_0.

2.2.3 Defining Two Distinct Péclet Numbers

With coupled and decoupled gas-melt systems requiring different definitions for the advective timescale, it follows that each of the two systems has its own definition of Péclet number. By adapting the general definition of Pe **(Eq.2.9)** to account for either viscous advection

through melt shell response or buoyant advection through bubble rise, two unique expressions can be written. The former for coupled, low-Stokes number systems, and the latter for decoupled, high-Stokes number systems.

2.2.3.1 Stationary Péclet Number (Pe_s)

For coupled bubble-melt systems, Péclet number can be expressed as the ratio of the diffusive timescale λ_D and melt shell response timescale λ_v. This is the stationary Péclet number Pe_s, applicable to systems where Stk << 1 and the bubbles appear stationary relative to the melt.

$$Pe_s = \frac{\lambda_D}{\lambda_v} = \left[\frac{100 M_m p_0}{3 R_g T \rho_m S_0}\right]^2 \cdot \frac{R_0^2 p_0}{4 D \mu} \tag{2.17}$$

This expression suggests that Pe_s is highly dependent on the pressure of the surrounding melt, having a proportionality to p_0^3. By comparison, the dependence of Pe_s on initial bubble radius, melt viscosity and diffusivity appear less significant.

A low value of Pe_s means the system is limited by viscosity as λ_v will be significantly longer than λ_D. At this point, the rate of bubble shrinkage is determined by how quickly the surrounding melt shell can respond and relax into the space once occupied by the shrinking bubble. In the endmember case where melt viscosity becomes increasingly high, $Pe_s \to 0$ and system pressure will instead become the controlling factor on bubble shrinkage, as significant over-pressure would be required to counteract the extremely resistive high viscosity.

A high value of Pe_s means the system is limited by diffusion as λ_D will be much longer than λ_v. For this case, the low melt viscosity means the melt shell around the bubble is able to relax inwards with relative ease. The value of diffusion coefficient becomes the principal control such that in the opposite endmember case, as D reduces towards zero, $Pe_s \to \infty$ and the gaseous species is essentially unable to move into the melt.

It is expected that the transition between these two limits will also occur around $Pe_s = 1$ where λ_D and λ_v will be in a similar order of magnitude, and the melt shell is able to relax at a similar rate as the gaseous phase can diffuse through it. The stationary Péclet number and its application to natural volcanic systems is discussed further in **Chapter 5**.

2.2.3.2 Buoyant Péclet Number (Pe_b)

For decoupled bubble-melt systems, Péclet number can be expressed by taking the ratio of the diffusive timescale λ_D and bubble rise timescale λ_b. This yields the buoyant Péclet number Pe_b for systems where Stk>> 1.

$$Pe_b = \frac{\lambda_D}{\lambda_v} = \left[\frac{100 M_m p_0}{3 R_g T \rho_m S_0}\right]^2 \cdot \frac{R_0^3 g \Delta\rho}{3 D \mu} \tag{2.18}$$

For this version of Péclet number, the initial bubble radius appears the most significant parameter, with Pe_s being proportional to R_0^3. Melt pressure has a second order significance and melt viscosity, diffusivity, and density contrast even less.

A high value of Pe_b means the system is limited by diffusion such that λ_D will be much longer

than λ_b. In this case, a bubble would rise rapidly, unimpeded by the melt viscosity and the diffusion coefficient would act as the principal control on the movement of gas into the melt. In the endmember case where D becomes so small that $\lambda_D >> \lambda_b$, $\mathrm{Pe}_s \rightarrow \infty$ and minimal diffusion would be observed such that the bubble appears not to reduce in size during rise.

A low value of Pe_b means the system is instead limited by viscosity as λ_b will be much longer than λ_D. This means the advection of melt around the rising bubble is slower than the rate at which the gas species diffuses into the melt. Since λ_b is controlled principally by the bubble's size and the melt viscosity, an opposite endmember case will occur as μ increases or R decreases such that $\mathrm{Pe}_s \rightarrow 0$. At this point, bubble rise will be halted meaning it becomes stationary in the melt.

Therefore, at very low values of Pe_b, the system transitions to a low-Stokes number regime and instead, the stationary Péclet number Pe_s becomes more applicable. Melt viscosity and bubble size can therefore be seen to act as a switch control between the two cases of coupling and decoupling in a system. Further investigation of the buoyant Péclet number, including experimental observations and the transitions between the different Péclet number regimes is outlined in **Chapter 6**.

2.3 Materials, Properties & Parameters

Material properties of magmatic melts can be determined through various underpinning laws that show how they vary with changes to conditions in the wider system. The effect of temperature and pressure variations are chiefly considered for the context of this study as they can vary significantly within a volcanic system, both spatially and temporally.

Alongside an overview of magmatic melts, the material properties of several analogue materials, including manufactured silicate melts (glasses), viscous oils and syrups, are also introduced. This highlights the similarities to magmatic melts that makes these analogues suitable in scaled experiments such as those carried out later in this study.

2.3.1 Magmatic Melts

2.3.1.1 Composition

The major element composition of naturally occurring silicate melts is fairly consistent, comprising of silicon, oxygen, aluminium, some alkali and alkali earth metals, titanium and iron. These build to together to form a base network of tetrahedral silicate anions (SiO_4^{4-}), charge balanced by cations *(Mysen, 1983; Henderson et al., 2006)*. In addition to these major elements, other more minor elements may be present which are able to alter the base network or modify the wider silicate structure. These modifications are observed as chnages in material properties like viscosity.

In magmatic melts, silicon can be partially replaced by aluminium ($\mathrm{Al}^{\mathrm{III}}$) to form an aluminosilicate base network. Further modifications to the melt can also occur when alkali cations such as Na^+, K^+, Mg^+ and Ca^+ are present. These act to modify the base network by binding with oxygen to form metal oxides, breaking the continuous Si – O – Si bonds as a result *(Bottinga and Weill, 1972)*. Therefore, melts with a high presence of network modifying cations

are said to be depolymerised compared to a completely polymerised melt of only Si and O.

These network alterations lead to magmatic melts being classified by their SiO_2 and alkali oxide (NaO_2 and K_2O) composition using Total Alkali Silica (TAS) diagrams such as **Figure 2.1**. On this diagram, it can be seen that basaltic melts have medium-to-low alkali and SiO_2 content whereas rhyolitic melts have very high SiO_2 and wide variation in alkali content. These two melt classifications are principally focused on in this study as they represent two opposing compositions associated with different types of volcanism **(Fig.1.1)**.

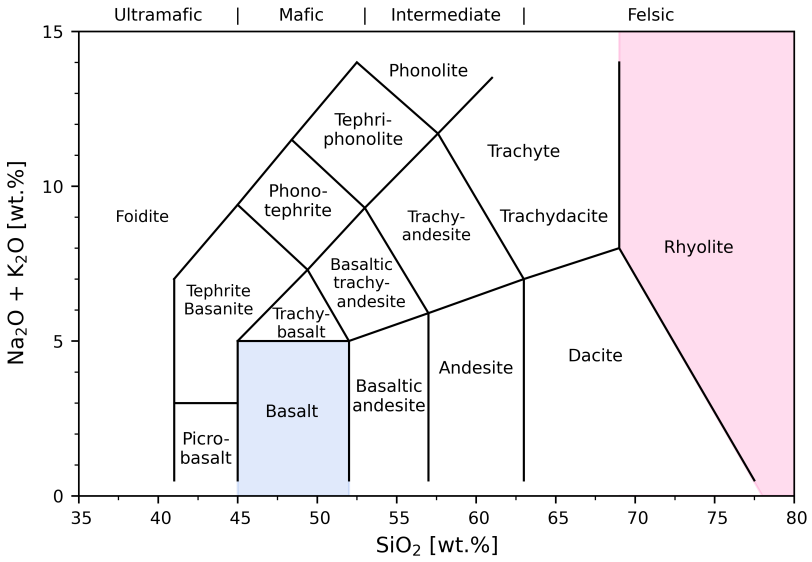

Figure 2.1: Total Alkali Silica diagram adapted from Iacovino and Gouard (2021) to show the variation in both SiO_2 and total alkali content between different melt classifications. Compositions of basaltic and rhyolitic melts are highlighted in blue and pink respectively. An alternative classification system is included along the top axis.

TAS classification diagrams use the assumption of a dry melt; so are based on melt composition which are completely free of dissolved volatiles like H_2O or CO_2. In natural systems, magmatic melts can instead contain varying quantities of volatiles that affect the network structure and melt properties because OH- hydroxyl and CO_3^{2-} carbonate ions act as network modifiers, reacting with oxygen to break up the base network and depolymerise the melt *(eg. Behrens and Gaillard, 2006)*.

Therefore, to conclude, it is crucial to know the volatile content in addition to the wider compositional make-up of a magmatic melt in order to understand its material properties.

2.3.1.2 Viscosity Laws

Dynamic viscosity of a fluid μ is the ratio of the shear stress experienced to the strain rate applied; expressed more simply as the resistance of a fluid to movement. The viscosities of naturally occurring magmatic melts vary dramatically, from highly viscous rhyolites where μ can be greater than 10^8 Pa.s, to much lower viscosity basalts or basanites where μ is closer to 10^0 Pa.s *(Lesher and Spera, 2015)*. This significant range between different TAS classifications of melt highlights the control of chemical composition and structural make up on the observed physical properties.

As a result, SiO_2 and volatile content are two quantities that can alter the viscosity of a mag-

matic melt. **Figure 2.2a** demonstrates the effect of increasing SiO_2, equivalent to increasing the polymerisation of the melt. A lack of bond-breaking network modifiers means the melt has a much more rigid structure, which is reflected though a high viscosity. Consequently, rhyolitic and dacitic melts have much greater viscosities than basaltic melts under the same conditions.

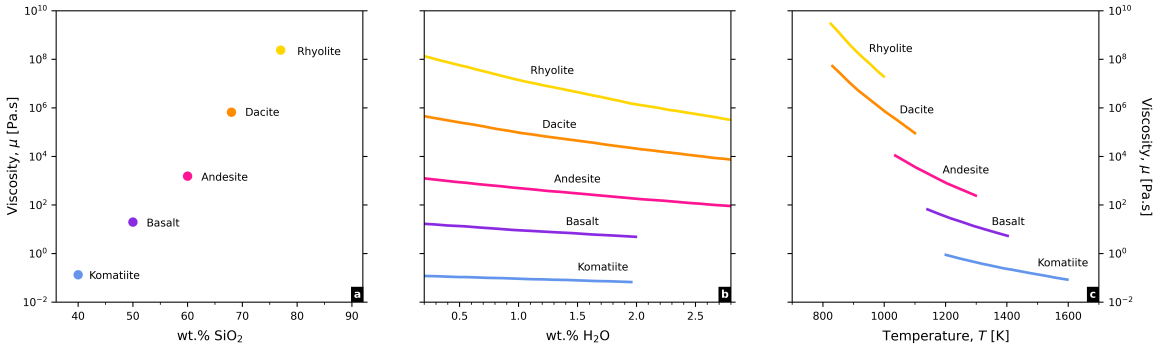

Figure 2.2: Set of plots showing how visocsity of different magmas vary with **(a)** silica content, **(b)** volatile water content, and **(c)** temperature. In all figures, basaltic melts have significantly lower viscosities than rhyolitic melts.

Figure 2.2b shows the effect of volatile content on magmatic melts. Just a 3 wt.% increase in the quantity of dissolved volatiles (in this case water) can reduce the dynamic viscosity of a melt by over two over two orders of magnitude. This results from modification of the bonding network and increased depolymerisation. The effect is most dramatic for silicate-rich melts and the first 1 wt.% H_2O increase, after which the effect becomes increasingly less pronounced *(Hess and Dingwell, 1996)*.

Fluid viscosities, including those of magmatic melts are also significantly affected by temperature, described by an Arrhenian relationship in the Vogel-Fulcher-Tammann (VFT) equation,

$$\mu = \mu_0 \exp \frac{\mathrm{A}}{(T - \mathrm{B})} \tag{2.19}$$

where T is temperature in Kelvin, A and B are constants unique to the melt and μ_0 is viscosity of glass transition *(Vogel, 1921; Fulcher, 1925; Tammann and Hesse, 1926)*. An increase in temperature reduces the viscosity of the melt exponentially, meaning that at higher temperatures, melts are more dynamically mobile than at lower temperatures **(Fig.2.2c)**. The exact values of A and B vary between melts based on their composition, as is also true for the value of μ_0.

The viscosity of glass transition μ_0 has additional significance as it represents the viscosity at which the melt first displays fluid-like behaviour; also described as where the applied stress and the strain rate are proportional, and any response to stress is immediate. For magmatic and silicate melts, this transition in behaviour is controlled by the relaxation time of the melt which itself is determined by rate at which Si – O bonds can be broken in the structural network *(Dingwell, 2006)*. For any given melt, this process has a strong dependency on temperature and therefore μ_0 has its own temperature relationship,

$$\mu_0 = \frac{c}{|q|} \tag{2.20}$$

where c is a function of the melt composition and q is the heating or cooling rate *(Gottsmann et al., 2002)*.

Viscosity models for magmatic melt have been developed that incorporate the effects of both temperature and volatile content, more specifically, H_2O content. Some of these models are for a very specific type of melt or conditions, whereas others are derived to be used for a much wider range systems. For example, Hess and Dingwell (1996) present a model suggested to be best for silicic and hydrothermal granitic melt systems, where viscosity can range between 10^2 - 10^{13} Pa.s and H_2O content altered from 0 - 12.5 wt.%. Giordano et al. (2008) have also developed a comprehensive viscosity model that uses compositional inputs to estimate viscosities between 10^{-1} - 10^{14} Pa.s and 0 - 8 wt.% H_2O. Some of these melt-specific viscosity laws are applied in the modelling of bubble systems in **Chapter 5 6**.

2.3.1.3 Solubility Laws

Solubility of a fluid is the key driver for mass transfer in a gas-fluid setting, where it describes the amount of gas that can be accommodated into the fluid under equilibrium conditions. The presence of a concentration gradient over a distance x between a bubble of gas and the surrounding fluid enables the migration of the gas species into the fluid, down the concentration gradient, from a region of high gas concentration c_i to a region of low gas concentration c_∞ **(Fig.2.3)**.

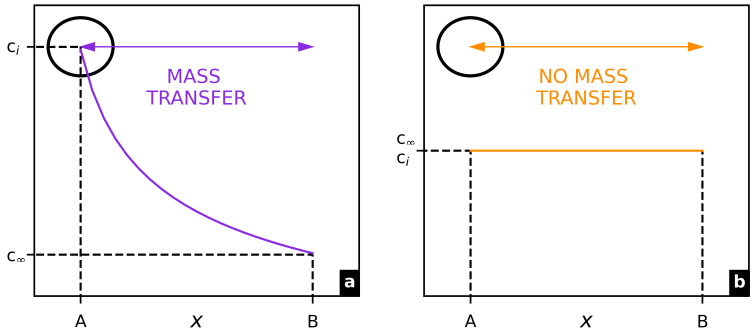

Figure 2.3: Schematic representation of concentration variation as distance, x from a bubble increases. For cases where **(a)** concentration at the bubble, c_i is greater then in the distal melt, c_∞ mass transfer can take place, whereas **(b)** if there is no concentration gradient, mass transfer is not plausible.

In volcanic systems, magmas and natural silicate melts act as the fluid phase, and exsolved volatile bubbles as the gas phase. Any diffusive mass transfer that occurs from the bubble is controlled by solubility of the melt, which in turn can vary in its degree of saturation (or concentration) *(McIntosh, 2013)*. Low solubility, highly volatile-saturated melts will act as if they are already in equilibrium as the melt has no more capacity to accommodate dissolved volatiles. However, if the gas bubble sits within a high solubility, volatile-unsaturated melt, a concentration gradient exists as the melt has capacity to take up further dissolved volatiles and so the gas species can be transferred diffusively.

Figure 2.3 sets out these two endmember scenarios schematically in order to highlight the pinnacle significance of solubility, saturation and concentration gradients to the hypothesis of bubble resorption and shrinkage.

For many gas-fluid systems, Henry's Law can be applied to find the solubility C of the gas species g.

$$C_g = Hp_g \tag{2.21}$$

It shows how solubility is unique to each system, being dependant on the partial pressure of the gas p_g and Henry's constant H which itself is strongly dependant on the fluid and temperature, and weakly dependant on pressure *(eg. Gamsjäger et al., 2010)*. H and therefore C_g are proportional to both temperature and pressure. For more complex scenarios where multiple different gas phases or species may be present, Henry's Law is not applicable. Instead, more comprehensive solubility laws have been developed that are unique to a specific or range of melt classifications and a specific gas.

Zhang (1999; 2007) and Liu et al. (2005) have looked extensively at H_2O and CO_2 solubility laws for rhyolitic melts, developing several models for different system conditions. One such model for mixtures of H_2O and CO_2 applicable for rhyolitic and haplogranitic melts between 700 - 1200 ^oC and up to 500 MPa, shows an inverse relationship between volatile solubility and temperature, but proportionality to pressure (Liu et al., 2005) **(Fig. 2.4)**. A similar observation is made by Ryan et al. (2015) for H_2O in rhyolitic obsidian, where they find the magnitude of retrograde solubility with temperature to be -7.1 x10^{-3} wt.% per 100 ^oC **(Fig. 2.4)**.

Solubility studies have also been completed for a whole range of volatiles and rare gases in melts with a more basaltic composition *(Jambon et al., 1986; Pan et al., 1991; Berndt et al., 2002; Behrens et al., 2009; Lesne et al., 2011)*. Experimental data from these studies suggest that the pressure control on solubility is much stronger than the temperature control, but similarly that solubility increases with pressure and decreases slightly with temperature **(Fig.2.4)**. Using models such as those from these studies allow the solubility of melts to be estimated for a given gas-melt system with specified conditions. The approach is adapted in **Chapters 5 & 6** of this study when modelling volatile bubble dynamics in naturally occurring melts.

2.3.1.4 Diffusion Laws

Diffusion is the mechanism by which mass is transferred between the bubble and melt phase. As highlighted in **Figure 2.3** diffusive mass transfer will only occur if there is a sufficient concentration gradient over which a substance can equilibrate. Diffusive movement of particles to reach this equilibrium results from random motion as particles from a high concentration spread out into a region of low concentration. Described by Fick's first law, the rate (or flux) of diffusive particle motion J is therefore dependant on the concentration gradient dC/dx and is unique to the system, as indicated by the diffusion coefficient, D.

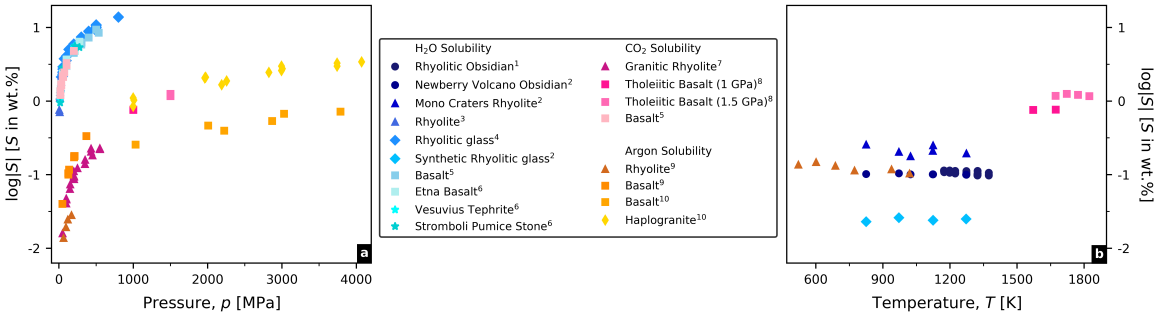

Figure 2.4: Collection of datasets demonstrating the effects of **(a)** pressure and **(b)** temperature on the solubility of different gases in magmatic melts. The effects of increased pressure increasing solubility are more dramatic than those of increased temperature reducing solubility, especially in the first 1000MPa increase. References for the datasets are given in a table in **Appendix I**.

$$J = D\frac{dC}{dx} \tag{2.22}$$

A high concentration gradient will result in more rapid diffusion than a low concentration gradient. Similarly, systems where the diffusion coefficient is high will experience faster rates of diffusion than systems with a lower value of D. This is highlighted further in Fick's second law which relates both the temporal and spatial evolutions of substance diffusion:

$$\frac{dC}{dt} = D\frac{d^2C}{dx^2} \tag{2.23}$$

As described in **section 2.2.1**, applying Fick's laws to a simplified one-dimensional case with fixed initial and final concentrations allows the characteristic timescale or lengthscale of diffusion to be found *(Zhang, 2010)*.

As well as being unique to the system materials, the value of the diffusion coefficient also varies with temperature and pressure. For pure substances, pressure acts to limit the rate of self-diffusion in a system as increasing pressure is thought to reducing the space available between molecules, although the effects are minimal compare to those of temperature which acts to promote diffusion in a system. This relationship of diffusion and temperature is correlated by an Arrhenian relationship,

$$D = D_0 \exp\frac{-pV}{R_g T} \tag{2.24}$$

$$\ln D = \ln D_0 - \frac{Ea}{R_g T} \tag{2.25}$$

where Ea is the activation energy, R_g is the gas constant and D_0 is a fitting parameter unique to the system. At increased temperatures, a substance will diffuse at a faster rate resulting from the thermally increased internal energy and greater particle motion, as described by Fick's first law *(Brehens, 2010)*.

The trends described by these pressure-temperature relationships have been observed for an extensive range of gas-melt systems, including natural and simulated magmatic systems *(Watson, 1991; Roselieb et al., 1996; Alletti et al., 2007; Brehens, 2010)*. **Figure 2.5** summarises

a selection of diffusion data for both gaseous species and individual cations to show how values of D vary significantly from system to system and are more strongly affected by temperature than pressure.

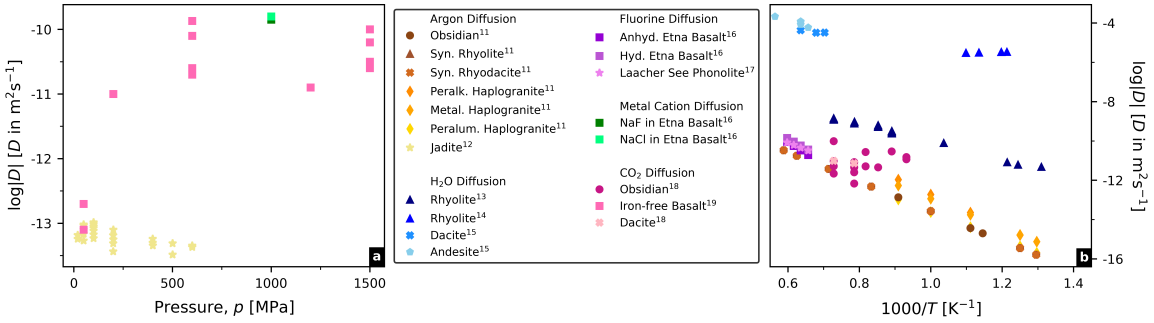

Figure 2.5: Collection of datasets demonstrating the effects of **(a)** pressure and **(b)** temperature on the diffusivity of different gases and cations in magmatic melts. The effects of tempreature are more pronounced, with the value of the diffusion coefficient increasing with temperature. References for the datasets are given in a table in **Appendix I**.

A further observation from diffusion data for magmatic melts is that diffusivity and viscosity of the melt are linked. This was first described by the Stokes-Einstein equation, and subsequently refined to give the Eyring equation,

$$D = \frac{kT}{\mu l} \tag{2.26}$$

where l is the jump distance of an oxygen atom, k is the Boltzmann constant, T is temperature and μ is the viscosity of the melt *(Glasstone et al., 1941)*. It shows that at a given temperature, a gas species will diffuse faster through a lower viscosity melt than a higher viscosity melt. Past hypotheses attribute this to the control that Si – O bond networks have on viscosity (see **2.3.1.2**) and therefore it is harder for a species to move between molecules in highly polymerised viscous melts than in depolymerised melts where fewer Si – O bonds are present. However, work by Oishi et al. (1975) and Henderson et al. (1985) show that diffusion-viscosity data for both natural and manufactured glasses deviate from the Eyring model at a certain temperature so that the value of D becomes much higher than that predicted by the model. **Figure 2.6** shows a collection of data from diffusion studies in natural gas-melt systems showing this same trend. Oishi et al. (1975) described this deviation point, to be when the melt 'super cools' towards a solid state.

Analysis by Dingwell (1990) instead suggests that the deviation arises due to the relative timescales of viscous relaxation (glass transition) and diffusion, and how these relate to the jump frequency of oxygen within the Si – O bonding network. At lower temperatures (higher μ), diffusion is faster than that of the Si – O network, leading to a deviation from the Eyring model. At higher temperatures (lower μ), the timescales of relaxation and diffusion are much more similar, resulting in the convergence of data with the Eyring line.

The significance of a viscosity-diffusivity relationship to this study is limited to the determination of D values for different fluid viscosities during experimental planning and numerical simulations. However, it is important to highlight the inter-play between the different parameters of bubble-melt systems in order to build a holistic view of the impacts that volatile

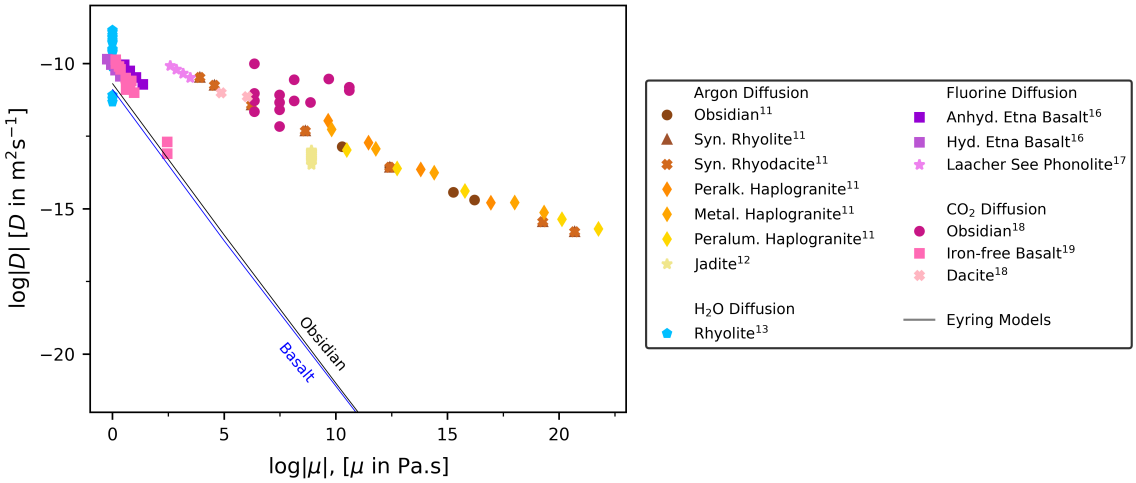

Figure 2.6: Datasets showing the link between the value of diffusion coefficient and melt viscosity. In line with the Eyring equation, increased viscosity results in decreased diffusion however data points deviate significantly from the lines modelled for a rhyolitic obsidian and basalt using **Equation 2.26**. References for the datasets are given in a table in **Appendix I**.

resorption could have.

2.3.2 Analogue Materials

Volcanological studies frequently use data from scaled experimental analysis to validate numerical models built from underpinning theory. This requires the careful selection of analogue materials to ensure the laboratory scale system remains in the correct dimensionless regimes (see **section 2.1**).

For studies investigating the dynamics and interactions of magmas and exsolved gas bubbles, highly viscous analogue materials are typically used to replicate the magma phase. Whilst having lower viscosities than a natural magma, the use of these analogues in smaller scale setups ensures the system sits within low Reynolds and Eötvös number regimes, and that the density ratio remains low *(Kavanagh et al., 2018)*. Under these conditions, viscous and surface-tension forces will dominate, and spherical rising bubble phases can be generated.

There are two main groups of analogue materials to replicate magmatic melts, manufactured silicate glass *(eg. Zhang, 1999; Jackson et al., 2022)*, which requires experimental procedures to be carried out at high-temperatures and high-viscosity oils or syrups *(eg. Llewellin et al., 2002; Mathieu et al., 2008; Spina et al., 2016b)* which allow the correct system regimes to be accessed at room temperature.

In the remainder of this chapter, some of these analogue materials are introduced in more detail, and specific properties and parameter laws explored. This work accompanies subsequent experimental work presented in this thesis which makes use of such analogues.

2.3.2.1 Manufactured Silicate Glass

Manufactured silicate glass melts, also referred to as silicate glasses or synthetic melts are beginning to be used for an increasingly wide range of volcanology studies. These include in-

vestigations into diffusion *(Zhang, 1999)*, solubility *(Zhang, 1999; ?)*, viscosity *(eg. Dingwell and Virgo, 1988; Wadsworth et al., 2022)* and more general magmatic fluid-dynamics studies *(Jackson et al., 2022)*. Originally produced for industrial or artistic use, these glass melts provide a very close analogue to natural silicate melts due to their silica-based bonding structure, resulting composition, high viscosity and temperature-dependant material properties.

Figure 2.7a displays viscosity-temperature relationships for several different manufactured glasses, which all follow unique Arrhenian laws, similar to natural melts. A specific example for the soda-lime-silicate glass *Spectrum System-96 (Jackson et al., 2022)* demonstrates this similarity of silicate glass viscosity laws to those for magmatic melts (eg.**Eq.2.19**).

$$\log|\mu| = -4.10 + \frac{5700}{(T - 430)} \tag{2.27}$$

Conducting experiments in glass at elevated temperatures so that they are molten provides a better replication of real volcanic settings. Furthermore, melt viscosity can be easily and significantly changed by altering the experimental temperature within a single order of magnitude, allowing a large range of melt conditions to be recreated.

Manufactured glasses and melts have the additional similarity to magmatic melts of composition; dominated by SiO_2 content and the degree of Si – O bonds in the network. The exact glass composition can be altered during production to be saturated or depleted in different species. As a result, reactive or mass-transfer processes can be incorporated into experimental analysis by selecting the correct composition of glass *(eg. Pereira et al., 2020; Pigeonneau et al., 2010)*. **Figure 2.7b** shows $\log|\mu|$-$\log|D|$ relationships for some manufactured glasses, demonstrating that diffusion of gaseous species is observable and that the rate diffusion varies with viscosity in a similar way to natural silicate melts.

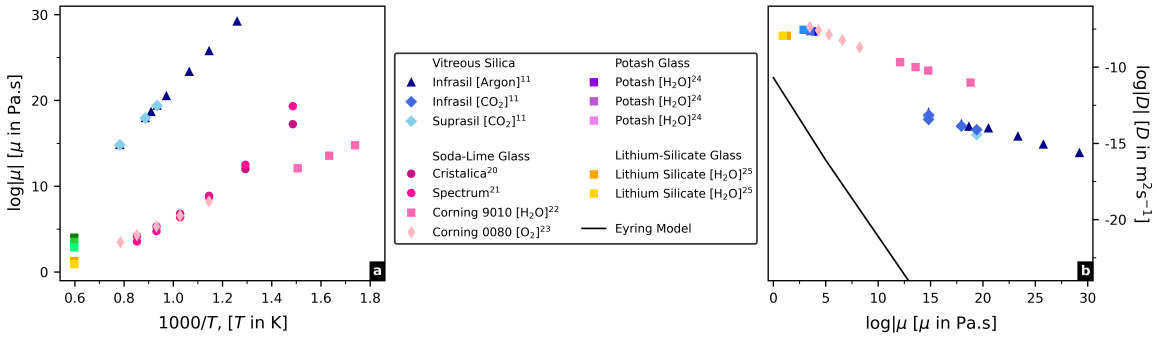

Figure 2.7: Datasets showing the link between **(a)** melt viscosity and temperature, and **(b)** melt viscosity and diffusivity for various manufactured silicate glasses. Similarly to magmatic melt, viscosities can vary dramatically in response to small temperature increments. References for the datasets are given in a table in **Appendix I**.

In **Chapter 4** of this thesis results from studies using glass-based analogues are discussed in relation to the case of non-resorbing decoupled bubbles in magmatic melt systems.

2.3.2.2 Golden Syrup

Despite being more distinctly removed from magmatic melts in terms of chemical and structural make-up, golden syrup, honey and other glucose-based syrups are widely accepted

experimental analogues for recreating observations of volcanic systems on a laboratory scale. In particular, golden syrup has been used to simulate scenarios such as the geometries of magma intrusions *(Mathieu et al., 2008; Poppe et al., 2019)*, multi-phase magma rheologies *(Mueller et al., 2011; Truby et al., 2015; Llewellin et al., 2002)* and lava dynamics in flows, conduits, and lakes *(Castruccio et al., 2010; Beckett et al., 2011)*. Golden syrup is a mixture of sucrose and invert sugars diluted to around 20vol.% with water **Ed Thesis REF**. It's structure is dominated by C - O - H bonding which acts in a similar way to the Si - O bonding in a magma. This composition and bonding structure lead to material properties that make golden syrup popular as an analogue, including its translucency, Newtonian fluid properties and the ease with which its viscosity can be altered through dilution or temperature change.

As with natural silicate melts, the viscosity of golden syrup has an inverse relationship with temperature, driven by the thermally-induced breakdown of the C – O – H structure and increase in internal energy. Viscosity can also be reduced by further dilution with water; a process more suitable for laboratory-scale analysis where temperature control isn't possible or would have other unwanted effects on the system *(Beckett et al., 2011; Baker et al., 2004)*. **Figure 2.8** shows viscosity data for readily available Tate & Lyle golden syrup alongside data from some different glucose-based syrups which have a very different chemical make-up. This highlights how viscosities are affected by both temperature and dilution, but also how there is great variation between syrup types.

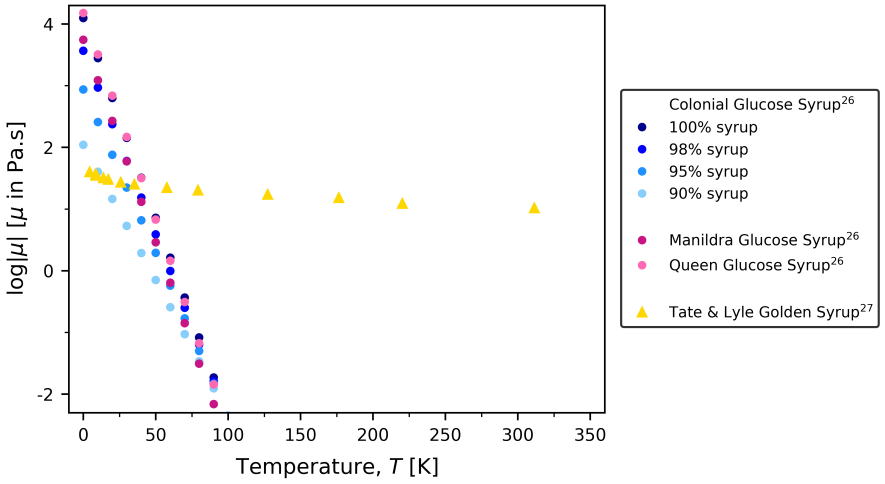

Figure 2.8: Viscosity variance with temperature for several sugar syrups at different dilutions. Glucose syrups have a different bonding structure to golden syrup which is a sucrose-based syrup, which is reflected in the viscosity-temperature trend. References for the datasets are given in a table in **Appendix I**.

In **Chapter 6** of this thesis golden syrup is used to observe mass transfer of gaseous species during bubble rise on a laboratory scale at standard temperatsures and pressure. The results from these experiments are then extended to discuss decoupled bubble resorption in natural magmatic melts and the implications of this.

Hypotheses

Following a review of previous literature on magmatic bubble systems and the fluid dynamics underpinning the study bubbles and bubble resorption in highly viscous fluids, hypotheses on the work in this thesis can be set out. Taking into consideration the two different numerical definitions of Péclet number, the ability for diffusive mass trasnfer to occur in systems where there is sufficient solubility or concentration gradient, and the ablility for bubbles to be either coupled or decoupled with respect to the fluid surrounding them, it is hypothesised that:

1. The suite of dimensionless Péclet numbers can be used to describe different types of bubble system in respect of whether they are able to undergo resorption and what drives that resorption. The dimensionless Stokes number can be used to describe if a bubble and surrounding fluid are coupled or decoupled. Combining the use of Péclet number and Stokes number, systems where bubbles may be coupled or decoupled in addition to udergoing resorption or not will be able to be described.

2. Two further definitions of Péclet number can be used by considering the different types of advection: the movement of melt inwards around a shrinking bubble (melt shell response) or the movement of melt around a rising bubble (bubble rise). These will be the stationary and buoyant Péclet numbers, Pe_s and Pe_b respectively.

3. For systems described by stationary Péclet number:

   o High values define systems where diffusion occurs slower than the melt shell response, so the bubble will resorb at the rate of diffusion.

   o Low values define systems where diffusion occurs faster than the melt shell is able to respond, leading to overpressure in the bubble and the sudden collapse of bubbles following removal of the gaseous species via diffusion.

4. For systems described by buoyant Péclet number:

   o High values define systems where bubbles rise much faster than the gas is able to diffuse, leading to less diffusion and resorption as the bubble is in contact with melt for a shorter period of time.

   o Low values define systems where bubbles rise much slower than the rate of gas diffusion, so that bubbles resorb faster as they are in contact with melt for longer.

5. In systems described by Pe_b, there will be a point at which bubble buoyancy is so small in relation to the melt that it can be considered as effectively stationary with no rise velocity. At this point Pe_s would provide a better description of the system.

6. Each value of Péclet number is unique to a systems as a result of the gas and fluid present. These unique values help define a specific system regime in which a bubble will have a specific behaviour. There will also be limits to each of these regimes, occurring at specific value of Pe_b or Pe_s.

7. There will be four major types of bubble regime that are dependent on the degree of diffusive mass transfer and bubble-fluid coupling:

   o Stationary, non-resorbing – no significant mass transfer in a coupled system

   o Stationary, resorbing – significant mass transfer in a coupled system

   o Buoyant, non-resorbing – no significant mass transfer in a decoupled system

   o Buoyant, resorbing – significant mass transfer in a decoupled system

8. Further dimensionless analysis of bubble radius evolutions with time using different normalisations will highlight the onset of different system limits as well as enabling the transition between systems where resorption is dominant or not to be identified. It is initially thought that this transtition will occur around a Péclet number of 1.

9. Applying conditions for various volcanic systems will produce a spectrum of different Péclet number values that will allow for interpretation of the effects that limit or enhance bubble resorption in natural system.

3.1 Graphical Hypothesis

To provide a visual representation of the four major types of bubble regime that are hypothesised, and their relation to one another in terms of Péclet and Stokes numbers, a graphical hypothesis is devised. This shows the expected relative values of Pe_b, Pe_s and Stk at which different bubble regimes will be found.

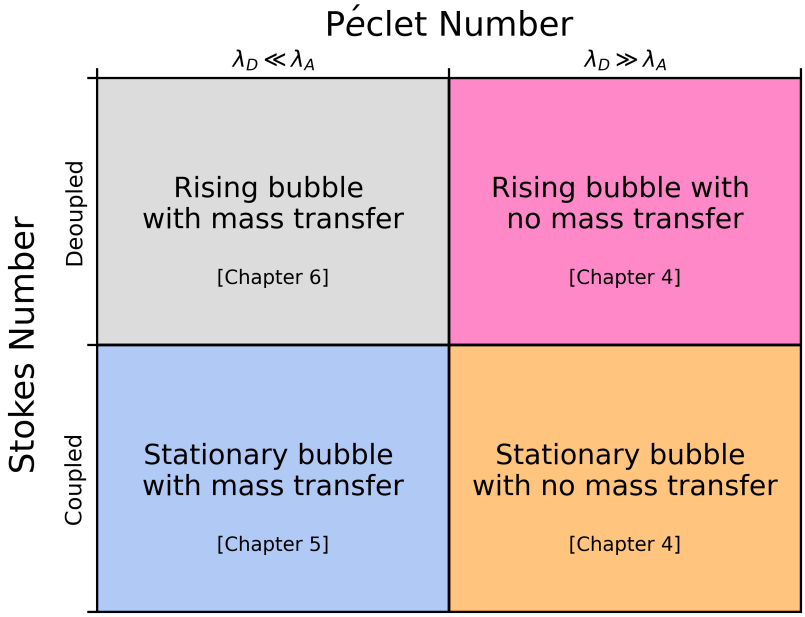

Figure 3.1: Image representing a graphical hypothesis of the four different major bubble regimes. These are displayed in relation to one another in terms of Stokes and Péclet number. The relevant chapters exploring each of the different regimes is also displayed.

Non-Resorbing Bubble Systems

This chapter explores bubble-melt interactions in systems where significant mass transfer does not take place, meaning bubbles undergo growth or shrinkage rather than resorption. Such systems can occur in two main ways, (1) when the timescale of diffusion is significantly greater than the timescale of advection, or (2) when the bubble and melt are in chemical equilibrium so there is lack of a concentration gradient. In the latter case, no mass transfer would occur as there would be zero potential for the gas species to move into the melt. However in first case, transfer of mass between the bubble and melt may still be occurring but over such a long timescale that it is negligible compared to any advection of the bubble due to buoyant rise or pressure-temperature-controlled growth.

In the majority of this thesis, a general assumption is made that system conditions are isobaric and isothermal so that changes to bubble size result only from mass transfer. However, in this chapter, some non-isothermal and non-isobaric cases are discussed to demonstrate the controls that act on bubble systems where mass transfer is negligible. These changing conditions are applied to the two endmember cases of coupled and decoupled bubbles in systems where mass transfer is negligible.

4.1 Coupled Bubbles

In addition to sitting in a low-Stokes number, coupled regime, bubble-melt systems may also be subject to conditions that result in little to no mass transfer.

Considering this in the context of Péclet number regimes, the coupled nature of the systems means they are described by the stationary Péclet number Pe_s, with the advective timescale referring to the melt shell response timescale for the viscous relaxation of the bubble wall, λ_v **(see 2.2.2.1)**. In a system where λ_v is significantly shorter than λ_D so that there is little to no mass transfer, bubble size will be solely controlled by the pressure or temperature of the system as the fixed quantity of gas in the bubble expands or contracts in response, and the surrounding melt advects to accommodate it. These types of pressure-temperature controlled, coupled systems are described by very large values of Pe_s as $\lambda_D \to \infty$ relative to λ_v.

4.1.1 Pressure-Temperature Controlled Bubbles

Gas bubbles will expand or contract in accordance with an equation of state such as the ideal gas equation. This highlights the proportionality of gas volume to temperature, T and inverse proportionality to pressure, p. Using this equation, the equilibrium radius, R_∞ of a spherical gas bubble under any conditions can be determined as,

$$R = \sqrt[3]{\frac{3nR_gT}{4\pi p}} \tag{4.1}$$

where R_g is the gas constant and n the number of moles of gas in the bubble, taken to be fixed when there is no mass transfer.

The effects of pressure and temperature in high Pe_s systems can be demonstrated using a numerical model for stationary bubble growth *(Coumans et al., 2020)* **(see Chapter 5)**. Applying a very low diffusivity ($O(10^{-20})\mathrm{m}^2\mathrm{s}^{-1}$) to replicate negligible mass transfer conditions, means pressure and temperature responses become the only things simulated by the model, reducing its functionality to an iterative solver of **Equation 4.1**. More complex applications of the stationary bubble growth model are set out in **Chapter 5** alongside a more detailed description of its design.

Input conditions are set to simulate shrinkage of a water vapour bubble in rhyolitic obsidian from Krafla, Iceland. Testing the model with isothermal-isobaric conditions shows that there is no bubble shrinkage when mass transfer is negligible and temperature and pressure are constant **(Fig.4.1a)**. Applying a sudden temperature drop at fixed pressure results in bubble shrinkage in line with the ideal gas equation **(Fig.4.1b)** as the rapid cooling causes gas in the bubble to contract resulting in a new, smaller equilibrium radius. Bubble shrinkage is also observed by applying a sudden pressure increase at a fixed temperature **(Fig.4.1c)**, causing the gas bubble to contract to a smaller equilibrium radius, again in-line with **Equation 4.1**.

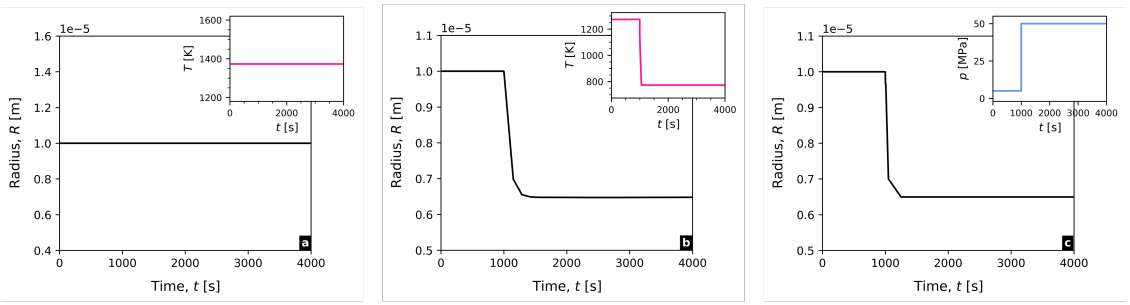

Figure 4.1: Outputs from the bubble growth model (Coumans et al., 2020) showing how in systems where there is no mass transfer, bubbles can shrink as a result of pressure or temperature changes. **(a)** Constant conditions result in no changes to the bubble. **(b)** A sudden drop in temperature or **(c)** a sudden increase in pressure causes contraction of the bubble to a smaller equilibrium radius in line with the ideal gas law.

4.2 Decoupled Bubbles

The opposing endmember case to coupled pressure-temperature-controlled bubbles is high-Stokes number systems where the bubble is decoupled from the melt.

In this case is described by the buoyant Péclet number, Pe_b as a relative velocity between the bubble and melt means the advective timescale instead describes the buoyant rise timescale λ_b **(see 2.2.2.1, Eq.2.16)**. Bubble rise timescales are principally determined by the terminal rise velocity (TRV) of the bubble, which is in turn affected by parameters such as bubble radius, or material densities and viscosities **(Eq.2.15)**.

Where decoupled systems also experience negligible mass transfer, they will be described by high values of Pe_b, as λ_D will be significantly longer than λ_b. Large radius bubbles moving through low density and viscosity melts will have the highest Pe_b values, tending towards infinity. Smaller radius bubbles moving through denser, higher viscosity melts will have lower Pe_b values until eventually the melt shell response timescale becomes more limiting than the response to buoyant rise. Therefore, at low values of Pe_b, there is a transition towards a coupled-style regime more suitably described by Pe_s.

4.2.1 Bubble Rise in Isothermal-Isobaric Conditions

Under isothermal and isobaric conditions, many parameters of a decoupled bubble-melt system can be considered as constants, including the viscosities and densities of the gas and melt. Therefore, TRV and by extension λ_b and Pe_b of a given system at a fixed temperature and pressure will vary only with the initial bubble size.

These controls on bubble TRVs have been determined from experimental studies conducted in high-viscosity fluids *(Jucha et al., 1982; Hornyak and Weinberg, 1984; Li and Schneider, 1993)*, result from which have enabled the experimental validation of the Hadamard-Rybczynski (H-R) solution for isothermal conditions, which underpins the definitions of λ_b and Pe_b.

Jucha et al. (1982) used a novel transparent furnace system to observe the rise of air bubbles in boron-silicate (borate) glasses at several different temperatures. This altered the glass properties for each run, resulting in varying bubble rise velocities, demonstrating that TRVs are highly dependent on glass melt viscosity. Furthermore, their results confirmed that the bubble rise motion is better described by the Hadamard-Rybczynski solution than the previously used Stokes solution. Hornyak and Weinberg (1984) used a different experimental system to produce similar observations but this time between bubbles of oxygen, CO_2 or air a soda-lime-silicate glass melt. Their results again confirm that the evolution of bubble rise is best described by the H-R solution compared with the Stokes solution **(Fig.4.2a)**. The final study by Li and Schneider (1993) measured the rise velocities of helium bubbles in high-viscosity oils using a computerised detection system to track the bubble movement through the melt. This added a further dataset of evidence to support the use of the H-R solution to describe bubble motion in high-viscosity fluids **(Fig.4.2b)**.

Figure 4.2 displays a selection of results from these past studies highlighting the excellent fit of the H-R solution for bubble rise in isothermal, isobaric, low Reynolds number systems, as

well as confirming the key control that temperature and bubble size has on TRVs. Therefore, by extension, these, along with pressure that would also affect viscosities and densities, can be confirmed as major controls on λ_v and by extension the value of Pe_b for decoupled systems with limited mass transfer.

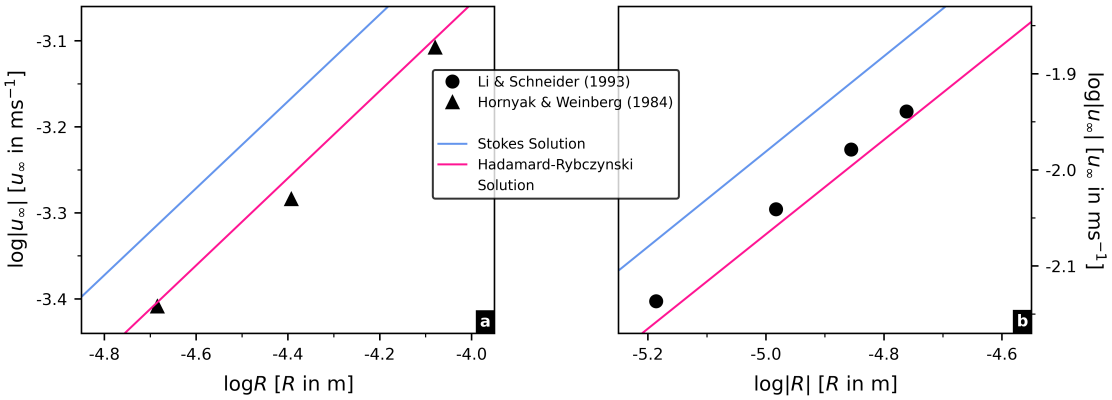

Figure 4.2: A selection of data from past observational studies of non-resorbing bubbles rising in isothermal-isobaric (a) soda-lime-silicate glass melt, and (b) high viscosity oil. In both cases, the data across a range of bubble radii are better described by the Hadamard-Rybczynski solution than the Stokes solution.

4.2.2 Bubble Rise in Non-Isothermal-Isobaric Conditions

Under conditions where temperature and pressure are not constant with time, the parameters of the gas-fluid system that were previously considered as constants (μ, ρ, and R), will now vary. A study on the effect of non-isothermal conditions on TRVs Jackson et al. (2022) used an integral form of the Hadamard-Rybczynski equation **(Eq.4.2)** to account for temperature-related changes to melt density, viscosity, and bubble radius, to find bubble position over time.

$$x = \frac{g}{3}\int_0^t \frac{R^2\Delta\rho}{\mu_0}, dt \tag{4.2}$$

This solution was tested against experimental data collected from the entrapment of air bubbles in soda-lime-silicate glass. Various heating and cooling cycles were applied to the system to generate different non-isothermal conditions, with the integral solution providing a better description of the observed bubble motions than if isothermal conditions were assumed.

Therefore, this study further confirms that μ, ρ and R are all key controls on TRVs in high-viscosity melts and that TRVs can change in response to changes in system conditions. By extension, the findings of this study suggest that in non-isothermal or non-isobaric systems, the values of λ_v and Pe_b may change in space or over time such that systems may fluctuate between dynamic regimes. This additional complexity is not analysed further in this study but is included here for consideration and discussed again in **Chapter 7**.

4.3 Implications for Volcanology

4.3.1 Coupled Systems

There are several plausible volcanic settings where coupled bubble-melt systems may exist without significant mass transfer. Firstly, bubbles moving rapidly upwards through a conduit coupled to a low viscosity basaltic melt. The bubbles would experience changes in size controlled only by pressure or temperature variation, as the rate of diffusive mass transfer would be significantly slower than that of the melt shell response to the expansion of the gas in the bubble. This setting would be defined by high Pe_s values.

A second setting, more akin to a system where the bubble and melt are both stationary, concerns bubbles sitting within a volatile-saturated, cooling rhyolitic lava. In this case, there will be little to no diffusion of the gas species into melt, meaning despite its high viscosity, the melt shell response around the cooling, contracting gas would be relatively fast. This high Pe_s setting would produce magmatic material with entrapped bubbles and a noticeable absence of the diffusive haloes observed in studies by Watkins et al. (2012) or McIntosh et al. (2014) for resorbing bubbles.

As **Figure 4.1** demonstrates, in high Pe_s systems, changes to the system conditions appear to be a much greater control on bubble size. In a volcanic setting where pressure varies with depth and conduit temperatures are in constant flux, understanding how bubbles respond and how these responses might act to enhance or limit an eruption is paramount.

4.3.2 Decoupled Systems

Despite there being no direct measurements or observations of bubble rise velocities in magmatic melts, results from studies using suitable analogues of oils and silicate glasses have been able to describe TRVs well using forms of the Hadamard-Rybczynski solution. Future work could aim to better this by measuring bubble rise more directly in magmatic material. For this, the preparation technique employed by Wadsworth et al. (2022) could be combined with the non-isothermal methodology adopted by Jackson et al. (2022) and to make direct observations of bubble rise in non-analogue melts. This would provide comprehensive validation of the H-R equation to describe bubble rise directly in magmatic melts; but even without this, the collection of past work is sufficient to justify the use of the H-R solution to generate an expression for the characteristic bubble rise timescale, λ_b **(Eq.2.16)** used here to calculate the buoyant Péclet number of decoupled bubble-melt systems.

High-Pe_b, decoupled systems where no significant mass transfer takes place are plausible in volcanic settings. One such setting is where small bubbles sit within an ultramafic melt where melt viscosity is very low. As a result, the bubbles would rise very rapidly relative to the melt, enhancing processes such as fragmentation which result in fountaining, Hawaiian-style eruptive behaviours.

Another plausible setting for decoupled, non-diffusive bubble rise is where the surrounding melt is saturated. Here, even in very high-viscosity silicic melts, bubbles would have a buoyant rise timescale shorter than that of the diffusive timescale due to the lack of volatile concentra-

tion gradient. Coupling this with non-constant temperature-pressure conditions, unreactive bubble rise could occur in settings such as lava lakes or cooling lava flows where temperature or pressure vary with time and space.

Coupled, Resorbing Bubble Systems

In this chapter, systems where diffusive mass transfer is no longer negligible begin to be introduced, with coupled bubbles resorbing into the surrounding melt. The bubbles in these low Stokes number (Stk << 1) systems can be considered as stationary relative to the melt such that any reference to advection is to viscous relaxation rather than buoyant rise.

The stationary Péclet number (Pe_s) is used to describe the regimes of these coupled resorbing systems with λ_D as the diffusive timescale and λ_v as the advective timescale for viscous relaxation of the melt around the shrinking bubble. Variations in the conditions of the system will result in variations to both λ_D and λ_v and as a result, the value of Pe_s. Therefore, this type of system no-longer represents an endmember scenario and instead a whole spectrum of different Péclet numbers depending on whether the diffusive or viscous timescale is dominant. This range of Pe_s equates to different bubble-melt dynamics as parameters of the systems such as viscosity, diffusivity, or solubility change. As a result, the evolution of bubble radii over time will vary from system to system as either diffusion or viscosity act to limit the resorption and the degree of bubble shrinkage.

In this chapter, observations of coupled bubble resorption are briefly discussed before more numerical analysis is presented using an adaptation of a model for bubble growth and shrinkage. Simulations of bubble resorption from this model are used to highlight the different Péclet number regimes as well as the onset of the viscous and diffusive limits. Solutions for the evolution of bubble radii with time at and between these limits for any given coupled gas-melt system are also set out. Finally, the significance of these findings for natural systems such as basaltic or rhyolitic melts is discussed to demonstrate the application of this non-dimension analysis to wider settings.

5.1 Previous Observations of Stationary Bubbles

Central to this chapter of work is a previous study by Coumans et al. (2020) in which a numerical model for bubble growth is presented. Alongside the numerical model **(see section 6.2**), they give experimental observations of stationary bubbles changing size as a result of mass transfer.

They monitored the porosity of rhyolitic obsidian samples from Hrafntinnuhryggur, Krafla (Iceland) following heating at a constant rate to a hold temperature between $930 - 1000°C$ under isobaric conditions. Over the course of the experiments, an increase in the gas volume fraction (ϕ) of the samples was observed. This occurred as a result of H_2O transfer from the melt, leading to bubble growth, even when corrected for expansion due to the temperature increase. The rate of growth appeared vary over time, starting off slow before accelerating in response to the increase in temperature which would as have reduced the viscosity of the surrounding melt. As the samples reached the hold temperature, the rate of volume change slowed again as the bubbles reached an equilibrium state under the constant conditions.

Coumans et al. (2020) highlight the similarity of these findings to Ryan et al. (2015) who also investigated H_2O mass transfer in obsidian, observing an increase in gas volume fraction following the heating of the same Hrafntinnuhryggur rhyolitic obsidian at a constant high temperature. They however attribute the additional observation of the varying growth rate to be significantly controlled by the changing viscosity of the surrounding melt, given the correlation of growth rate to the changes in temperature over time.

Alongside their new experimental observations, Coumans et al. (2020) compile data from decompression experiments where pressure is changed under isothermal conditions *(Burgisser and Gardner, 2004; Mourtada-Bonnefoi and Laporte, 1999; Hamada et al., 2010)*. Each experiment exposed various rhyolite samples to reduced pressures at a fixed temperature, measuring the initial and final gas volume fraction to estimate bubble growth. Under these conditions, changes to the gas volume fraction were concluded to occur principally as a result the equation of state for H2O, increasing as the pressure is decreased. Furthermore, results from Burgisser and Gardner (2004) where the samples underwent an isobaric quench at the end of the experiment provided further supporting evidence for the control of viscosity on bubble growth, as gas volume fraction reduced during the rapid decrease in temperature.

This work is appropriate to review here as it discusses mass transfer processes in natural magmatic melts, however, the work mainly focuses on bubble growth and doesn't discuss the possibilities of bubble shrinkage or resorption to a very large extent.

A second previous work on stationary bubbles by Doremus (1960), presenting experimental observations from Greene and Kitano (1959), instead focuses on bubble shrinkage but in molten glasses rather than naturally occurring melts. Given that molten glass is an appropriate analogue for magmatic material **(see Section 2.3.2.1)**, results from this study are appropriate to present here and provide evidence for diffusive mass transfer leading to the resorption of a gas species into surrounding melt, and the shrinking of a bubble phase.

Greene and Kitano (1959) monitored individual millimetre-scale oxygen bubbles in borosilicate and barium-alkali-silica glass melts for several hours to track bubble radius evolution with time instead of measuring changes to the gas volume fraction of a sample with multiple bubbles. The transparent properties of the glasses compared to obsidian, and the novel experimental apparatus developed allowed this to be possible.

The results show that the rate of bubble shrinkage is significantly dependant on the glass used and the temperature of the experimental run, with bubbles of the same initial radius shrinking faster when the same glass is increased in temperature. Similarly, to Coumans et al. (2020),

this can be attributed to reduction of melt viscosity with increased temperatures, which acts to limit bubble volume change. Furthermore, the results suggest that the rate of bubble shrinkage varies depending on bubble size, with the radius of initially larger bubbles reducing faster than those that were initially smaller.

Overall, these previous works provide a substantial base of evidence for bubble growth and shrinkage to build upon and better understand. Evidence that such diffusive mass transfer processes can take place in both naturally occurring and analogue melts warrants investigation of the physical laws and relationships that control mass transfer and the resulting bubble volume change, as well as the system parameters that act to control these changes.

5.2 Modelling Bubble Radius Evolutions

The past works of Coumans et al. (2020) and Doremus (1960) also present models for bubble radius evolutions over time which they test against the experimental data collected. Doremus (1960) derives a solution from equations for solute flux, J around the surface of a sphere, and the concentration gradient between the bubble, bubble wall and distant melt. Their analytical solution is given as,

$$R(t)^2 = R_0^2 - 2D\beta t \left[\frac{2R_0}{\sqrt{\pi D t}}\right] \tag{5.1}$$

where R_0 is initial bubble radius, D is the diffusion coefficient, and β takes the form of a concentration gradient.

Comparison of this solution to the experimental data from Greene and Kitano (1959) **(Fig.5.1)** shows that it provides a good fit for bubbles in the barium-alkali-silicate glass and for bubbles in the borosilicate glass at lower temperatures. At higher temperatures, the solution matches well for the initial evolution of bubble radius but deviates away from the observed data with time. Greene and Kitano (1959) originally attribute this to the presence of a secondary gas in the bubble that doesn't diffusively transfer in the glass melt or diffuses at a much slower rate than the oxygen. Therefore, this secondary gas remains in the bubble phase after the oxygen has been removed, limiting bubble shrinkage beyond a certain radius.

Doremus (1960) alternatively suggests that the size of the glass rods used were too small to accommodate all of the oxygen mass from the bubble. As a result, the concentration gradient between the bubble and distant melt would decrease over time as oxygen is transferred and diffuses throughout the melt. Eventually, the oxygen concentration in the distant melt is large enough for mass transfer to be significantly reduced and therefore the observed bubble shrinkage rate is slower than predicted from the solution.

The model by Coumans et al. (2020) is much more comprehensive, starting from a well understood form of the Rayleigh-Plesset equation which describe the dynamics of spherical bubble growth as a result of pressure difference between the gas in the bubble p_g and melt p_∞, viscous pressure p_v and surface tension pressure p_s.

$$p_\infty - p_g + p_v + p_s = 0 \tag{5.2}$$

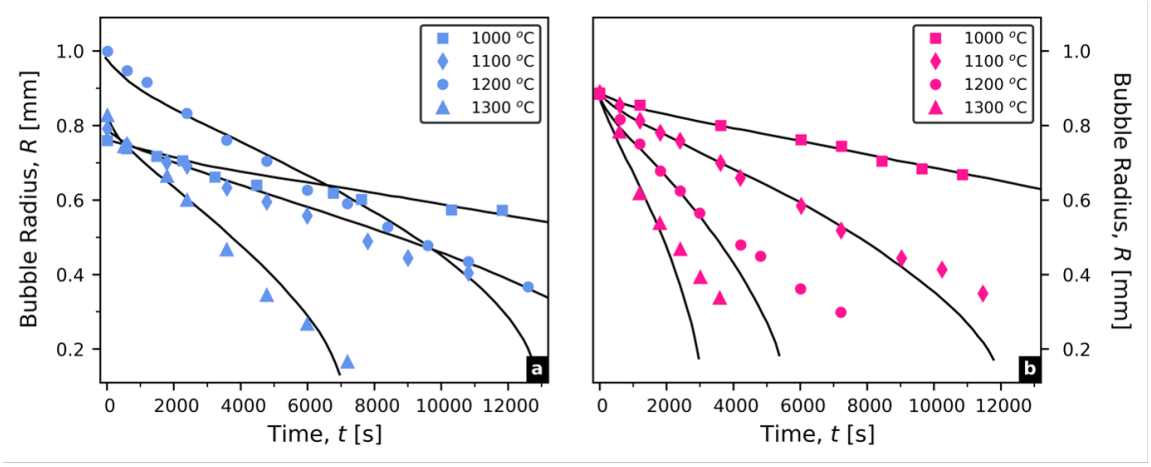

Figure 5.1: Experimental data from Greene and Kitano (1959) showing the shrinking of oxygen bubbles in molten **(a)** barium-alkali-silicate glass, and **(b)** borosilicate glass at various different temperatures. The black lines show solutions for bubble radius evolutions modelled by Doremus (1960) **(Eq.5.1)**. These solutions have the best fit in lower temperature melts and the barium-alkali-silicate glass, however there is visible variation between the model solutions and observation across all datasets.

They expand upon the terms of this equation by setting out various other governing equations that would affect the volume change of a spherical bubble in an incompressible fluid where inertial effects are negligible (low Reynolds number systems). To do this, they define the bubble as being surrounded by a 'melt shell' which can grow or shrink in response to volume change in the bubble. It is between this shell and the bubble that mass transfer will occur, and thus it can be said to have a concentration gradient from c_i at the bubble wall to c_∞ at the exterior wall of the melt shell that will help to drive mass transfer. For a bubble that will grow, $(c_i < c_\infty)$ such that mass moves from the melt into the bubbles, whereas for a shrinking bubble, $(c_i > c_\infty)$ which tends towards zero resulting in the movement of mass from the bubble into the melt.

Into this melt shell model approach, governing equations for diffusivity, solubility, equation of state and viscosity are incorporated. Viscosity, μ is of particular significance in their model as is built to describe the diffusion of water into magmatic melts, which could alter significantly in viscosity as a result **(see 2.3)**. Therefore, with each timestep of the model, as water is released into or removed from the melt, its viscosity needs to be recalculated.

Finally, they consider the potential effects of non-isothermal and non-isobaric conditions on these different governing equations and therefore the bubble radius evolution. This enabled them to run simulations for conditions such as those they measured experimentally, and for a wider context, allows conditions more akin to those of a natural volcanic system to be tested.

The model is coded into *MATLAB* for execution and run through a series of scripts that ultimately solve a series of ordinary differential equations to integrate their solution for bubble radius change with time. Different input conditions can be entered such as initial bubble radius, gas volume fraction, melt density and pressure-temperature profiles. The governing equations for solubility, diffusivity, viscosity and equation of state can also be changed to be most specific to the melt and gas being simulated.

5.3 Simulations of Bubble Resorption & Shrinkage

The outputs of the Coumans et al. (2020) bubble growth code include profiles for bubble radius and gas volume fraction over time. These give a clear indication as to whether a bubble is undergoing diffusive growth or resorption.

In the remainder of this chapter, the method used to adapt this code for unique use in this study is set out, and the resulting simulations presented for analysis. This adaptation of the code enables bubble radius profiles to be generated for systems where resorption and therefore shrinkage occur. These simulations help better understand the controls on these processes and the onset where either viscosity or diffusion becomes the limiting control.

5.3.1 Adaptation of the Model for Bubble Shrinkage

In order to investigate the effects of different parameters on bubble shrinkage, the bubble growth model needed to be adapted so that the parameters could be changed individually and systematically. To explore the 'simplest' case scenario to start with, the code also needed to be changed so that parameters such as melt viscosity didn't change with time during the model runs. The code was set up using an analogue gas-glass system where it known that the gas would diffuse well into the glass as its composition is undersaturated in that species. The well-studied soda-lime-silica glass Cristalica was used as it has a known composition, and helium was chosen as the gas phase. To incorporate these into the code, the chemical make-up and density of Cristalica were set as an input, and the molecular mass M_m of water was changed to that of helium throughout.

Next, the individual laws for solubility, diffusivity, viscosity and equation of state had to be adapted. The original code was designed so that pressure-temperature-concentration dependant laws for each of these, that would change over time, could be entered. In the adapted code, the laws for diffusivity and viscosity were changed to be fixed, constant values throughout the entire run, which allowed for the investigation of the viscous and diffusive limits. The equation of state was maintained as the ideal gas law **(Eq. X)** except with the molecular mass of helium instead of water. The solubility law was changed to be a simple equation following Henry's law **(Eq.X)**, where the value of the Henry constant could be changed to control the ability for the bubble to be completely resorbed or not.

For the other input settings, the system conditions were set to be isothermal and isobaric, surface tension and the gas volume fraction were given fixed values and the initial bubble radius could be set to a required length. Therefore, the code could be run for different bubble radii, different values of viscosity or different values of diffusivity, either in sequence or in combination.

The time of the simulation for each run completed was extended so that the bubble always underwent complete resorption. Data for the bubble radius evolution over time was printed as an output for each simulation along with the exact input conditions to complete further analysis with.

5.3.2 Processing Simulation Outputs

Running the code multiple times, each with varying inputs results in a large range of bubble sizes and systems for which the radius evolutions with time need to be made comparable. In order to do this, a series of normalisations are carried out on the output radius-time data from the *MATLAB* code. These normalisations non-dimensionalise the datasets, enabling radius evolutions for bubbles of different sizes and for different gas-melt systems to be plotted in a single dimensionless space.

5.3.2.1 Normalised Radius

Firstly, to make bubbles of different sizes and their shrinkage rates comparable, the radii need to be normalised. The simplest way of doing this is to divide the radius value at each timestep of the simulation by the initial input radius to give $\bar{R}$, the normalised radius.

$$\bar{R} = \frac{R(t)}{R_0} \tag{5.3}$$

This means all radius data now starts at a value of one and decreases over time towards zero. If the bubble is completely resorbed, $\bar{R}$ will become zero.

5.3.2.2 Diffusion Normalised Timescale

To help identify the onset of the diffusive limit in a bubble-melt system, where diffusivity becomes the controlling factor, the timescale over which bubble radius is simulated needs to be normalised. Normalising time to a characteristic diffusive timescale gives $\bar{t_D}$, the diffusion normalised time,

$$\bar{t}_D = \frac{tD}{R_0^2} \tag{5.4}$$

where D is the diffusion coefficient of the gas into melt. $\bar{t_D}$ is independent of viscosity, highlighting how this normalisation helps to show systems where diffusion is the limiting effect. For systems that sit at this diffusive limit, bubble radius evolutions in dimensionless space should be the same, regardless of any other changes to the inputs or parameters.

5.3.2.3 Viscous Normalised Timescale

The viscous limit of a bubble-melt system, where viscosity of the melt becomes the controlling factor, can be found using a second normalisation of time. Normalising time to a characteristic viscous timescale that depends on melt pressure, p_0 and viscosity, μ gives the viscous normalised time $\bar{t_v}$.

$$\bar{t}_v = \frac{tp_0}{4\mu} \tag{5.5}$$

The independence of $\bar{t_v}$ to the diffusion coefficient shows how at this point, viscosity is the limiting parameter of the system. Similarly to the diffusive limit, systems that sit at the viscous limit will have the same radius evolution for resorption in dimensionless space.

5.3.2.4 Capillary Timescale

In systems where surface tension dominates, most commonly when the bubble in the melt is very small, the capillary normalised time, $\bar{t_c}$ may be useful. This normalises time using surface tension, Γ viscosity and the initial bubble radius.

$$\bar{t_c} = \frac{t\Gamma}{\mu R_0} \tag{5.6}$$

Using this dimensionless timescale enables bubble radius evolutions for initially very small bubbles to be compared.

5.3.3 Analogue Simulation Results

In order to test the effects of changing diffusivity, viscosity and solubility on different sized bubbles, several series of model simulations were completed. This helped to build a better understanding of how each parameter affected the system and the resulting bubble radius evolutions. The results shown here are a compilation of the different simulations from each of these series of tests, selected and combined to give the best demonstration of the findings. Firstly, results from the analogue gas-glass system on Cristalica and helium are presented. These represent a 'simplest case' simulation where each parameter has a fixed value for the duration of bubble shrinkage. Viscosity, diffusivity and initial radius were varied sequentially to generate different bubble radius evolutions ($R(t)$ evolutions). The outputs from the *MATLAB* code were reduced using the different non-dimensionalisations to give graphs of $\bar{R} - \bar{t}_D$ and $\bar{R} - \bar{t}_v$. An example output is shown in **Figure 5.2**, which shows $R(t)$ curves for bubbles of different initial radii with fixed values for μ, D and S.

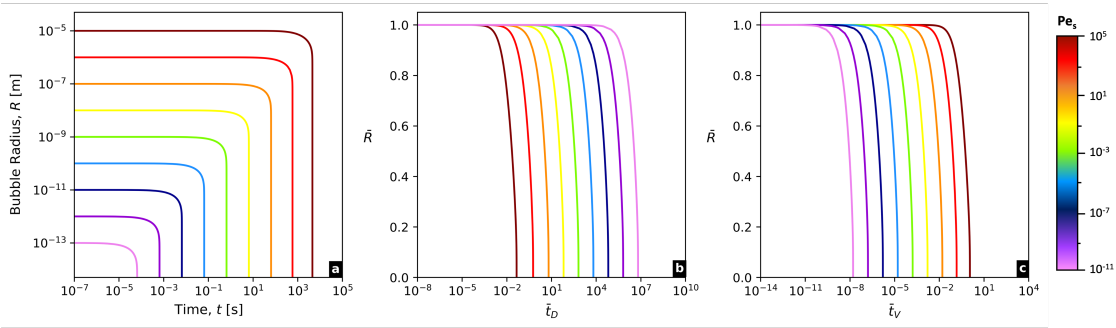

Figure 5.2: Simulation results from the adapted bubble growth code, run for bubbles of varying radii in a fixed condition system where $\mu = 10^8$Pa.s and $D = 10^{-15}$m^{2}s^{-1}. Each bubble is described by a different value of Pe_s indicated by the colour bar and has a unique bubble radius evolution in **(a)**dimensional space as well as **(b)** diffusion-normalised, and **(c)** viscosity-normalised dimensionless space. The value of Pe_s increases from right to left in $\bar{R} - \bar{t}_D$ space, but from left to right in $\bar{R} - \bar{t}_v$ space.

Figure 5.2 demonstrates how each bubble has a unique $R(t)$ evolution in both dimensional and dimensionless space. A further observation comes when Pe_s for each $R(t)$ curve is calculated from the model inputs. In **Figure 5.2**, each curve is coloured according to its order of magnitude value of Pe_s, showing a trend of increasing stationary Péclet number from left to right in dimensional space, driven by the factor two proportionality of Pe_s to R_0. There are also trends in the dimensionless figures, with values of higher values of Pe_s on the left in dif-

fusion normalised space **(Fig.5.2b)**, but on the right in viscous normalised space **(Fig.5.2c)**.

When comparing $R(t)$ curves between simulations of different systems where viscosity or diffusivity were set to different values, curves with the same order of magnitude of Pe_s align in dimensionless space to the exact same curve **(Fig.5.3)**. This leads to the conclusion that regardless of the input conditions, systems with the same magnitude of Pe_s have a unique bubble radius evolution in dimensionless space (ie. $\bar{R}(\bar{t}_D)$ or $\bar{R}(\bar{t}_v)$). This presents the opportunity for the bubble radius evolution for any given bubble and melt to be found as long as all initial conditions of the system are known.

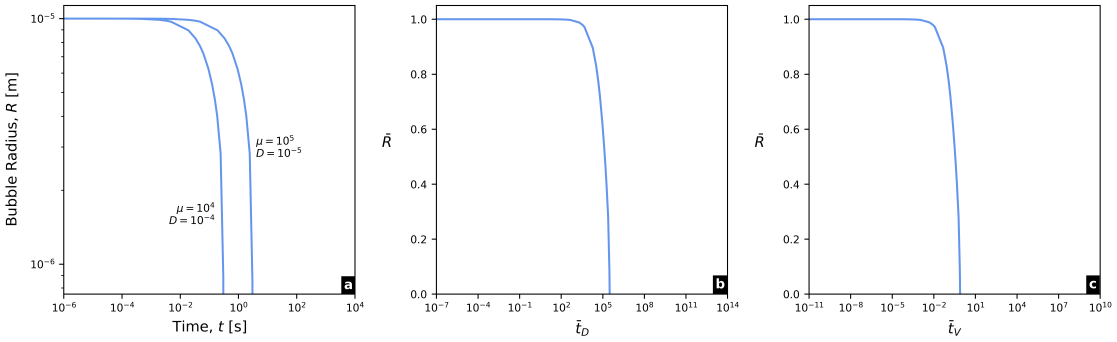

Figure 5.3: Two simulation outputs from the adapted bubble growth code, for bubbles of the same initial radius (10^{-5}m) but in systems where viscosity and diffusivity vary. The two systems are described by the same value of Pe_s ($10^{-}2$). **(a)** Bubble radius evolutions in dimensional space are different due to the different system conditions. In **(b)** diffusion-normalised and **(c)** viscosity-normalised space, the two simulations collapse to the same result. This demonstrates that these normalisations of bubble radii and time lead to systems with the same value of Pe_s having the same solution in dimensionless space, regardless of the input conditions.

Combining the results from several different simulations so that a much larger range of Pes is analysed, further observations become apparent **(Fig.5.4)**. **Figure 5.4b** shows that in diffusion normalised space, the $\bar{R}(\bar{t}_D)$ curves begin to converge to a single solution when the magnitude of Pe_s becomes greater than 10^5. Similarly in **Figure 5.4c**, the $\bar{R}(\bar{t}_v)$ curves converge to a single solution when Pe_s has a magnitude less than 10^5.

5.3.3.1 Diffusive Limit

The collapse for $\bar{R}(\bar{t}_D)$ represents the diffusive limit, where diffusivity becomes the limiting control on the system. Here, regardless of the value of viscosity, initial bubble radius or any other parameter in the system, bubble shrinkage is controlled chiefly by the value of the diffusion coefficient. Therefore, **Figure 5.4b** suggests systems where $\mathrm{Pe}_s > 10^5$ will sit in the diffusive limited regime.

5.3.3.2 Viscous Limit

The collapse of $\bar{R}(\bar{t}_v)$ in viscous normalised space represents the viscous limit, where viscosity becomes the limiting control on a system. At this limit, it is principally the value of melt viscosity that controls bubble shrinkage over any other parameter in the system. The

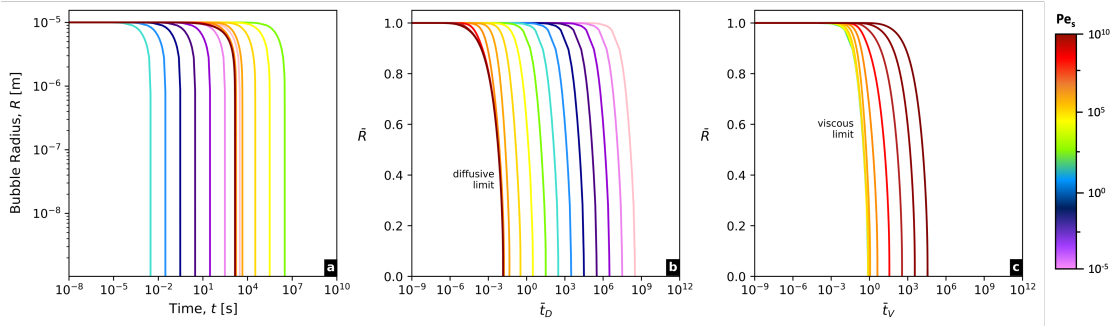

Figure 5.4: Model results combined from simulations where diffusion or viscosity are varied for a bubble of the same initial radius (10^{-5}m). Curves are coloured according to the value of Pe_s for that simulation, shown by the colour bar. **(a)** In dimensional space, there is overlapping of the data as the various different input conditions are affecting the evolution of the bubble radius. This provides evidence that normalisation of the data is required for meaningful analysis to be completed. **(b)** When time is normalised to diffusion, the curves align with increasing Pe_s values from right to left and there is collapse of simulation curves for systems with values of Pe_s greater than 10^5; the diffusive limit. **(c)** When time is normalised to viscosity, curves again align but with higher Pe_s values on the right. The simulation curves for systems with values of $\mathrm{Pe}_s < 10^5$ similarly collapse but this time to the viscous limit.

curves shown in **Figure 5.4c** suggest that systems for which $\mathrm{Pe}_s < 10^5$ will sit in the viscous limited regime.

5.3.3.3 Pe_s Regime Transition Point

Identifying the transition point between the viscous and diffusive limit, and its relationship to a value of Péclet number can confirmed through further analysis. This is done by taking the value of $\bar{t}_D$ and $\bar{t}_v$ at which each bubble has shrunk by half its original value, equivalent to when $\bar{R} = 0.5$. Plotting these values of $\bar{t}_{D0.5}$ and $\bar{t}_{v0.5}$ for each bubble against Pe_s (Fig.5.5) highlights the transition from a low-Péclet number regime where viscosity dominates and curves have the same radius evolution in $\bar{t}_v$ space, but different in $\bar{t}_D$ space, to a high-Péclet number regime where the opposite is observed.

From the results analysed so far for the analogue gas-glass system, it appears that the transition point from a low to a high Péclet number regime occurs at Pe_s. This can be concluded from both **Figure 5.4** and **Figure 5.5**. As a result, in any remaining analysis of the simulated gas-glass system, high-Pe_s regimes refer to those where $\mathrm{Pe}_s > 10^5$ and low-Pe_s regimes to those where $\mathrm{Pe}_s < 10^5$.

5.4 Solutions for Bubble Radius Evolutions

These observations of a single unique curve in dimensionless space for both the viscous and diffusive limits suggests there must be a numerical solution to describe the bubble radius evolution in these two different regimes. Next, these numerical solutions are derived from first principles and compared to the results from the model simulations to assess the extent to which they describe bubble shrinkage.

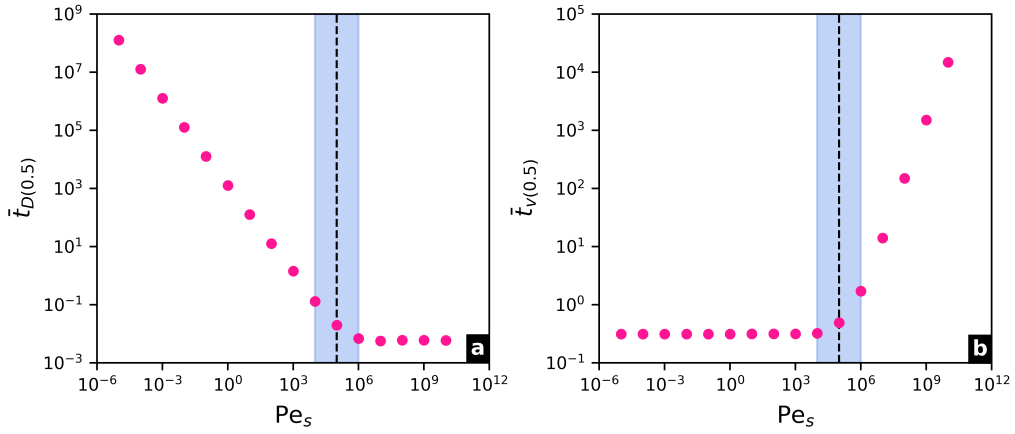

Figure 5.5: Analysis showing where the onset of the transition between the viscous and diffusive limits occurs. **(a)** The value of $\bar{t}_D$ taken when the bubble radius fall to half of the initial value against the value of Pe_s for that simulation. At Pe_s values $> 10^5$, $\bar{t}_{D(0.5)}$ has the same value for all simulations. These bubble systems sit in diffusive limited regime. For systems described by values of $\mathrm{Pe}_s < 10^5$, $\bar{t}_{D(0.5)}$ increases with decreasing Pe_s. The transition between these two types of behaviour occurs in the blue shaded region around $\mathrm{Pe}_s = 10^5$, indicated by the black dashed line. **(b)** The value of $\bar{t}_v$ taken when the bubble radius fall to half of the initial value against the value of Pe_s for that simulation. At Pe_s values $< 10^5$, $\bar{t}_{v(0.5)}$ has the same value for all simulations, meaning these bubbles sit in the viscosity limited regime. For systems described by values of $\mathrm{Pe}_s > 10^5$, $\bar{t}_{v(0.5)}$ increases with increasing Pe_s. The transition between these two types of behaviour is again indicated by the blue shaded region and occurs around $\mathrm{Pe}_s = 10^5$ (black dashed line).

5.4.1 High Pe_s Systems (Diffusion Limited)

Systems described by high values of stationary Péclet number ($\mathrm{Pe}_s > 10^5$) sit in the diffusion limited regime, where melt shell response is fast enough that the rate of diffusion is the only factor that determines the rate of bubble resorption. This is most likely due to melt viscosity being reasonably low. As a result, even if the diffusivity of a gas species is high, the diffusive timescale λ_D will be significantly longer than the melt shell response timescale λ_v, yielding higher values of Pe_s that place these systems in a diffusion limited regime.

Complete numerical solutions for the diffusion limited case of coupled bubble resorption are sparse due to the complexities of the problem. Clift et al. (2005) describe this type of system as a bubble in a stagnant continuous phase where the velocity can be considered zero everywhere. They also explain that diffusion can then only occur in the radial direction, with the diffusing species spreading out into the melt from the spherical surface area of the bubble. Using this description, Clift et al. (2005) provide an expression for the concentration gradient of the diffusing gas around a stationary or coupled bubble as,

$$\frac{\partial}{\partial r}\left(r^2\frac{\partial c}{\partial r}\right) = 0 \tag{5.7}$$

where r is the radial coordinate and c the concentration of the gas. This is the limiting case where the diffusivity of the melt, D tends to infinity in, leading to infinitely fast diffusion compared to melt shell response and thus high Pe_s values. Therefore **Equation 5.7** can be thought of as a description of the concentration of the diffusing species around a coupled bubble in a diffusion limited system.

Secondly, the model previously developed by Doremus (1960) can be thought of as a solution for bubble radius evolutions in diffusion limited systems **(Eq.5.1)** as it does not appear to factor in any effects of the surrounding melt viscosity. Instead, the radius evolution is controlled strongly by the diffusion coefficient and their factor β which is similar to a concentration gradient. However, this beta factor and its ill-described definition in their work makes it very difficult to model solutions that could then be compared to the simulations produced in this study. Furthermore, the data used by Doremus for comparison to their model was taken from a different previous study *(Greene and Kitano, 1959)* such that information on the material properties of the glasses used are missing, making it difficult to normalise the results or remodel solutions for the inputs of their experiments.

The underpinning theory of diffusion controlled stationary bubble systems is very complex as highlighted by the lack of solutions developed in previous studies and poor description of these to data outside of their measured system. As a result, a complete numerical solution for this regime is not presented in this work. The dynamics of diffusion limited bubbles have been attempted to be modelled in several other settings outside of those in viscous fluids *(eg. Srinivasan et al., 2003)*. Solutions such as these could be investigated further in future work with the aim of adapting them to develop a solution applicable to spherical bubbles in viscous fluids. The remainder of this chapter instead focuses on solutions for the viscous limited regime, where there has been a lot more development in the underlying theory allowing solutions to be derived and tested.

5.4.2 Low Pe_s Systems (Viscous Limited)

Systems described by a low value of stationary Péclet number ($Pe_s < 10^5$) sitting in the viscous limited regime are dominated by the melt shell response timescale over the diffusive timescale. Bubbles in low-Pe_s systems experience rapid diffusion of their gas species such that the bubble becomes fully vacated and significantly under-pressured. As a result of this pressure contrast, the bubble space acts like a vacuum and collapses in on itself. However, the rate of this collapse is controlled by the ability for the melt shell to respond, itself controlled by surface tension of the bubble surface and the melt viscosity. These two effects, especially viscosity, play a key role in determining the length of the advective shell response timescale (λ_v). Hence, bubbles shrinking in this type of system are viscous limited.

5.4.2.1 Complete Analytical Solution

Given that pressure contrasts help initiate bubble shrinkage, and viscosity and surface tension help control the rate of shrinkage in the viscous limited regime, the inertia-free form of the Rayleigh-Plesset equation **(Eq.6.2)** is used as the starting point to derive a numerical solution for the viscous limited regime.

Expanding out the terms for viscous and surface tension pressure, **Equation 6.2** can be written as,

$$p_\infty + \frac{4\mu}{R}\frac{dR}{dt} + \frac{2\Gamma}{r} = 0 \tag{5.8}$$

where p_∞ is the melt pressure, from the assumption that p_g is zero in $(p_\infty - p_g)$. Integration and manipulation of this equation leads to an expression for $R(t)$ in terms of melt pressure, viscosity and surface tension.

$$R(t) = R_0 \exp\left(-\frac{tp_\infty}{4\mu}\right) + \frac{2\Gamma}{p_\infty}\left[\exp\left(-\frac{tp_\infty}{4\mu} - 1\right)\right] \tag{5.9}$$

It can be noted here that the exponential term $\frac{tp_\infty}{4\mu}$ is the viscous normalised time from **Eq.6.8**. By dividing throughout by R_0, **Equation 6.11** can be written as a dimensionless solution for $\bar{R}(\bar{t}_v)$.

$$\bar{R}(\bar{t}_v) = \exp(-\bar{t}_v) + \frac{2\Gamma}{R_0 p_\infty}\left[\exp(-\bar{t}_v - 1)\right] \tag{5.10}$$

A further non-dimensionalisation can be made by considering the pre-exponent pressure term $\frac{2\Gamma}{R_0 p_\infty}$, which is the inverse of a dimensionless pressure $\bar{p}$. Incorporating this yields a completely dimensionless solution for bubble radius evolution the viscous limited regime.

$$\bar{R}(\bar{t}_v) = \exp(-\bar{t}_v) + \frac{1}{\bar{p}}\left[\exp(-\bar{t}_v - 1)\right] \tag{5.11}$$

Testing this full solution against the model simulations from **Figure 5.4** shows it provides a good fit to the simulated results that sit in the viscous regime ($\mathrm{Pe}_s < 10^5$) **(Fig.5.6)**. As expected, the solution does not fit well for results where $\mathrm{Pe}_s < 10^5$ as these sit in the diffusive regime and are better described by the diffusive limit solution.

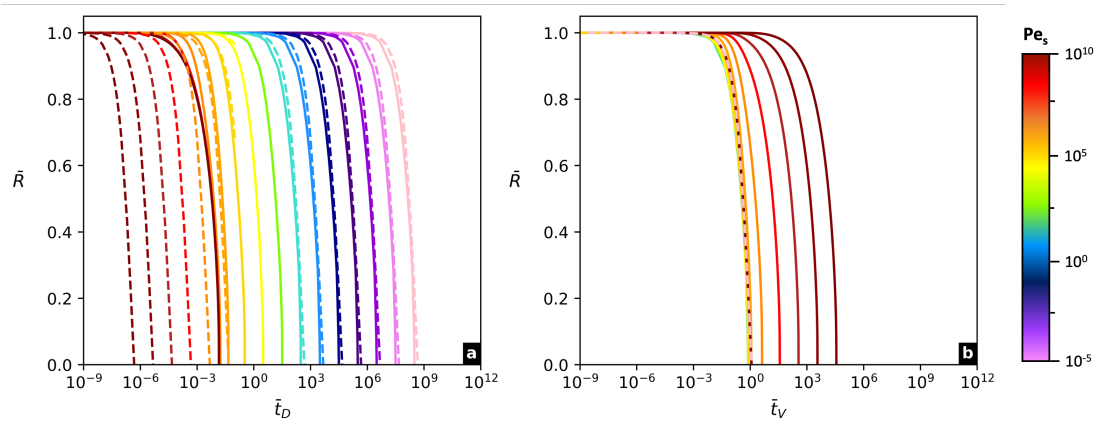

Figure 5.6: Combined model simulation results (solid lines) from **Figure ??** tested against the complete numerical solution (dashed lines) for bubble systems in the viscous limited regime **(Eq.5.9)**. All curves are coloured according to the value of Pe_s for that system, shown by the colour bar. **(a)** In diffusion-normalised space, the modelled curves fit well to those with values of $\mathrm{Pe}_s > 10^5$. The model poorly describes the collapsed solution, as expected since this collapse is for the opposing diffusion-limited regime. **(b)** The model gives a very good fit to the simulation curves that have collapsed to a single unique solution for the viscous-limited regime, but a poor fit to curves for systems with a higher value of Pe_s. This provides support for a single viscous-limited solution of bubble radius evolutions in dimensionless spaces **(Eq.5.11)**.

5.4.2.2 A Solution for Larger Bubbles

Equation 6.13 provides a complete and comprehensive solution for the viscous limit as both a viscosity and surface tension dependant term are included. A simpler form of **Equation 6.13** could be written just using the viscous term which would be valid for viscous limited systems where R_0 or p_∞ are sufficiently large that surface tension effects would be negligible, captured by large values of $\bar{p}$.

$$\bar{R}(\bar{t}_v) = \exp(-\bar{t}_v) \tag{5.12}$$

Comparison of this solution to the simulations shows it has a reasonable fit to the modelled results and again describes only those simulations in the viscous limited regime but is visibly less good than the full solution **(Fig.5.7)**. Deviation from the simulated curves is seen most dramatically towards the final stages of bubble shrinkage when the bubble radii are becoming increasingly small and surface tension would play a major role in the behaviour.

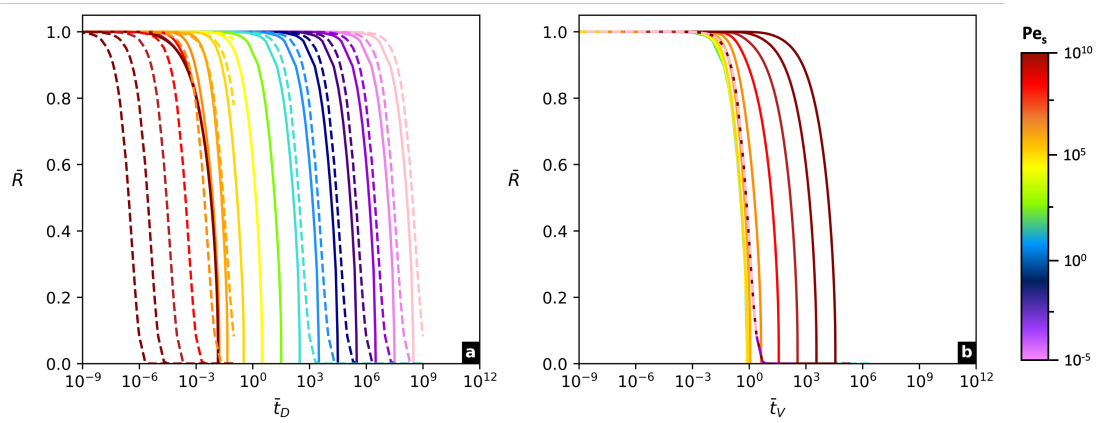

Figure 5.7: Combined model simulation results (solid lines) from **Figure 5.4** tested against the numerical solution (dashed lines) for larger bubbles in the viscous limited where surface tension effects can be neglected **(Eq.5.12)**. All curves are coloured according to the value of Pe_s for that system, shown by the colour bar. The results of this solution fit slightly less well than the complete solution **(Eq.5.9)** but still give a reasonable estimate of normalised bubble radius evolutions in both **(a)** diffusion-normalised space, and **(b)** viscous-normalised spaces for systems where the values of Pe_s is greater than 10^5.

This simplified solution gives the best fit for bubbles with a radius larger than 10^{-6}m, suggesting this might be a threshold for where bubbles can be considered as large or small. For bubbles with radii less than 10^{-6}m, the role of surface tension is too significant to be neglected, but for bubbles with a radius larger than 10^{-6}m, this solution may be appropriate. Overall, **Equation 6.14** is appropriate for finding approximate bubble radius evolutions in viscous limited systems or for settings where knowledge of the gas-melt system is insufficient to use the full solution **Equation 6.13**.

5.4.2.3 A Solution for Smaller Bubbles

A final adaptation of the full solution can be made for systems where the bubbles are small enough that surface tension is the major control on radius evolution instead of melt viscosity. For such small bubbles, the gas pressure inside the bubble becomes so great that

the pressure contrast with the melt tends to zero. As a result, the Δp term in the **Equation 6.2** can be neglected, leaving just the viscous and surface tension pressure terms. Similar integration and manipulation of this reduced Rayleigh-Plesset equation yields an expression for $R(t)$.

$$R(t) = R_0 + \frac{\Gamma t}{2\mu} \tag{5.13}$$

Normalisation of radius to R_0 results in another completely dimensionless solution where $\frac{\Gamma t}{R_0 \mu}$ is the capillary timescale $\bar{t}_c$ from **Equation 6.9**.

$$\bar{R}(\bar{t}_c) = 1 - \frac{1}{2}\bar{t}_c \tag{5.14}$$

Testing this solution against model simulations for different bubble radii **(Fig.5.8)**from shows it provides a very good fit for bubbles with a radius less than 10^{-6}m, matching the threshold at which the simplified solution for large bubbles **(Eq.6.14)** was no longer valid.

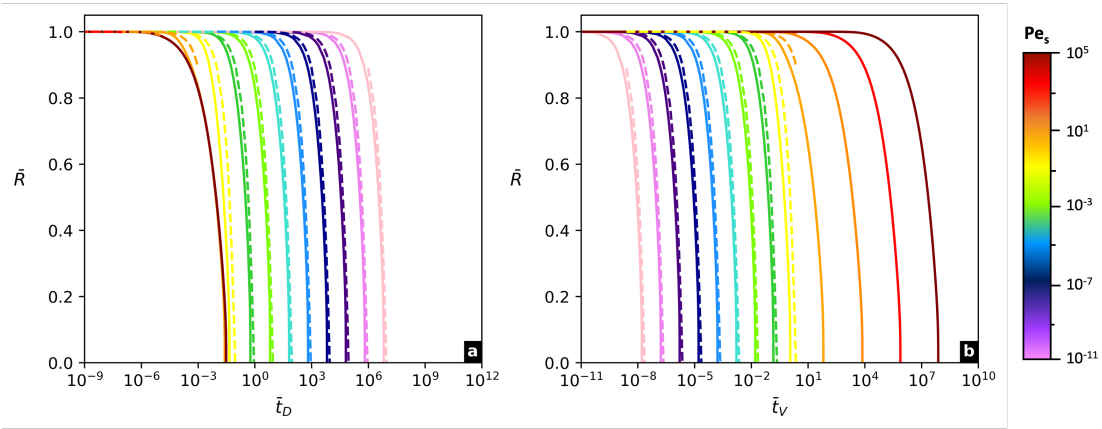

Figure 5.8: Combined model simulation results (solid lines) from **Figure 5.4** tested against the numerical solution (dashed lines) for smaller bubbles in the viscous limited where surface tension effects become dominant **(Eq.5.14)**. All curves are coloured according to the value of Pe_s for that system, shown by the colour bar. This solution gives a good fit to curves in both **(a)** diffusion-normalised, and **(b)** viscosity-normalised space for bubbles with an initial radius smaller than 10^{-6}m, suggesting this is the onset of the surface-tension regime. Bubbles larger than this would be better described by **Equation 5.9 or 5.12**

.

To summarise the numerical solutions for low-Pe_s, viscous limited systems, the complete numerical solution **(Eq.6.13)** provides the most comprehensive solution for a wide range of bubble sizes and system conditions as it accounts for both viscous and surface tension effects. For larger bubbles ($R > 10^{-6}$m) or more approximate results, the simplified solution **(Eq.6.14)** which neglects surface tension effects is appropriate. For smaller bubbles ($R < 10^{-6}$m), the simplified surface tension solution **(Eq.6.16)** gives a good estimation of bubble radius evolution.

5.5 Natural Systems Simulations

Having explored coupled bubble resorption and shrinkage for an idealised case using an analogue glass, the dynamics of water vapour bubbles in natural melt systems is considered, to see if the same observations are made and the same solutions for radii over time are applicable. The same model code can be used to do this but with one significant difference to the analogue system in that the pressure-temperature-concentration dependant laws for solubility, viscosity, and diffusivity, are reinstated instead of using fixed values. This means that model parameters such as viscosity adapt to the diffusing water during the time of the simulation. Initial water content of the melts was set to be very low in order to artificially ensure that each bubble tested would resorb.

Two endmembers of magmatic melt composition are tested, a basalt and a rhyolite, to see how the different properties of the melts affects bubble resorption. These properties are altered by changing the temperature at which the simulation is run. Completing similar analysis to **Section 5.3** will also reveal if bubbles in these melts sit in the diffusive regime, the viscous regime or across a spectrum between the two.

5.5.1 Rhyolitic Melt

To simulate a rhyolitic system, a rhyolitic obsidian from Hrafntinnuhryggur, Krafla (Iceland) **(Tuffen & Castro, 2009)** was selected to input into the *MATLAB* code. Solubility of this melt was modelled using the Liu et al. (2005) solubility model for H_2O in wt.%,

$$S = \frac{354.94p^{0.5} + 9.623p^{-1.5223}p^{1.5}}{T} + 0.0012439p^{1.5} \tag{5.15}$$

with pressure, p in MPa and temperature, T in Kelvin. For the diffusion of the H_2O from the bubble, the simplified diffusion model for rhyolitic silicate melts was used,

$$D = \mathrm{H_2O}_t \exp\left[-18.1 + 1.888p - \frac{(9699 + 3626p)}{T}\right] \tag{5.16}$$

where p is in GPa, T in K and $\mathrm{H_2O}_t$ is the wt.% of water **(Zhang & Ni 2010)**. Viscosity of the rhyolitic obsidian was calculated from the Giordano et al. (2008) model,

$$\mu = 10^{\left[A + \frac{B}{T-C})\right]} \tag{5.17}$$

in which A, B and C are constants unique to the melt composition; $A = -4.55$, $B = 11073$ and $C = 327.5935$. Incorporating these into the bubble growth code allowed bubbles of different sizes to be modelled in a hot melt (900°C) and a cooler melt (800°C).

Figure 5.9 shows the simulation results for the rhyolitic obsidian melt at 800°C. As with all simulations using the analogue glass, systems with different magnitudes of Pe_s have unique curves in non-dimensional space. In addition, the same collapses are seen at high-Pe_s for the diffusive limit and low-Pe_s for the viscous limit.

An observation that differs for this natural melt simulation is that for very small the curves

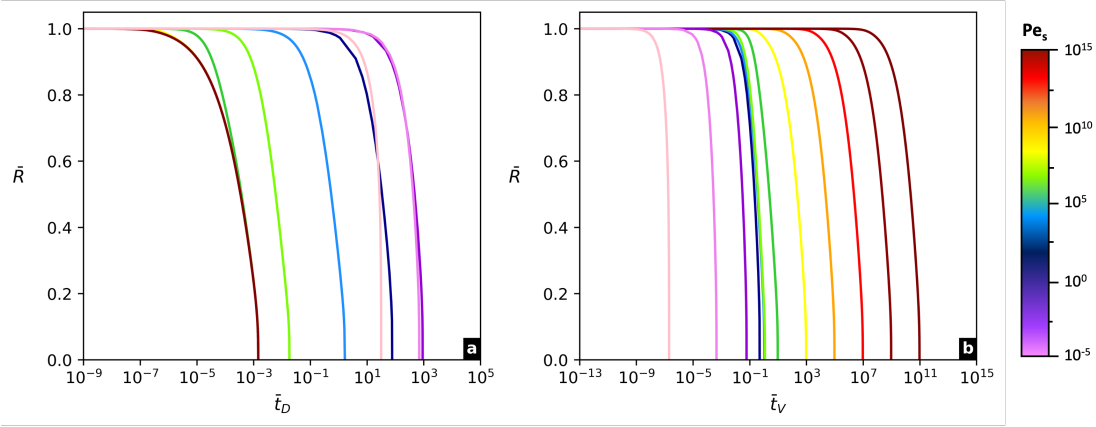

Figure 5.9: Simulation results for bubbles of different initial radii in rhyolitic obsidian melt from Krafla, Iceland at 800°C. All curves are coloured according to the value of Pe_s for that system, shown by the colour bar. The same trends in both **(a)** diffusion-normalised space, and **(b)** viscous-normalised space as those simulations for the analogue glass system can be seen, with higher Pe_s values on the left in **(a)**, but on the left in **(b)**. An additional observation is that curves for the smallest bubbles ($R < 10^6$m) do not follow this same trend and in **(b)** do not collapse to the viscous solution. This indicates the dominating effects of surface tension for these simulations which results in curves of a different shape. Similar simulations were also completed at a hotter temperature of 900°C more akin to an eruptive temperature, but outputs are not shown here.

in $\bar{R} - \bar{t}_D$ space have a different shape and no longer have the trend of increasing Pe_s to from left to right. Furthermore, in $\bar{R} - \bar{t}_v$ space the curves appear to deviate further to the left in $\bar{R} - \bar{t}_v$ space, away from the viscous limit. This occurs when bubble radius gets smaller than 10^{-6}m, suggesting there is a further limit – the perhaps the surface tension limit where surface tension effects become extremely significant in the bubble dynamics.

To better understand these limits and transitions, the same Pe_s transition analysis as **Section 5.3.3.3** is carried out, finding the value of $\bar{t}_D$ and $\bar{t}_v$ when each bubble has a radius half of its original size. Unlike with the simulated glass system there appear to be two transition phases **(Fig.5.10)**. The first, occurring around $Pe_s = 10^5$, is the transition between a diffusive or viscous limited regime. The second, occurring when $Pe_s << 100$, aligns with the deviations from the viscous limit observed in **Fig.5.9**.

This helps to confirm the presence of a second regime transition as bubbles get increasingly small (Pe_s increasingly small) and surface tension effect increasingly significant. It should be noted here that it is likely this secondary transition would also be observed in the silicate glass analogue melt if smaller radius bubbles were simulated. It is not likely to be something unique to natural melts.

Finally, the solutions for bubble radius evolutions in the viscous limited regime are tested against the rhyolitic obsidian simulation results.

The three different viscous solutions **(Eq.6.14, 15, 17)** are then tested **(Fig.5.11)** showing that the full numerical solution, accounting for both viscous and surface tension effects, gives the best fit to the resulting curves in the viscous limited regime (Fig.5.11a,b). The simplified solution for larger radius bubbles has a small window of good fit where bubbles are both large enough for surface tension effects to be negligible, but small enough for the system to

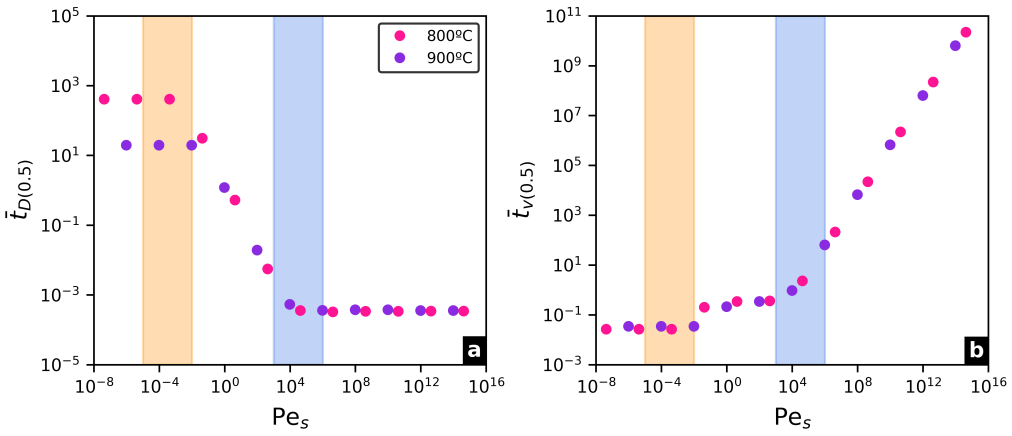

Figure 5.10: Analysis showing where the onset of the transition between the viscous and diffusive limits occurs for bubbles in the Krafla rhyolitic obsidian. Values of $\bar{t}_D$ and $\bar{t}_v$ are taken when bubble radius falls to 0.95% of the initial value. **(a)** $\bar{t}_{D(0.95)}$ against Pe$_s$ showing that at Pe$_s$ values $\geq 10^5$, $\bar{t}_{D(0.5)}$ has the same value for all simulations. These bubble systems sit in diffusion limited regime. For systems described by values of Pe$_s$ between 10^5 and 10^{-3}, $\bar{t}_{D(0.5)}$ increases with decreasing Pe$_s$, before becoming constant again for values of Pe$_s < 10^{-3}$. The first transition (blue shaded region) is that between the viscous and diffusion-limited regimes. The second (orange shaded region) is the transition between the viscous-limited and surface-tension limited regimes. The same two transitions are observed in **(b)** viscosity-normalised space at similar values of Pe$_s = 10^5$ and Pe$_s = 10^{-3}$.

still be in the viscous limited regime (Fig.5.11c,d). The most interesting observation here is that the simplified surface tension solution for small radius bubbles provides a poor fit for all simulated bubbles regardless of size **(Fig.5.11e,f)**. This suggests that for the natural melts, the complex interplay of surface tension effects and viscous effect that change as the gas species is diffusing cannot be captured by this simplified solution.

5.5.2 Basaltic Melt

To simulate a basaltic system, a melt composition of basalt from Kilauea, Hawaii was implemented into the *MATLAB* code. Alongside this, the laws for diffusivity, solubility and viscosity were also changed to be more appropriate for this type of system. The solubility model from **Iacono-Marziano et al. (2012)** for H_2O in a basalt,

$$S = \exp\left[0.54\ln(p) - 2.56 + 0.02\frac{p}{T}\right] \tag{5.18}$$

where p is in bars and T in K was used. The diffusion model was changed to be a temperature and water concentration-dependant model from **Zhang & Ni (2010)**.

$$D = \mathrm{H_2O}_t \exp\left[-8.56 - \frac{19110}{T}\right] \tag{5.19}$$

For the viscosity of the basaltic melt, a different law from Giordano and Dingwell (2003) Giordano et al. (2000) was implemented,

$$\mu = 10^{(-5.9-0.286\log|\mathrm{H_2O}|)} + \frac{10775.4 - 394.8\mathrm{H_2O}}{T - 148.7 + 21.65\log|\mathrm{H_2O}|} \tag{5.20}$$

with T in K and H_2O in wt.%. Changing the code to run from these laws allowed for water

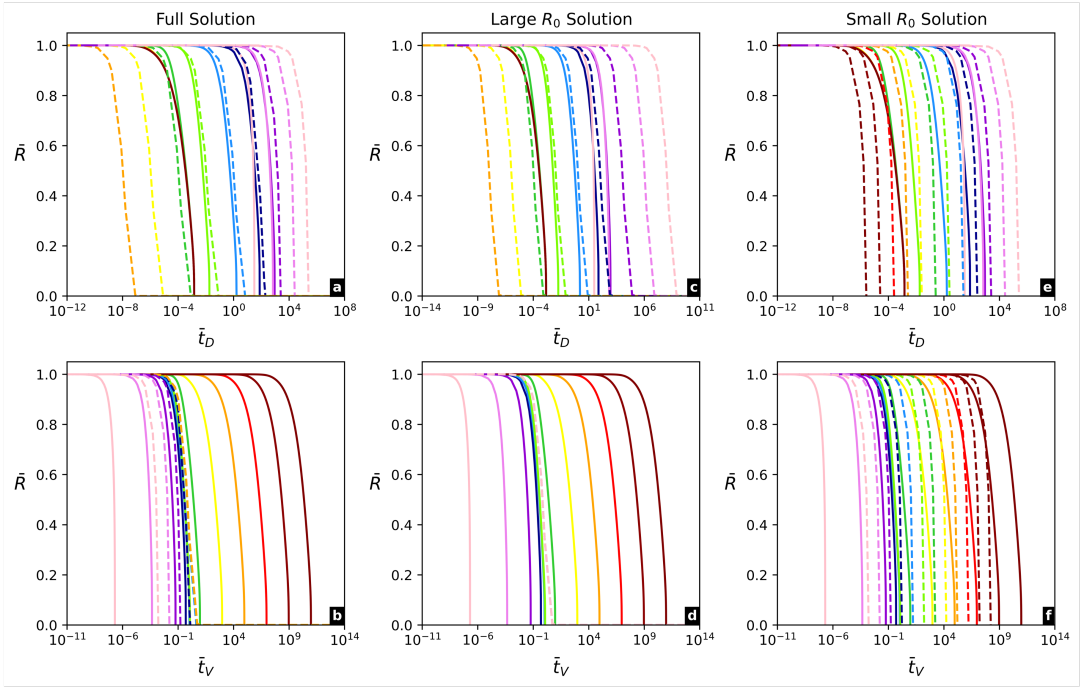

Figure 5.11: Model simulation results (solid lines) for bubbles in rhyolitic melt from **Figure 5.9** tested against the three different numerical solutions (dashed lines) for bubble systems in the viscous limited regime. All curves are coloured according to the value of Pe_s for that system, shown by the colour bar. **(a-b)** The complete numerical solution **(Eq.5.9)** has a good fit for bubbles in systems with a value of Pe_s between 10^5 and 10^{-5} (blue and light green curves) in both $\bar{t}_D$ and $\bar{t}_v$ space. **(c-d)** The numerical solution for larger radius bubbles **(Eq.5.12)** fits well for similar curves, which can be expected as these sit in the viscous-limited regime where surface-tension effects do not dominate. **(e-f)** The numerical solution for smaller bubbles **(Eq.5.14)** where surface-tension dominates doesn't provide a good fit to any of the simulated curves, even for the very smallest bubbles with radii $< 10^{-6}$m.

diffusion into a basaltic melt to be simulated at two different temperatures, 1050°C and 1150°C, characteristic of a hot and cooler eruptive temperature. The results from bubble simulations in the basalt at 1050°C are shown on **Figure 5.12**.

These display very similar trends to both the analogue and rhyolitic simulations with unique curves for different magnitudes of Pe_s. Similarly to the rhyolitic simulations, when initial bubble radius becomes very small (very low Pe_s) the curves begin to collapse together in $\bar{R} - \bar{t}_D$ space and spread out in $\bar{R} - \bar{t}_v$ space again, at a point different to the viscous and diffusive limits. This can again be attributed to significant surface tension effects and the onset of a surface tension limit.

Transition analysis finding the value of $\bar{t}_D$ and $\bar{t}_v$ when $\bar{R} = 0.5$ again confirms the presence of this second limit **(Fig.5.13)**. An observed difference between the basaltic simulations and rhyolitic simulations is that the transitions occur at higher values of Pe_s. The viscous-diffusive transition occurs around $\mathrm{Pe}_s = 10^7$, and the surface tension limit around $\mathrm{Pe}_s = 10^3$. These increased values are likely due to the physical properties of basaltic melts, such as lower viscosity and increased diffusivity. As a result, bubbles in basalts are most likely to sit within the diffusive regime at higher values of Pe_s unless the initial bubble radius is very small ($R < 10^5$).

The same solutions for bubble radius evolution are tested against the basaltic simulation

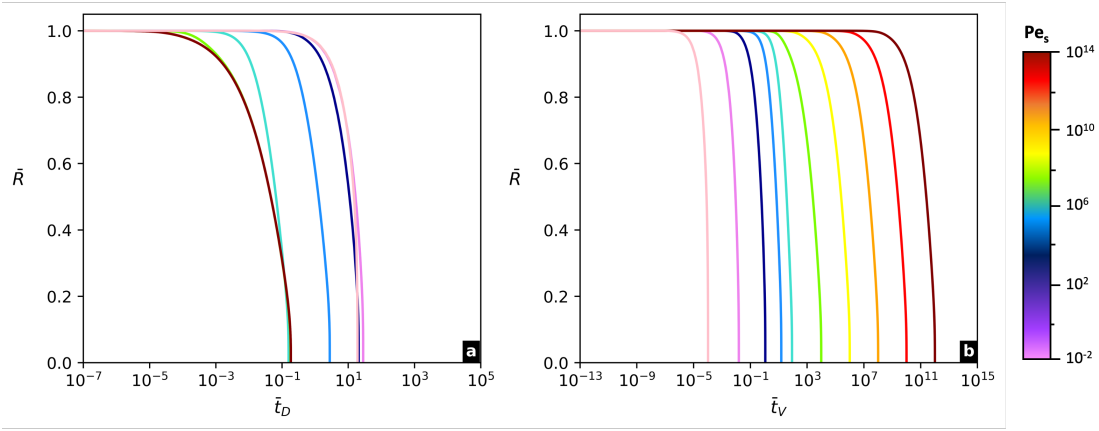

Figure 5.12: Simulation results for bubbles of different initial radii in basaltic melt from Kilauea, Hawaii at 1050°C. All curves are coloured according to the value of Pe_s for that system, shown by the colour bar. Similar trends in both **(a)** diffusion-normalised space, and **(b)** viscous-normalised space as those simulations for the rhyolitic system can be seen, with higher Pe_s values on the left in **(a)**, and on the left in **(b)**, but with deviations in curve shape and collapse for simulations of the smallest bubbles. This again indicates the dominating effects of surface tension when bubble radius is less than 10^6m. Figure **(a)** shows there is a much smaller window in which bubbles in basaltic melts sit in the viscous-limited regime, unaffected by either viscosity of the melt, or surface tension. Therefore, bubbles in these systems are likely to be better described by solutions for the diffusive limit. Similar simulations were also completed at a hotter temperature of 1150°C more akin to an eruptive temperature, but outputs are not shown here.

results for various different bubble radii at 1050°C. Comparisons of the simulations to the three viscous solutions **(Eq.6.14, 15, 17)** are shown on **Figure 5.14**. In all cases, the solutions do not give a very good fit to the radius evolutions in $\bar{R} - \bar{t}_D$ space but give a better description of the viscous limit in $\bar{R} - \bar{t}_v$ space.

It could be that basalts are more affected by changes to the melt system during the resorption of water, such as changes to viscosity, that mean a solution based on just the initial inputs of the system isn't appropriate. For the rhyolite, the melt properties remained much more similar to the initial inputs throughout, meaning this discrepancy between the solutions and simulations was less apparent.

Further exploration of the implications of these results for natural melt systems is discussed in **Chapter 7**. The impacts of the different likely regimes of basalts and rhyolites is also considered, in particular, the effect on magmatic processes and eruptive behaviours where bubbles play a key role.

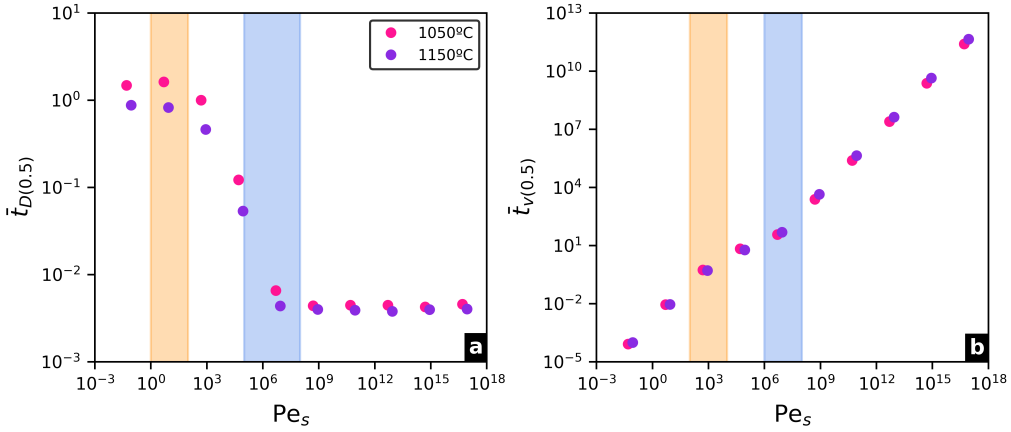

Figure 5.13: Analysis showing where the onset of the transition between the viscous and diffusive limits occurs for bubbles in the Kilauea basalt melt. Values of $\bar{t}_D$ and $\bar{t}_v$ are taken when bubble radius falls to 0.95% of the initial value. **(a)** $\bar{t}_{D(0.95)}$ against Pe$_s$ showing that at Pe$_s$ values $\geq 10^7$, $\bar{t}_{D(0.5)}$ has the same value for all simulations. These bubble systems sit in diffusion limited regime. For systems described by values of Pe$_s$ between 10^7 and 10^3, $\bar{t}_{D(0.5)}$ increases with decreasing Pe$_s$, before becoming constant again for values of Pe$_s < 10^3$. The first transition (blue shaded region) is that between the viscous and diffusion-limited regimes. The second (orange shaded region) is the transition between the viscous-limited and surface-tension limited regimes. The same two transitions are observed in **(b)** viscosity-normalised space at similar values of Pe$_s = 10^7$ and Pe$_s = 10^3$. The small range of systems that sit in the viscous limited regime again suggests that the majority of basaltic melt system will be diffusion-limited instead.

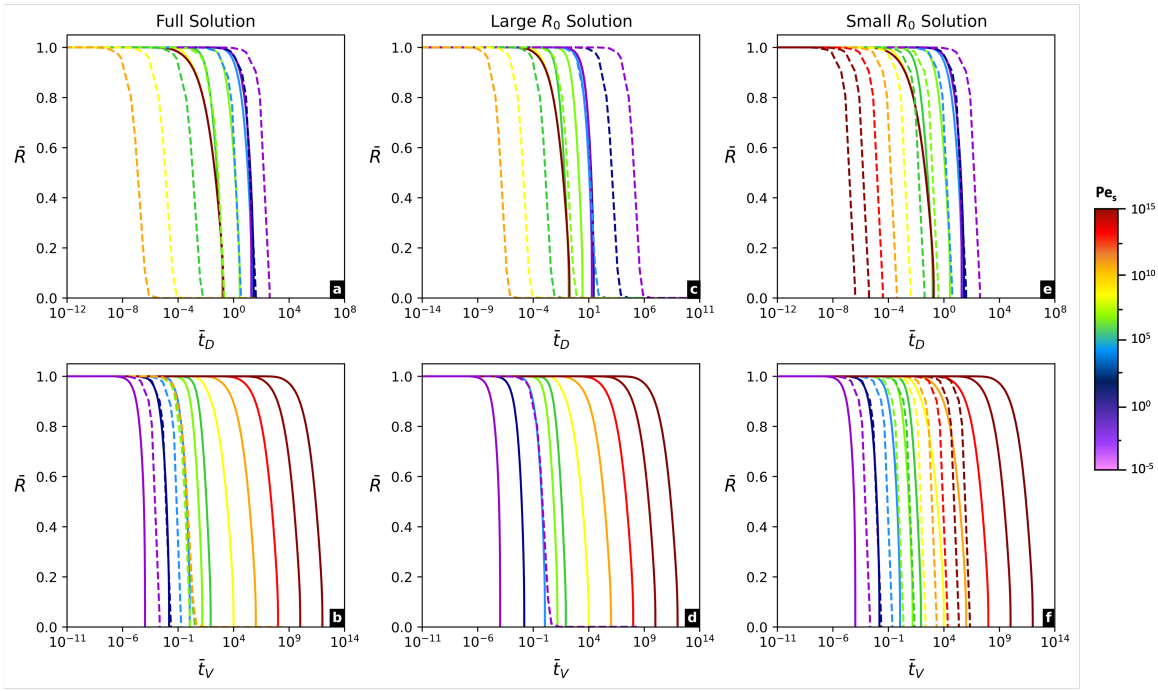

Figure 5.14: Model simulation results (solid lines) for bubbles in basaltic melt from **Figure 5.12** tested against the three different numerical solutions (dashed lines) for bubble systems in the viscous limited regime. All curves are coloured according to the value of Pe$_s$ for that system, shown by the colour bar. **(a-b)** The complete numerical solution **(Eq.5.9)** only has a good fit for one of the bubble simulations, in a system with a Pe$_s$ value of 10^4 (dark blue curve). This matches observations in **Figure 5.12 & 5.13** that suggest this system sits in the viscous-limited regime. For all other curves, the fit of this solution is very poor. **(c-d)** Fit of the numerical solution for larger radius bubbles **(Eq.5.12)** is similarly poor, only providing reasonable fit to the curve for Pe$_s = 10^4$ system. **(e-f)** The numerical solution for smaller bubbles **(Eq.5.14)** where surface-tension dominates again only provides a good fit to simulated curves for the Pe$_s = 10^4$ system. This means the bubble in this system is small enough to also be well described by the surface-tension limit solution.

Decoupled, Resorbing Bubble Systems

This chapter explores the final subset of bubble-melt system where both buoyant advection and significant mass transfer take place, resulting in a simultaneously rising and resorbing bubble. These systems will occur when neither the timescale of diffusion nor the timescale of advection is dominant. Instead, the two timescales have a more similar order of magnitude as the system conditions allow for both diffusive mass transfer of the gas and buoyant rise of the bubble through the melt with relative ease.

The decoupled nature of these systems means they are in the high Stokes number regime (Stk $>>$ 1) where the bubble moves freely of the melt. For describing this case, the advective timescale refers to the time for melt to move around the walls of a rising bubble. Therefore, λ_A is replaced with the buoyant rise timescale λ_b in the definition of Péclet number. As a result, these systems are described by the buoyant Péclet number Pe_b. Unlike the endmember scenarios discussed in **Chapter 4**, these decoupled-resorbing systems have a spectrum of Péclet number values extending from $\mathrm{Pe}_b \rightarrow \infty$ to $\mathrm{Pe}_b \rightarrow 0$ as λ_A and λ_D vary with the material properties of the gas and melt.

Observations of decoupled-resorbing bubbles in molten silicate melts have been made previously, with a focus on redox reactions between a bubble of oxygen and borosilicate glass melt. However, these systems are often subject to additional complexities that affect the dynamics of bubble resorption. In this chapter, new experimental results from a simplified scaled system using a golden syrup analogue melt are presented alongside the previous results from glass melts. Péclet number analysis similar to that in **Chapter 5** is completed on the combined datasets, including comparison to numerical solutions for decoupled bubble resorption.

Finally, results of bubble simulations in magmatic melts are shown as part of a discussion on bubble behaviours in natural silicate melt systems. Results in section **5.5** have shown that for natural magmatic melt systems, the buoyant Péclet number regime is only applicable to basaltic melts, and inappropriate for rhyolitic melts. The size of bubble required for a rhyolitic melt system to be better described by Pe_b would be so large that the system would no longer sit in the low Reynolds number regime, and therefore much of the underpinning theory applied in this work would no longer be correct. Consequently, simulations are completed solely in

melts of rhyolitic composition.

6.1 Observations in a Simplified Analogue System

To investigate the 'simplest' case for resorption of rising, decoupled bubbles, an experiment was designed using analogue materials. This 'simplest' case experimental system needed to provide observational evidence for bubble resorption as well as quantifiable results for the evolution of bubble radius over time but neglect any additional complicating factors to the bubble-melt system such as mixed gas bubbles or non-isothermal-isobaric conditions. Here, a description of the system, its design process and user procedure are outlined before initial results and observations are presented.

6.1.1 Selecting Materials

To select the analogue materials for the gas and melt phases, a scaling approach was adopted to ensure that (1) the viscosity and other material properties of the melt phase mean the system sat in the low Reynolds number regime and bubble rise timescales would be relatively long, and (2) the gas phase was sufficiently mobile in the melt that diffusion would take place on relatively short timescales. These two points were crucial to consider as it would make sure that the bubble-melt system didn't sit in either of the stationary or the non-diffusive rise regimes. Instead, it was preferable that a suite of experimental runs could be completed in systems that ranged in buoyant Péclet number by several orders of magnitude so that varying degrees of bubble resorption could be observed. This could be achieved by changing the analogue melt used, its temperature, or alternatively by generating different sized bubbles.

The practical constraints of a laboratory-scale experiment also had to be considered when selecting the materials for use. For a 'simple' case experiment, working at high temperature or pressures wasn't preferable as maintaining these at a constant value throughout a sample of melt may have been difficult and other factors such as convection or pressure-temperature gradients would have to be accounted for. Therefore, an analogue melt that could be worked with a room temperature and pressure was required. As set out in **Section 2.3.2.2**, golden syrup is an increasingly common small-scale analogue used for experiments investigating magmatic processes due to it being manipulable at standard laboratory conditions, inherently low risk and having naturally very viscous. This means it would provide sufficient resistance to a rising bubble to ensure the system remained in the low Reynolds number regime for bubbles up to ~ 15 cm in diameter. For these reasons, golden syrup was chosen as the analogue melt phase for the experimental system.

The gas phase chosen had to be able to diffuse into the golden syrup. Since this syrup diluted to around 80% with water, and the experiments were completed without changes to temperature or pressure, species such as water vapour were unsuitable. Other common laboratory gases such as oxygen or helium also presented practical difficulties due to high flammability or issues with sourcing small enough quantities.

Therefore, another common and readily available gas, CO_2, was considered. CO_2 is regularly

dissolved in many sugar syrup-based fluids such as fizzy drink syrups in soda streams among others *(Lv et al., 2018)*. Pre-experimental calculations **(Appendix III)** using the material properties of golden syrup and an estimate for the diffusion coefficient of golden syrup at room temperature showed that for a suitable range of experimental bubble sizes ($0.1 < R < 10$ mm), CO_2 would resorb on a timescale that would enable a range of Pe_b systems to be tested. Therefore, CO_2 was chosen as the gas phase for the experimental system.

A summary of the material properties required for both golden syrup and CO_2 for standard laboratory conditions of 298K and 1bar (10^5 Pa) pressure is given below in **Table 6.1**.

	Molar Mass $\mathbf{gmol^{-1}}$	**Density** $\mathbf{kgm^3}$	**Viscosity Pa.s**	**Diffusivity** $\mathbf{m^2s^{-1}}$	**Solubility wt.**%
Golden Syrup	198.17	1437.59	77.55	-	-
Carbon Dioxide	44.01	1.8393	-	1.6x10-9	0.03

Table 6.1: Material properties of golden syrup and carbon dioxide gas under experimental conditions used in pre-experimental calculations and all post-experimental analysis.

6.1.2 Methodology

The experimental equipment consisted of a gas delivery system that would take CO_2 from a small pressurised cannister via a flow regulator through a series of connecting silicon and copper tubes into an open cylinder of undiluted golden syrup. **Figure 6.1a** shows a schematic of the system used alongside images of the final setup **(Fig.6.1b-c)**. In addition to this, LED lighting and a camera were set up to take periodic photographs of each bubble as it moved through the syrup **(Fig.6.1d)**. Photo timings varied between runs (from 10 seconds to 5 minutes) to best suit the size of each bubble and its rise velocity, but the timestamp of each photo was recorded to ensure accurate analysis of bubble could be made subsequently.

6.1.2.1 Gas Delivery System

The gas delivery system modified the use of a gas recharger typically used for home-brew beer kegs. The ability to connect small volume pressurised CO_2 cannisters using this and the reasonable sensitive gas release trigger made this device suitable for the scale of these experiments along with the built-in safety-catch feature. Each gas cannister stored 16g ($21cm^3$ by volume) of 90-99% pure CO_2, pressurised to 900psi **(REF)**, equivalent to those used in commercial kitchen devices or domestic bike pumps. The recharger device connected these cannisters directly into a gas flow regulator which housed a further valve to vary the rate of gas flow between 0-0.5 litres-per-minute (LPM) **(Fig.6.1c)**. This valve controlled the release of gas into the feeder tubes and thus, controlled the size of the bubble injected into the syrup.

Connections throughout the whole of the gas delivery system, from the recharger to the regulator and subsequent tubes were all sealed with plumbing and PVC tape to ensure an airtight seal. Once secure, the delivery tubes were flushed with CO_2 from the pressurised cannister to remove air and reduce the likelihood of a mixed-gas bubble being produced. The copper tube end was then stopped with a small amount of syrup to keep the system flushed

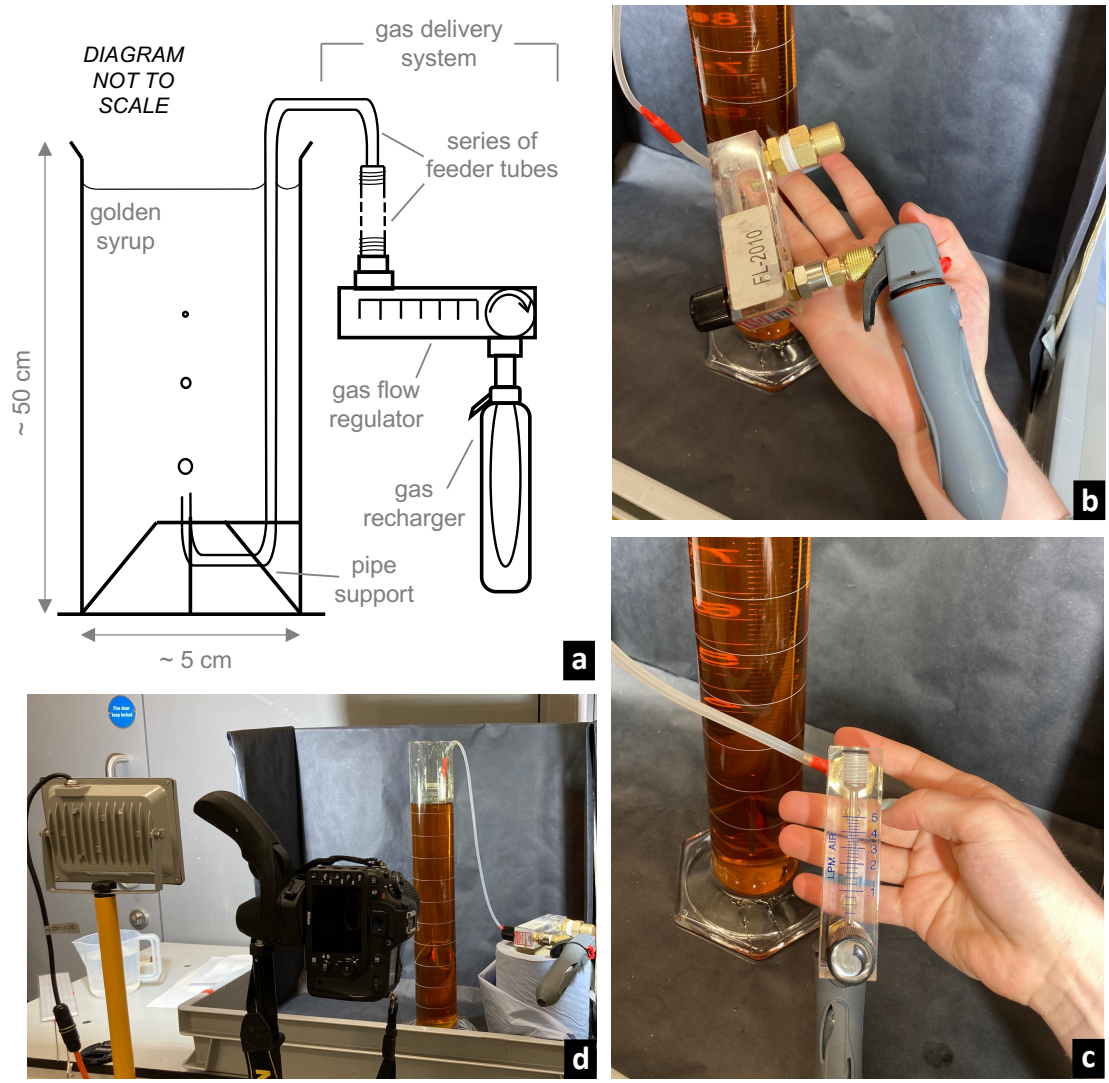

Figure 6.1: **(a)** Simplified schematic showing the experimental setup used. Not to scale, the components of the gas delivery system and the apparatus used to support the copper piping once submerged in the cylinder of golden syrup are shown. **(b,c)** Images showing the gas recharger and flow regulator for scale and in more detail. The safety catch on the recharger is visible in red and the gas release trigger in dark grey to the left of **(b)**. **(d)** Image of the wider experimental set up with the cylinder of syrup placed in front of a black screen to enhance the images taken by the camera. LED lights were adjusted onto the apparatus to provide better lighting for the images.

with CO_2, before the entire copper tubing section was submerged into a cylinder previously filled with bubble-free syrup **(Fig.6.1d)**. A small 3D-printed pipe support structure was also submerged to fix the final pipe position upwards in the centre of the cylinder cross-section.

6.1.2.2 Injecting Bubbles

Once the gas delivery system was submerged in the cylinder of syrup, the setup was left to settle for several minutes to allow any movement in the syrup to cease before a bubble was injected. By releasing the safety catch on the recharger and gently pressing the gas release trigger, CO_2 was released into the flow regulator. The control knob on the regulator was then briefly (∼1s) but carefully turned for allowing a small flow of CO_2 through the submerged pipe until a small bubble formed at the end of the final copper tube. Once free of the tube, the gas regulator value was turned to closed again and the safety catch on the recharger re-applied.

At this point, the camera was set to take periodic photos of the bubble until it had risen to the top of the syrup in the cylinder. For larger bubbles, photos were taken in closer succession than for smaller bubbles which could take significantly longer to rise the same distance. In total, ten differently sized spherical bubbles were injected in ten individual experiment runs. Between every 2-3 runs, syrup held in the cylinder was changed to ensure it wasn't becoming oversaturated, and the camera timings reset before the method was carried out again.

6.1.2.3 Measuring Bubble Radii

The set of photographs collected for each experiment were used to determine if the bubbles had undergone shrinkage from resorption. Observations of this by eye were extremely difficult to make out due to the very slow rise of the bubbles and the small scale of the experimental set up. Instead, the photos were used to quantify the bubble radii using scaling to grid. Prior to the submergence of the gas delivery system in each experiment run, a laminated tab of mm-scale graph paper was lowered into the syrup down the central plane of the cylinder cross-section and photographed. This photo formed a base scale over which photos of the bubbles were then laid. Taking measurements of both the grid and bubble diameter on image-editing software, then allowed for relative scaling to estimate each bubble size. Use of a grid photo taken 'in-situ' provided a continuous scale for measurement complete with correction for the effects of parallax and the curvature of the cylinder walls which proved better than trying to apply a digital grid to the bubble images subsequently.

Figure 6.2 shows how the gridded scale photos were used to measure bubble radii by superimposing them over images of the bubbles during rise. This method was completed for images from various stages of each bubble experiment, using the appropriate scale image for that run, to help build an understanding of radius evolutions.

6.1.2.4 Methodology Development & Limitations

The final experimental system and methodology were the result of a series of trial-and-error tests using different gas flow regulators, tubing configurations and connectors. Some of the initial connections used were not completely air-tight meaning CO_2 gas was escaping unnecessarily and raised the concern that air might be getting into the system to form mixed gas bubbles.

The type of flow regulator had to be changed from the original planned design to allow for much more precise control of gas delivery. This high level of control was required to inject bubbles into the syrup that were small enough to have a significant residence time in the syrup and not just rise rapidly with limited time for diffusion.

Another issue encountered was that once a bubble had been released into the syrup, there would be some 'back-flow' of syrup into the copper tubing. This again likely occurred due to the system not being perfectly airtight. As a result, the tube regularly became blocked to the point where the pressure of gas released into the tube was insufficient to force out the syrup and form a bubble. To fix this, the entire section of submerged tubing had to be regularly removed from the syrup, dismantled, cleaned and reconnected before it could be re-submerged to inject a bubble again. This was a timely process that markedly increased the lab time for

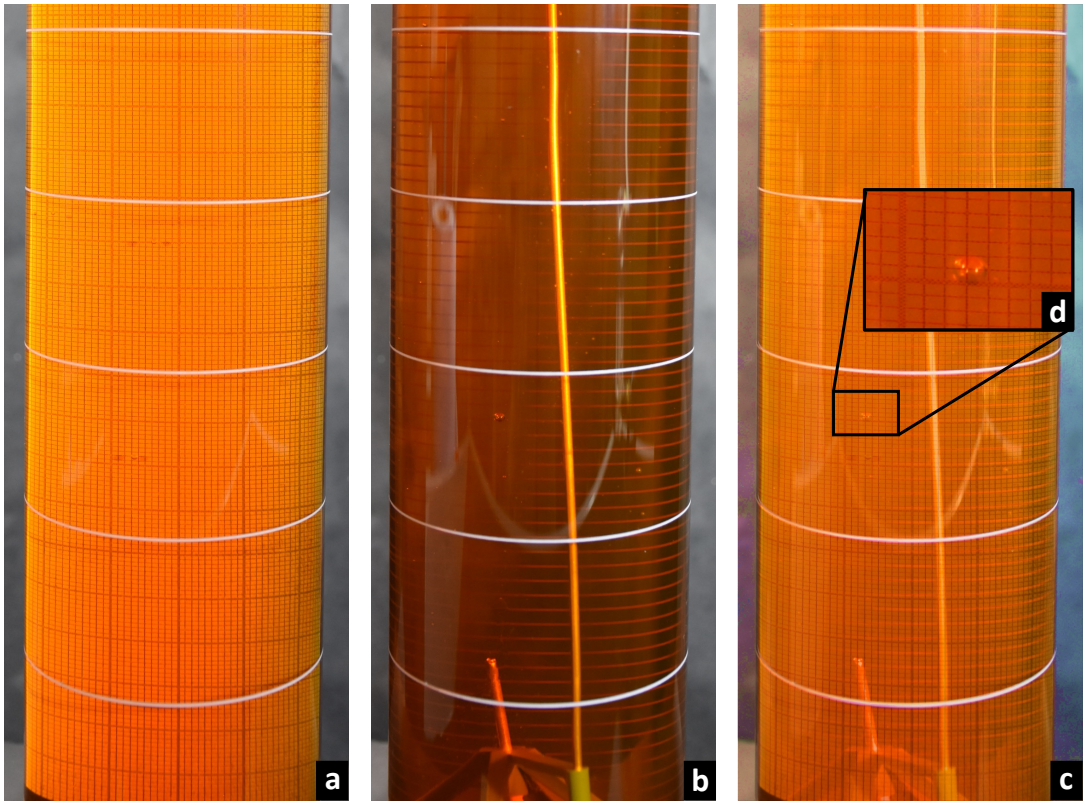

Figure 6.2: A selection of images showing how bubble radii were measured using photos of a gridded scale. **(a)** Image of the millimetre gridded scale submerged down the central axis of the cylinder of golden syrup. The horizontal white lines are markers on the outside of the cylinder and provided a good reference point when matching up the images. **(b)** Timelapse image (file DSC_7399) from bubble run 6 where the initial bubble radius was 1.15 ±0.12 mm. **(c)** Overlain images of the gridded scale and bubble. Without image alteration and cropping, it is difficult to interpret the bubble size. **(d)** Cropped image with alteration to colour and contrast to make both the bubble and scale clearer for measurement.

each experiment run and limited the number of runs that could be run in any one session.

The method used to measure bubble radii was also developed through trials. Originally, use of a scale on the outside of the cylinder was the proposed method of measuring bubble radii, however it soon became apparent that this had a large associated uncertainty due to distortion from both the syrup itself and the curvature of the cylinder containing it. Therefore, the submerged scale positioned to where the bubbles were then injected proved a much better method.

Use of digital image alteration tools allowed the colour, contrast and transparency of the collected images to be adapted so that the bubble edge and gridded scale were both as clear as possible during measurement. In some cases, reflections or marks on the glass meant a measurement of bubble radius wasn't possible meaning some images had to be disregarded. There was also still fairly significant uncertainty in the measurements of bubble radii due to the small scale of the experimental setup and measuring approach used. Nonetheless, bubble radii could still be measured repeatedly with reasonable accuracy for the required analysis using this technique.

Despite the limitations, mainly due to the practice required to control the gas input to

create small bubbles and the required regular clearing of the tubing, the final experimental set up did allow reproducible runs to be completed with bubbles of different sizes injected and monitored during rise through the cylinder of syrup. The digital measurement method still had quite large uncertainties associated with it but provided the most accurate way of simply measuring bubble radii through time to a reasonable degree of precision.

6.1.3 Results

Measurements made from digital photograph analysis yielded ten independent datasets for bubble rise distances and radii over time. This data is presented in full in **Appendix III**. From these datasets, several different lines of analysis can be completed including estimation of bubble terminal rise velocities (TRVs), an estimation of CO_2 solubility in golden syrup and analysis of bubble shrinkage due to resorption.

6.1.3.1 Bubble Terminal Rise Velocities

Bubble TRVs can be estimated from the total rise distance travelled during the experiment run. Given the high-viscosity of the golden syrup, it is expected that TRVs should be reasonably well described by the Hadamard-Rybczynski solution **(Eq.2.15)**, varying with initial bubble radius. **Figure 6.3** shows the experimentally observed TRVs as a function of initial bubble radius alongside the H-R estimation for a CO_2-golden syrup system.

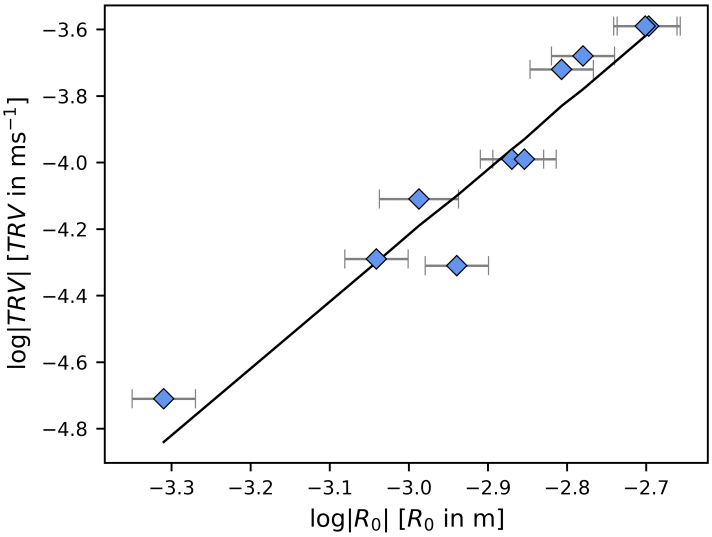

Figure 6.3: Terminal rise velocities (TRVs) of CO_2 bubbles in golden syrup against the initial raidus, R_0. TRVs are calculated from the total rise height and rise time. The data points show a good fit to the Hadamard-Rybczynski solution for bubble rise in high-visocsity fluids (black line) **(Eq.2.15)**. This assumes there is no effect on TRV from the reducing bubble size as a result of resorption, which could explain why some of the data lie outside of error with this solution. An integral approach to modelling bubble rise velocities *(Jackson et al., 2022)* may be more appropriate for this setting in the future.

An assumption made in the calculation of these TRVs is that any reduction in bubble size due to resorption is small enough that on the scale of these experiments, it would not significantly affect the rise speed. However, in reality as a bubble shrinks it will have less buoyancy and

therefore rise with a slower velocity through the melt. This simplification could help explain some of the deviations from the H-R solution in **Figure 6.3**, and if bubble were monitored through to complete resorption, these deviations could be even more profound. Nevertheless, the TRV average across the total rise distance for each bubble is still reasonably well described by this solution.

6.1.3.2 Estimating CO_2 Solubility

Prior to experimentation, the solubility of CO_2 in golden syrup had been estimated from that for water given that 20% of golden syrup by volume is water **(see Appendix IV)**. Using the data collected and some assumptions, a more direct estimate of CO_2 solubility can be made and compared to the previously assumed value.

To do this, each bubble is considered to have risen through a cylindrical volume of melt with a cross-sectional radius equal to that of the initial bubble, and a height equal to the total bubble rise distance. This gives a volume of melt that the bubble would have been in direct contact with as it rose. The volume of CO_2 lost from each spherical bubble is estimated from the initial and final bubble radii. From there, the moles and mass of both the syrup and gas are calculated and compared to give a value for solubility in weight percent.

Completing this for each of the ten bubbles observed gives a range of estimates for S_{CO_2} all of which sit around two orders of magnitude lower than those of the original estimated value from water. The mean S_{CO_2} from the ten measurements is 4x10-4 wt.% compared with $3x10^{-2}$ used in experimental planning calculations **(Fig.6.4)**.

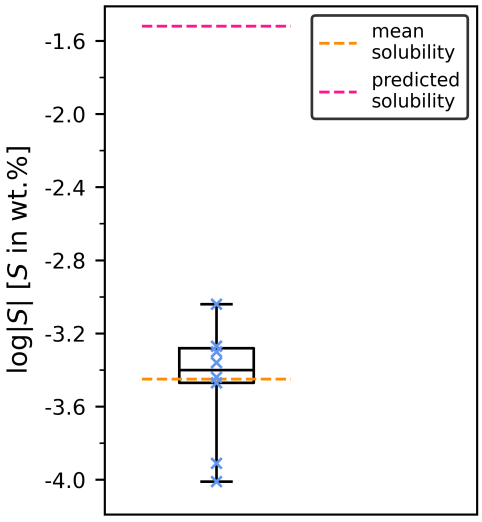

Figure 6.4: Estimates of CO_2 solubility in golden syrup from the ten observed bubbles. To generate each data point (blue crosses) the volume reduction of the resorbing bubble and volume of melt encountered during rise are used to calculate S_CO_2 in wt.%. Both the mean and median solubility values found using this method are around two orders of magnitude lower than those predicted from the solubility of CO_2 in the pre-experimental calculations.

This discrepancy could be explained by golden syrup being a mixture of sucrose and invert sugars which contain carbon within their molecular structure, meaning the ability for the syrup to accommodate more carbon from CO_2 is lower than that for pure water, which previously

contains no carbon. As a result, it could be expected that the solubility of CO_2 in golden syrup is lower than that in water. However, due to this S_{CO_2} measurement being estimated from a small number of experimental values via a method using several different assumptions, the original value of $3x10^{-2}$ used in experimental planning calculations continues to be used in all further analysis.

6.1.3.3 Bubble Shrinkage

Measurements of bubble radius with time were collected for each of the ten experimental runs using the digital analysis method. **Figure 6.5** shows radius evolutions for each bubble complete with the estimated measurement uncertainty. In **Figure 6.5b** the data been normalised to each initial bubble radius to allow for better comparison.

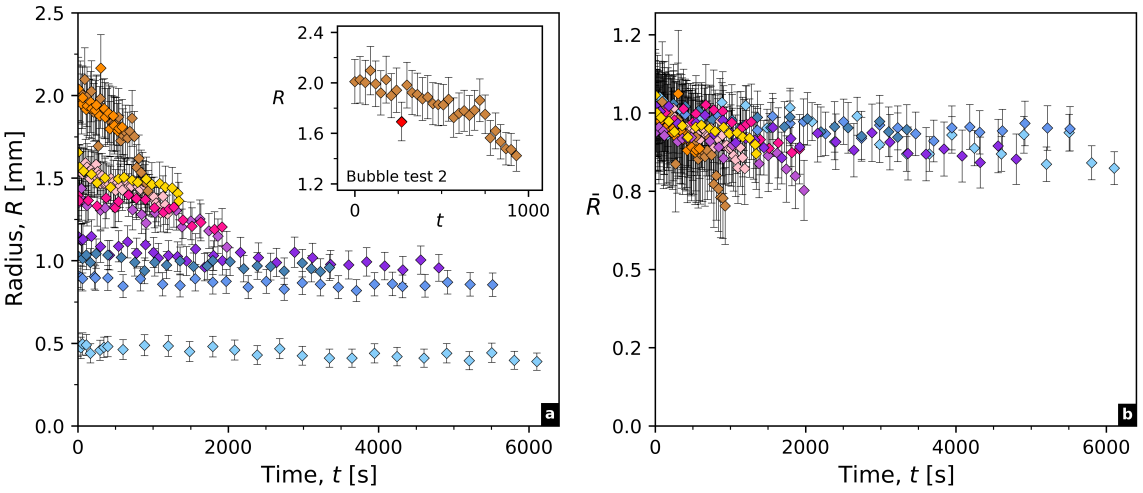

Figure 6.5: Datasets collected from ten experimental runs of CO_2 bubbles in golden syrup. Data point colours do not correspond to any other value, just each different dataset. **(a)** Bubble radii over time suggest there is some bubble shrinkage occuring. For the smallest bubbles, this reduction is less definite as over change in the radius does not fall outside of error. However for larger bubbles, reduction in bubble size is more apparent. the small subplot shows an individual dataset for *Bubble Test 2* to demonstrate that radius change is greater than the estimated errors. On this plot, the datapoint marked in red is considered erroneous as lighting in the image used to make the measurement made it difficult to read. **(b)** Bubble radii normalised to the initial radius of each bubble test to enable for better comparison between bubble sizes. This suggests that the initially larger bubbles (eg. orange datapoints) shrink at a faster rate than initially smaller bubbles (eg. blue or purple datapoints).

All bubbles appear to have undergone a small degree of shrinkage, however, there is significant uncertainty in the data which casts a high level of inclarity to some of the results, especially for the smallest bubbles. However, for the larger bubbles, reductions in bubble radii fall outside of the margin of error suggesting that shrinkage is taking place **(Fig.6.5a)**. It could be that if the cylinder of syrup had been taller, the bubbles would have had a greater rise distance and longer residence time in the syrup over which to resorb meaning the observed shrinkage would have been more definite.

A second observation from this initial data is that larger bubbles appear to be resorbing at a faster rate than smaller bubbles. This mimics observations from previous decoupled resorbing bubble studies such as Pereira et al. (2020) where the rate of resorption for bubbles rising under the same conditions appears dependant on the initial bubble size **(see Section 6.2)**.

6.1.3.4 Bubble Shrinkage Rate

To better analyse if bubble shrinkage rates are dependent on bubble size, radius change over approximately the first 10 minutes each experiment (dR/dt) is plotted against initial bubble radius **(Fig.6.6a)**.

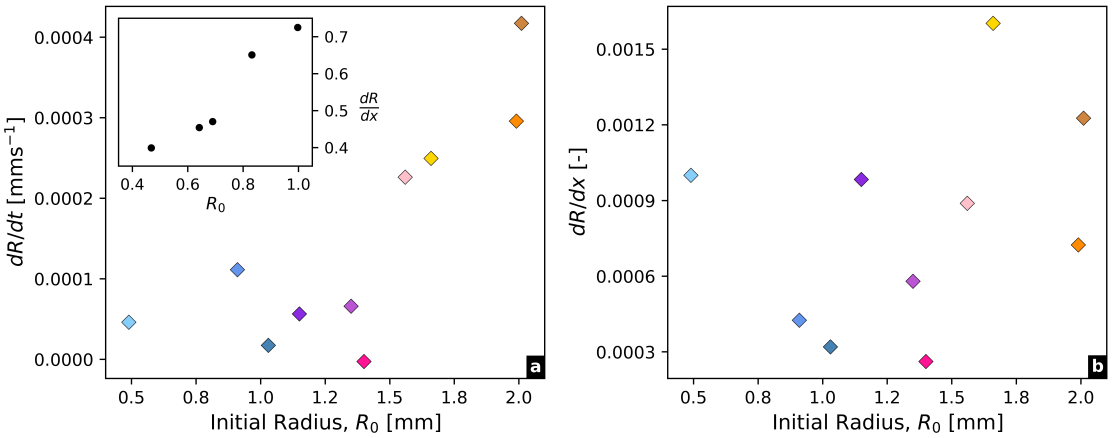

Figure 6.6: Different rates of bubble shrinkage for the CO_2 bubbles in golden syrup. Data point colours do not correspond to any other value, just each different dataset as in **Figure 6.5**. **(a)** Change in bubble radius with time, dR/dt plotted against the value of the initial bubble radius for each of the ten bubbles observed. dR/dt is measured across the first ten minutes of each bubble test. Data suggests there is a positive trend, with initially larger bubbles having a faster shrinkage rate with respect to time. The small subplot shows data from Pereira et al. (2020) where the same trend was observed. **(b)** Change in bubble radius over the first 100mm of bubble rise plotted against the value of the initial bubble radius for all ten bubbles observed. In this instance the trend between the two datasets is less apparent, suggesting that over the same distance, bubbles resorb at a similar rate, independent of bubble size.

This appears to show a positive correlation between dR/dt and R_0 similar to that from Pereira et al. (2020), shown in the subplot of **Figure 6.6a**. It might be expected for systems with larger bubbles, yielding higher Péclet number values would undergo very little diffusive resorption as high values of Pe_b indicate that the characteristic advective timescale is much shorter than the diffusive timescale, and thus rise would be more rapid than resorption. However, these results appear to contradict this, with initially larger bubbles resorbing faster than smaller bubbles. In their work, Pereira et al. attribute this trend to larger bubbles having greater TRVs which results in the chemical boundary layer around the bubble wall being decreased, enabling faster diffusion. However, it is also plausible that the faster TRV of these larger bubbles means they encounter more, 'new' melt over the same timescale than small bubbles would. As a result, they are continually rising into melt with a larger concentration gradient than they were previously in. As a result, gas from the bubble will diffuse at a greater speed for longer, resulting in more rapid resorption. This is discussed further in **Chapter 7**.

Fig.6.6b, which shows bubble shrinkage rate over the first 100 mm of bubble rise (dR/dx) helps to support this hypothesis, as over the same travel distance the degree of resorption is similar for bubbles of all sizes, with little apparent dependency on initial bubble size. Therefore, it is due to the faster rate of movement through the melt resulting from the faster TRV that larger bubbles are able to resorb more in a given time.

6.1.3.5 Summary of Results

To summarise the experimental data collected for the analogue system of CO_2 bubbles in golden syrup at room temperature and pressure; the rise velocity of all bubbles is well described by the H-R solution for spherical bubbles in high-viscosity, low Re systems. An estimation of CO_2 solubility as $1x10^{-3.5}$ calculated from the initial and final bubble volumes is within the same order to that estimated from water and confirms that CO_2 is soluble in this system.

Measurements of bubble radii over time suggest resorption is taking place and that larger bubbles resorb at a faster rate than smaller bubbles, but results are subject to significant uncertainties due to the small scale of the experiments. Use of a larger cylinder of syrup could help reduce these uncertainties and would provide a larger rise distance and longer residence time in the syrup so that more complete bubble resorption might be observable.

It is also possible that there is some contamination of the gas within the bubble resulting from the air remaining within the tubes of the gas delivery system. As a result, the bubbles may have a mixed gas composition meaning there is a limit on resorption if one of the gases in the mixture (such as air) is not soluble in the syrup or diffuses very slowly.

Despite some of these uncertainties and limitations, the suite of experimental data gives an insight into a simple analogue system for simultaneous bubble rise and resorption. This data is combined with a collection of existing data for further analysis in **Section 6.3**.

6.2 Observations in Glass Melt Systems

A series of previous, more complex studies made observations of decoupled bubble resorption in silicate melts and molten glasses. Added complexities included the conduction of experiments at high temperatures, and the use of mixed gas bubbles prompting other factors to be considered, such as limits to complete resorption or chemical reactions between the different gases and melt. Two studies are focused on here: Pigeonneau et al. (2010); Pereira et al. (2020), both completed from the perspective of industrial glass refinement or 'fining', the process by which bubbles, or gaseous impurities are removed from molten glasses. This process is vital in the industry of glass manufacturing and other industrial glass-based processes such as nuclear waste conditioning. Nonetheless, the results presented support theory which has much wider applications including the scope of this work.

Pigeonneau produced a series of works *(Pigeonneau, 2009, 2011; Pigeonneau et al., 2010)* investigating the resorption of oxygen bubbles in molten glass. They focussed principally on the problem of decoupled bubbles but also extended to consider reduction-oxidation (redox) reactions of the oxygen with iron compounds in the glass taking place simultaneously to diffusion and bubble rise. Alongside experimental results observed at high temperatures, Pigeonneau developed an increasingly complex numerical solution to describe bubble radius evolutions with time in a high-visocsity, redox environment. This model is discussed further in **Section 6.4**.

Observations of decoupled resorbing bubbles in a glass melt are presented in Pigeonneau et al. (2010). These observations and measurements of bubble radii over time were made

using a novel transparent furnace *(Kloužek and Němec; Fig.1 in Pigeonneau et al. (2010))* and gas delivery system which allowed millimetre-scale bubbles of oxygen to be injected into two different compositions of molten soda-lime-silica glass. Bubbles were monitored directly for several hours through the furnace window and recorded using a video camera to acquire measurements of radii.

In total, four different bubbles were injected and observed, two in each of the glass compositions and each one at a different temperature. Collective results for radius evolutions over time are shown on **Figure 6.7**, including data normalised to the initial bubble radii for better comparison **(Fig.6.7b)**.

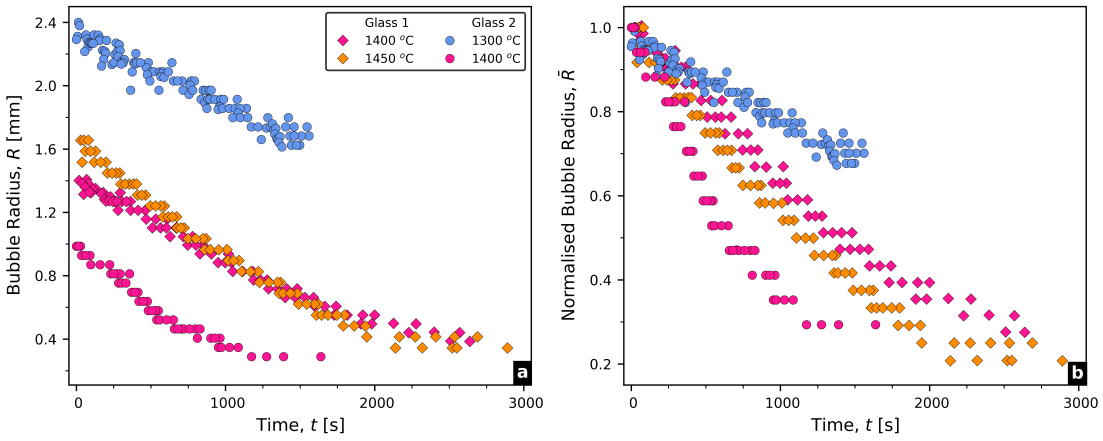

Figure 6.7: Datasets collected from Pigeonneau et al. (2010) for the evolution of oxygen bubble radii in two different soda-lime-silicate glasses (Glass 1 & Glass 2). **(a)** Radius evolutions with respect to time show that all bubbles are undergoing resorption but towards a plateau rather then complete resorption. This suggests there may be another non-resorbing gas species present in the bubble. **(b)** Bubble radii normalised to the initial bubble radius for each experiment against time, enabling better comparison. Bubbles in hotter melts appear to resorb faster and bubbles in Glass 2 resorb faster than those in Glass 1 at the same temperature.

These results show that bubbles resorbed faster in higher temperature melts, and in Glass 1 which had a lower iron content. This confirms the hypothesis of Pigeonneau et al. that an increased iron content reduces the shrinkage rate of an oxygen bubbles due to the mass transfer of oxygen controlling the redox of iron; a conclusion significant glass refinement processes where reagents need to be selected to enhance the removal of bubbles.

A second observation is that the bubble radii appear to plateau towards a non-zero value described by Pigeonneau as reaching steady-state. Similar to observations from the results of bubbles in golden syrup in this study, this is attributed to the presence of other gases in the bubbles, which therefore cannot be assumed to be pure oxygen. Complete resorption of the bubble is not then observed as either the glass melt is completely saturated in these contaminating gas species, or the gas has a diffusion rate much slower than the timescale of the experiment. Pigeonneau considers the behaviour of mixed gas bubbles more in a later numerical study *(Pigeonneau, 2011)*, including the possibility for one gas species to diffuse into a bubble whilst another is diffusing out which would also act to limit complete bubble resorption.

In a more recent work by Pereira et al. (2020) the work of Pigeonneau et al. (2010) is built

upon but instead with observations of decoupled resorbing oxygen bubbles in borosilicate glasses. Still focussed on the effects of redox reactions, the glass melts were doped with differing amounts of a cerium agent to alter redox state and thus the rate of bubble resorption. A similar experimental set up and digital measuring technique to that of Pigeonneau et al. (2010) was used but for a much more extensive range of bubble sizes and glass types. In total, 45 bubbles were injected, and radii monitored over time. **Figure 6.8** shows a sample of the collected data to demonstrate some of the key observations.

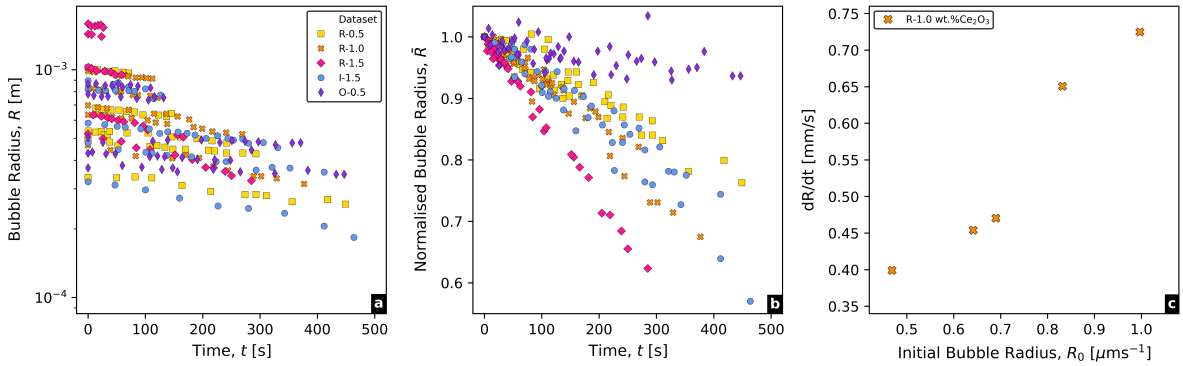

Figure 6.8: Datasets collected from Pereira et al. (2020) for the evolution of oxygen bubble radii in borosilicate glass melts with differing quantities of Ce_2O_3. Five datasets are selected to show the range of behaviours observed, the names of which correspond to those listed in their work. The number in each dataset name refers to the wt.% of Ce_2O_3 doping agent added to the melt. **(a)** Bubble radii over time shows that bubbles in all the different glass compositions are undergoing resorption **(b)** Bubble radii normalised to the initial bubble radius of each experiment against time shows that bubbles in melts with a greater Ce_2O_3 content (increased reduction state) resorb faster than those in melt with a lower Ce_2O_3 content. **(c)** Rate of bubble resorption with respect to time, dR/dt against initial bubble radius for a single dataset repeated from the subplot of **Figure 6.6**. Larger bubble appear to resorb faster than smaller bubbles.

Across all bubble sizes and melt compositions, the experimental observations support the case that an increased reduction state of the melt enhances bubble resorption due to it increasing the rate of mass transfer of oxygen. As mentioned previously and observed in the golden-syrup experiments of this study, a second observation made is that under the same conditions, initially larger bubbles appear to shrink faster when monitored over the first ten minutes of rise, than initially smaller bubbles **(Fig.6.8c)**. Pereira et al. attribute this to larger bubbles having a greater terminal rise velocity than smaller bubbles, which they suggest would cause a reduction in the chemical boundary layer around these bubbles. This reduced layer would then enhance the mass transfer of the oxygen leading to more rapid resorption of initially larger bubbles. Numerically, they explain this as an increase in Péclet number which in turn would increase Sherwood number, the dimensionless value used to describe the relative rate of bubble shrinkage in their study. Importantly to this study, this observation matches those made for bubbles of CO_2 in golden-syrup, showing that it appears to be the case across multiple different gas-melt systems.

To summarise the key observations from these two more complex studies using glass melts, the rate of bubble resorption appears to depend on (1) temperature, a higher temperature melt will resorb a bubble at a faster rate; (2) redox state, with more reduced melts resorbing bubbles faster and (3) initial bubble radius, as initially larger bubbles appear to resorb faster.

Perhaps the most significant to this work are the effects of temperature and initial bubble radius as the effects of redox or further chemical reactions fall outside of the scope of this work. Importantly, observations from these past studies align with those newly presented for a different gas-melt system in **Section 6.1.3**.

6.3 Analysis of Combined Experimental Results

Results from this work can now be combined with those from the two existing studies to create a combined dataset with decoupled bubbles of different gases in various silicate and non-silicate analogue melts. This larger dataset enables further analysis and discussion using Péclet numbers to explore possible trends between the different systems and the implications of any findings to the field of volcanology.

6.3.1 Buoyant Péclet Number Analysis

To start with, the value of buoyant Péclet number is calculated for each individual dataset using **Equation 2.18** before the data is combined graphically **(Fig.6.9)** and coloured according to this value of Pe_b. **Figure 6.9a** shows only the new data from this study of CO_2 bubbles in golden syrup. **Figure 6.9b** shows this dataset combined with the two existing datasets from Pigeonneau et al. (2010) and Pereira et al. (2020) recoloured to accommodate the wider range in Pe_b values.

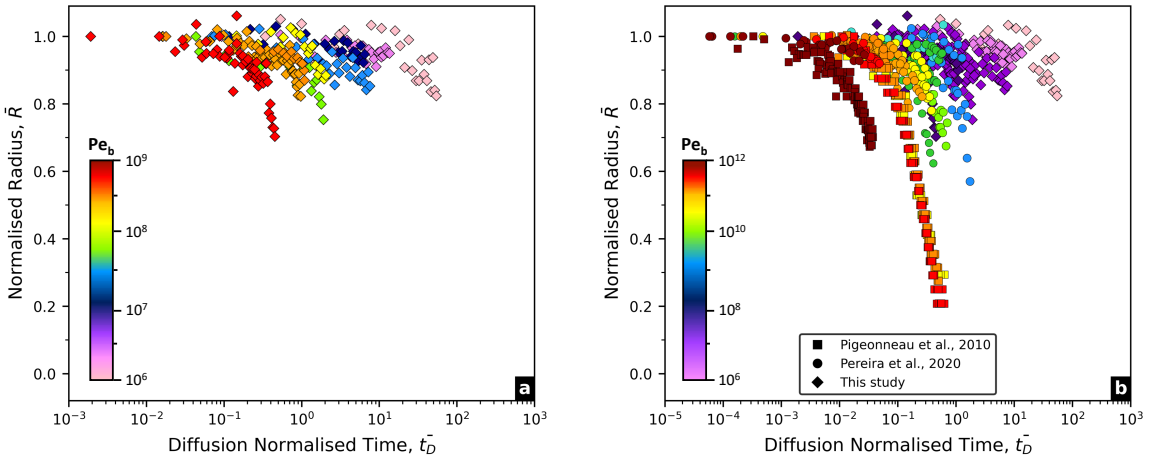

Figure 6.9: **(a)** Datasets from observations of CO_2 bubble resorption in golden syrup normalised to initial bubble radii and the diffusive timescale. Each dataset is coloured according to the value of Pe_b for that system shown by the colour bar. Higher Pe_b systems sit to the left of the plot and those with lower Pe_b values, to the right, in a similar to trend to that observed for stationary bubbles **(eg. Fig.5.4)**. **(b)** Combined datasets from this study, Pigeonneau et al. (2010) and Pereira et al. (2020) normalised to initial bubble radii and and the diffusive timescale. Each dataset is again coloured according to the value of Pe_b for that system shown by the colour bar. Across this wider set of data, the same trend is apparent with data aligning according to the value of Pe_b, descending from left to right.

A trend immediately observed across both figures is that the data organises according to Pe_b value. Whilst the data doesn't collapse to exact or complete curves, likely due to natural variation that arises with experimental results, the data groups together by Pe_b value, increasing from right to left. This observation is similar to that made in $\bar{R} - \bar{t}_D$ space for simulations of

stationary bubble resorption in **Chapter 5**.

On **Fig.6.9b**, datasets from the two studies using glass melts have higher Pe_b values and sit to the left of those from this study in golden syrup. These elevated Pe_b values are likely to result from the glass melts having a much higher density than golden syrup, or oxygen having a relatively low solubility and diffusivity with both glasses, all of which would act to increase the value of Pe_b **(Eq.2.18)**.

All of the datasets displayed on **Figure 6.9** are described by Pe_b values much greater than 1, the previously hypothesised threshold for the transition between a diffusive or advective controlled regime. Even if the higher transition point of 10^5 observed throughout **Chapter 5** is considered, the datasets still all sit in the high Pe_b, diffusion limited regime. It would then be expected that in $\bar{R} - \bar{t}_D$ space, the high Pe_b datasets would collapse to a single solution for this diffusive limit. However, **Figure 6.9** shows there is no such collapse, indicating that even at very high values of Pe_b ($> 10^{10}$), viscosity is still playing a role in the dynamics of bubble resorption. This results in a transition window for Pe_b that is not the same as that for Pe_s and therefore very high Pe_b systems can still be defined by unique bubble radius evolutions.

6.3.1.1 Pe_b Regime Transitions

To confirm that the datasets collected with very high Pe_b values don't yet sit in the diffusive limited regime, transition analysis is completed **(Fig.6.10)**. In variation to that completed in **Chapter 5**, the value of t_D taken each time is that when $\bar{R} = 0.95$ as many of the observed bubbles did not shrink to half their initial radius. Due to the values being taken from experimental data, exact values of $\bar{t}_D$ when $\bar{R}$ =0.95 are not always possible to extract, and instead the next nearest $\bar{t}_D$ value is used.

A negative correlation is observed between $\bar{t}_{D0.95}$ and Pe_b for all data points, with no horizontal trend or transition region, as would be expected for such high Péclet number systems (see **Figure 5.5a**). This again indicates that none of the experimental bubble-melt systems are diffusion limited and provides further evidence that viscosity must still playing a role in the evolution of bubble radii. Furthermore, unless further effects are acting that have not yet been taken into consideration, it suggests that the onset of the diffusive limit occurs a Pe_b values even greater than 10^{13}.

A secondary trend in **Fig.6.10** is that the two glass datasets sit distinctly separate from the golden syrup dataset. It may be that this separation arises from natural variation in experimental data that makes the datasets appear to separate out. Alternatively, there could be an additional control on buoyant bubble resorption that differs from stationary bubble systems and has not yet been accounted for, be that redox or mixed gas species in the glass systems, or even a completely different dynamic control for buoyant bubbles in general.

Given the complexity of a decoupled resorbing bubble, this latter explanation seems most likely and therefore suggests that a further normalisation of time is required to better analyse systems described by Pe_b. This could also explain the seemingly absent onset of the diffusive limit for the decoupled bubble observations and provide an alternative solution for high Pe_b bubble radius evolutions in dimensionless space.

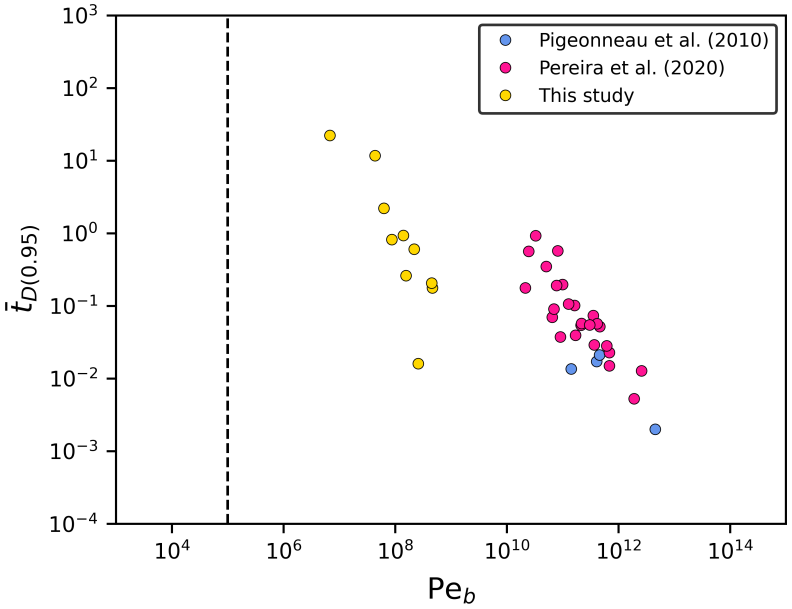

Figure 6.10: Analysis to try and find where the onset of the transition between the viscous and diffusive limits occurs for buoyant, decoupled bubbles. The black dashed line sits at a Pe_b value of 10^5 where it is hypothesised from the work on coupled bubbles that the transition would occur. The value of $\bar{t}_D$ for each dataset taken when the bubble radius falls to 95% of the initial value, $\bar{t}_{D(0.95)}$. Every dataset sits to the right of the transition line in the viscous-limited regime where it would be expected that the data falls along a horizontal line (similar to **Figure 5.5a**. Instead, the data forms a negative correlation, with values of $\bar{t}_{D(0.95)}$ decreasing as the Pe_b value of the system increases.

6.3.2 Sherwood Number Analysis

To expand the analysis of decoupled resorbing bubble systems, a further dimensionless number, Sherwood number, Sh is taken into consideration. Sherwood number is the ratio of convective mass transfer to diffusive mass transfer. It is used in both the Pigeonneau et al. (2010) and Pereira et al. (2020) studies to better account for mass transfer from a mobile phase. Pereira describes its application to the case of a decoupled bubble in a highly viscous fluid more specifically, where the bubble is considered the mobile phase and the surrounding melt as the immobile or motionless phase. As a result, the convective mass transfer term of the Sherwood number becomes an expression of the mass transferred from a bubble specifically due to it rising.

A similar description is made by Clift et al. (2005) along with an expression that shows the inherent link between Péclet number and Sherwood number.

$$\mathrm{Sh} = 1 + (1 + 0.564\mathrm{Pe}^{\frac{2}{3}})^{\frac{3}{4}} \tag{6.1}$$

For the purposes of this work, Pe in this expression is taken to be Pe_b. Use of Sherwood number in the analysis of bubble radii evolutions should therefore enable improved reduction and normalisation of data from the different gas-melt systems than buoyant Péclet number, as observed previously *(eg. Fig.9 in Pereira et al. (2020))*.

6.3.2.1 Sherwood Normalised Timescale ($\bar{t}_{Sh}$)

Incorporating Sherwood number into the normalised timescale for decoupled bubble resorption yields,

$$\bar{t}_{Sh} = \bar{t}_D \mathrm{Sh} = \frac{tD}{R_0^2}\mathrm{Sh} \tag{6.2}$$

where Sh is found from **Equation 6.1** and the effects of diffusion are still accounted for through the diffusion normalised timescale $\bar{t}_D$. Normalised bubble radii from the combined experimental datasets can then be plotted against $\bar{t}_{Sh}$ **(Fig.6.11)**.

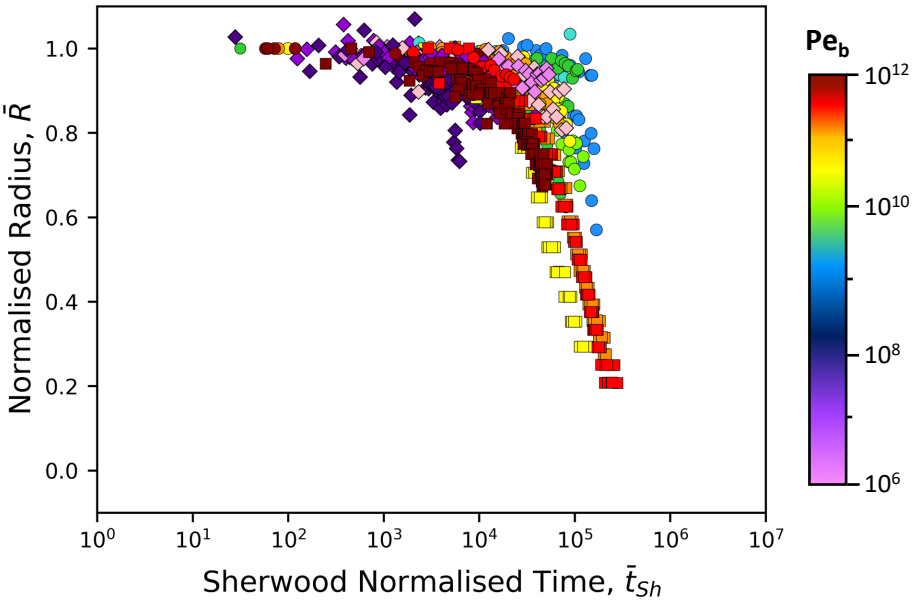

Figure 6.11: Combined datasets from this study, Pigeonneau et al. (2010) and Pereira et al. (2020) normalised to initial bubble radii and the Sherwood timescale **(Eq.6.2)**. The figure is plotted on the same scale as **Figure 6.9** to enable comparison. Each dataset is coloured according to the value of Pe_b for that system shown by the colour bar. When normalised in this way, the datasets collpase to be much closer together than when normalised to the diffusive timescale. There is also no apparent trend for the value of Pe_b between datasets.

In comparison with **Figure 6.9b**, the datasets are significantly closer grouped and appear to be tending towards complete collapse to a single radius evolution. There is still some variation in the results and the collapse is not to a completely unique curve. However, the lack of any other significant trend (for example with Pe_b value) suggests these variations are probably due to the experimental nature of the data points.

This confirms that the consideration of convective mass transfer through Sherwood normalised time provides a much better normalisation of the data and indicates there is a single limiting solution in dimensionless space for bubble radii in high Pe_b systems. If similar reduction and analysis were to be completed with simulated model results, a much clearer collapse to a single unique curve is expected.

6.3.2.2 Sh Regime Transitions

For completeness, transition analysis of the newly normalised $\bar{R} - \bar{t}_{Sh}$ data is carried out. From the observations in **Figure 6.11**, it should be expected that the data points for $\bar{t}_{Sh}$ when $\bar{R}$=0.95 will lie close to horizontal as the data is trending towards being expressed the limiting solution. **Figure 6.12** shows the results of transition analysis from the combined experimental data.

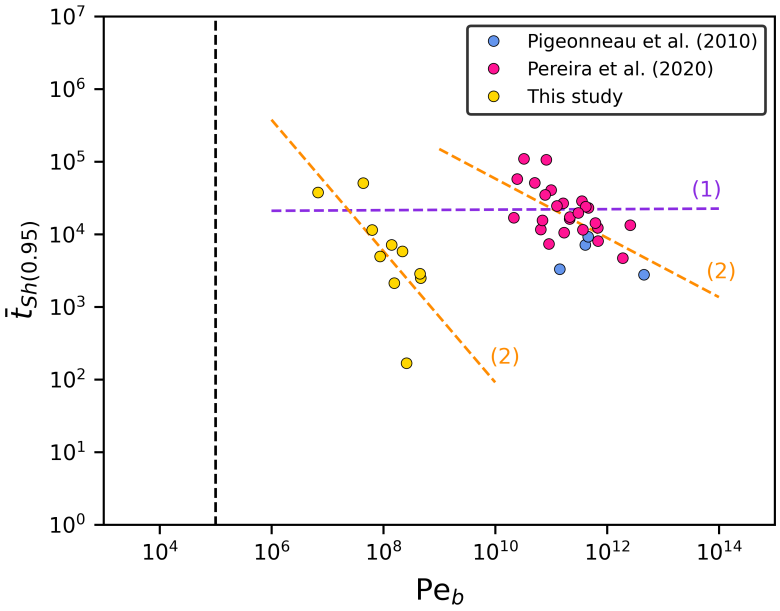

Figure 6.12: Analysis to see if the data, newly normalised to the Sherwood timescale enable the onset of the transition between the viscous and diffusive limits to be found for buoyant, decoupled bubbles. The black dashed line sits at a Pe_b value of 10^5 where it is hypothesised from the work on coupled bubbles that the transition would occur. The figure is plotted on the same scale as **Figure 6.10** to enable comparison. The value of $\bar{t}_{Sh}$ for each dataset taken when the bubble radius falls to 95% of the initial value, $\bar{t}_{Sh(0.95)}$. All datasets again sit to the right of the transition line in the viscous-limited regime and appear more spread out than in **Figure 6.10**. Two possible interpretations of the data are indicated by the purple and orange dashed lines. (1) Data sits on a horizontal trend but is scattered due to experimental variation. (2) Data is separated due to the different viscous fluids used and still displays a negative correlation.

There are two different interpretations of the data on this plot; (1) the data points show a roughly horizontal trend as shown by the purple dashed line plotted through linear regression analysis of all of the data points, or (2) the data points for the glass and syrup systems are still separated into two distinct groups which each have negative regression fits shown by the orange dashed lines. The first case would suggest that the data points sit in the diffusion limited regime and that transition to an advection limited regime would be observed in lower Péclet number systems where $Pe_b < 10^6$. The latter case suggests the Sherwood normalisation has not adequately accounted for all of the controls on the decoupled resorbing bubble system and has accentuated the separation of data from the different gas-melt systems.

Uncertainties and natural spread in the experimental data are causing these conflicting interpretations of the data, again highlighting that if it were possible to complete this transition analysis on results from model simulations, the trend in $\bar{t}_D$-Pe space would be more apparent, allowing one of the above interpretations to be rejected.

6.4 Modelling Buoyant Resorbing Bubbles

It is apparent from analysis of experimental data, that interpretations from the analysis of bubble radius observations are difficult to make as a result of variations within datasets arising from experimental error and uncertainties. Therefore, numerical models and simulations of buoyant resorbing bubbles now need to be considered and utilised in order to clarify some of the possible interpretations made in **Section 6.3**.

6.4.1 Previous Modelling Studies

In addition to Pigeonneau's experimental work in 2010, they also completed extensive work to model buoyant resorbing bubbles. Pigeonneau (2009) initially sets up the numerical problem in a similar way to this study, using several dimensionless numbers: Péclet number Pe, Sherwood number, Sh and Schmidt number, Sc (the ratio of viscous diffusion and mass diffusion rates). They express Péclet number not as a ratio of timescales but instead as a function of the other dimensionless quantities, Re and Sc such that Pe = ReSc to account for the buoyant advection of a resorbing bubble within a melt. Secondly, where their model differs from this study, the effects of redox reactions between the gas and melt are incorporated using a modification of Péclet number,

$$\mathrm{Pe}' = \mathrm{Pe}[1 + (Sa)N_{Fe}] \tag{6.3}$$

where Sa is the saturation rate of the gas species and $N - Fe$ the equilibrium constant for the redox reaction taking place. This modified Péclet number is used to redefine a modified Sherwood number, Sh' from **Equation 6.1** for a system where a rising bubble is also experiencing redox during diffusive mass transfer.

$$\mathrm{Sh}' = 1 + (1 + 0.564\mathrm{Pe}'^{\frac{2}{3}})^{\frac{3}{4}} \tag{6.4}$$

From this background theory, Pigeonneau (2009) develops an analytical solution for oxygen bubble radius evolution that accounts for the redox reaction taking place with iron in the glass melt. When tested against experimental data *(Pigeonneau et al., 2010)* this solution appears to provide a better fit than previous solutions *(eg. Ramos, 1986; Beerkens, 2002; Beerkens, 2003)*, however there is still some discrepancy, with the solution increasingly overestimating bubble radii as time goes on.

A final combined presentation of numerical and experimental work in Pigeonneau (2011) shows an updated version of the solution complete with a numerical model for bubble radii over time,

$$\bar{R}(\bar{t}) = R_0 \left[1 - \frac{1}{2}\left(1 - x - Sa - \frac{Sa}{\bar{\tau}}\right)\bar{t}\right]^2 \tag{6.5}$$

where x is the molar fraction and $\bar{t}$ a non-dimensionalised time. $\bar{\tau}$ is defined as the reduced timescale for the gas species and is used to express a normalised dimensionless timescale for mass transfer as,

$$\bar{\tau} = \left(1 - x - Sa - \frac{Sa}{\bar{\tau}}\right)\frac{\bar{t}}{2} \tag{6.6}$$

They use this timescale to normalise experimental results from different glasses, system temperatures and bubbles of different sizes for comparison in a single dimensionless space. As a result, Pigeonneau (2011) found that a single numerical solution could be expressed in this dimensionless space that gave a good fit to normalised observations from the glass melt experiments **(Fig.6.13)**. Therefore, they conclude that this solution can be used to simulate bubble radius evolutions in any decoupled bubble-melt system complete with the effects of oxidation and reduction reactions.

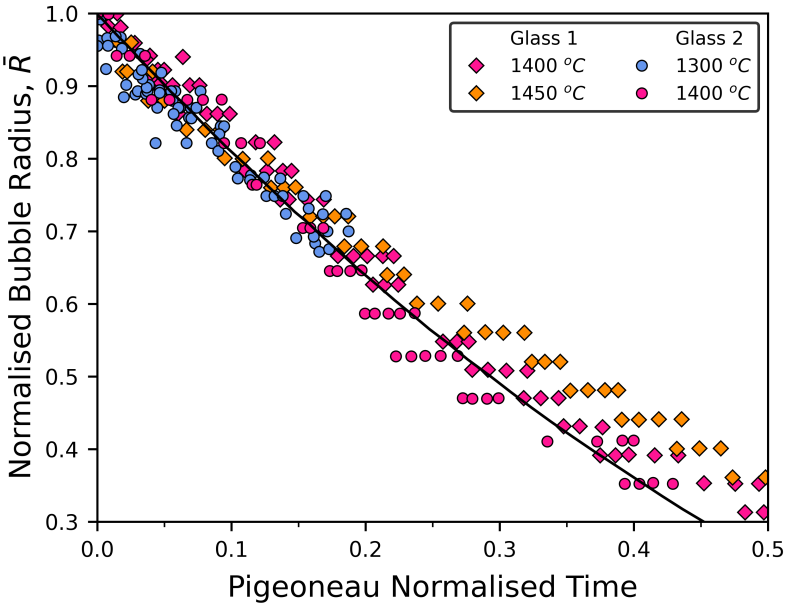

Figure 6.13: Datasets from Pigeonneau et al. (2010) **(Fig. 6.7)** normalised to a dimensionless time **(Eq.6.6)** and compared to a numerical solution **(Eq.6.5)** (black line) as set out in Pigeonneau (2011). The time normalisation pulls together the four different datasets towards a single radius evolution in dimensionless space, and the numerical solution describes this evolution fairly well. It provides the best description for the initial period of bubble shrinkage.

The later study by Pereira et al. (2020) validated the use of this model to different gas-melt systems by successfully simulating oxygen bubble radius evolutions that matched those they observed in different borosilicate glasses. These results suggest that simulations, carried out and visualised using a series of executable *C+* and *Python* scripts, can be run for different gas-melt systems by changing the input variable. Outputs of radius over time could then be analysed in a similar way to **Chapter 5** and **Section 6.3** to gain a better understanding of the Sherwood normalisation proposed in this work for describing decoupled resorbing bubbles, without the complicating factors that arise from using experimental data.

6.4.2 Simulations of Decoupled Bubble Resorption

Using the executable code developed by Pigeonneau (2011) and Pereira et al. (2020) a series of other bubble simulations were completed to show its application to other gas-melt systems and analyse the results in a similar way to **Chapter 5** and **section 6.1.3**. The aim of this was to gain a better understanding of the Sherwood normalisation proposed in this work

for describing decoupled resorbing bubbles, without the complicating factors and variation in data that arise from using just experimental results.

The input conditions of the code were adapted to model the same soda-lime-silica glass melt (Cristalica)-helium gas system used in **Chapter 5** to investigate stationary bubbles. This allowed simulations to be generated for decoupled bubbles that are comparable to those for coupled bubbles. It also provided a different glass melt system to those from previous work, which bubbles could be modelled in so see if any similarities or differences arose with those modelled in a different soda-lime glass or borosilicate glass melt.

Using the composition and material property laws of Cristalica **(see section 2.3.2.1)** and helium, model simulations were completed at 1000K and atmospheric pressure for bubbles of initial radius 0.75, 1.00 and 1.25 mm. **Figure 6.14** displays the radius outputs for the first 35000 seconds of the simulation with normalisation to the initial radius shown in **Figure 5.14b**. Each of the helium bubbles undergoes resorption into the soda-lime glass but do so over a resonably long timescale. It is difficult to decipher if the larger bubbles are resorbing faster than smaller ones as would be expected from previous observations. Running the simulations for a longer time period may help to clarify this.

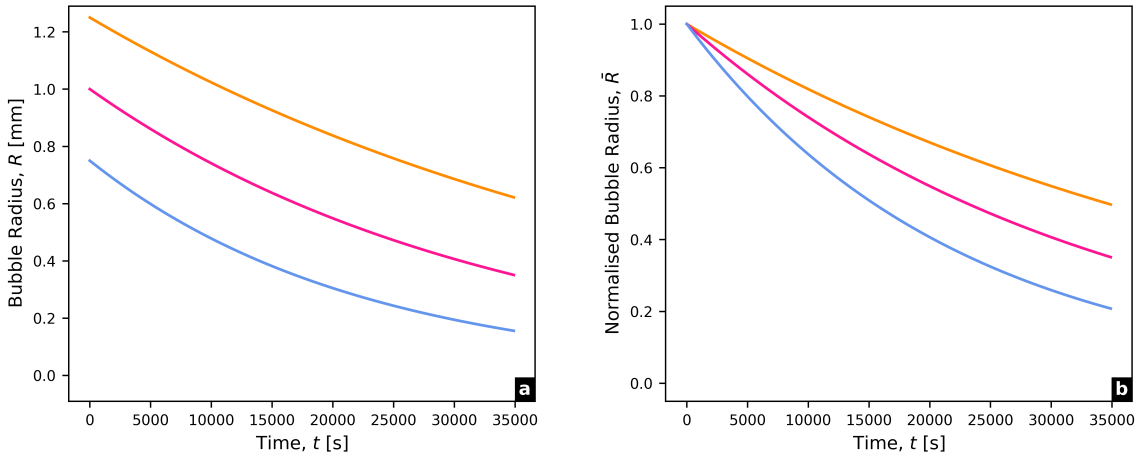

Figure 6.14: Three simulations of decoupled bubble resorption run using the model from Pigeonneau (2011) and Pereira et al. (2020) with input conditions for an analogue glass (Cristalica) and helium as the bubble gas species. **(a)** Bubble radius against time for three initially different sized bubbles. All three helium bubbles undergo resorption in the soda-lime-silicate glass melt. **(b)** Bubble radii normalised to the initial values against time for better comparison across bubble sizes.

To compare these new simulations with those from the previous literature, and better determine the trends suggested by analysis of experimental results in **Section 5.3 and 6.3**, bubble radius evolutions from a set of model runs are normalised to both the diffusive timescale, $\bar{t}_D$ and Sherwood timescale, $\bar{t}_{Sh}$ **(Fig.6.15)**. Simulations for an oxygen bubble in both soda-lime-silicate glasses from Pigeonneau et al. (2010) at 1400°C and a selection from Pereira et al. (2020) (all bubbles from glasses R-1.5 and I-1.5) are displayed for comparison.

Each of these systems sit in very high buoyant Peclet number regimes ($\mathrm{Pe}_b > 10^7$) where it would be expected that diffusion is the limiting process and thus all simulation curves collapse to a single unique solution. When plotted in diffusion normalised space **(Fig.6.15a)**, this collapse does not occur, with each curve appearing unique. There is some rough grouping of the curves according to the value of Pe_b for that bubble-melt system, but there is no collapse

to a single diffusive limit. Simulations from the helium-Cristalica system sit significantly apart from the others suggesting the specific gas and melt used is affecting the collapse of results. This further corroborates conclusions from the analysis of experimental data that there is an additional control in decoupled-resorbing systems that is not captured by diffusion normalised time alone.

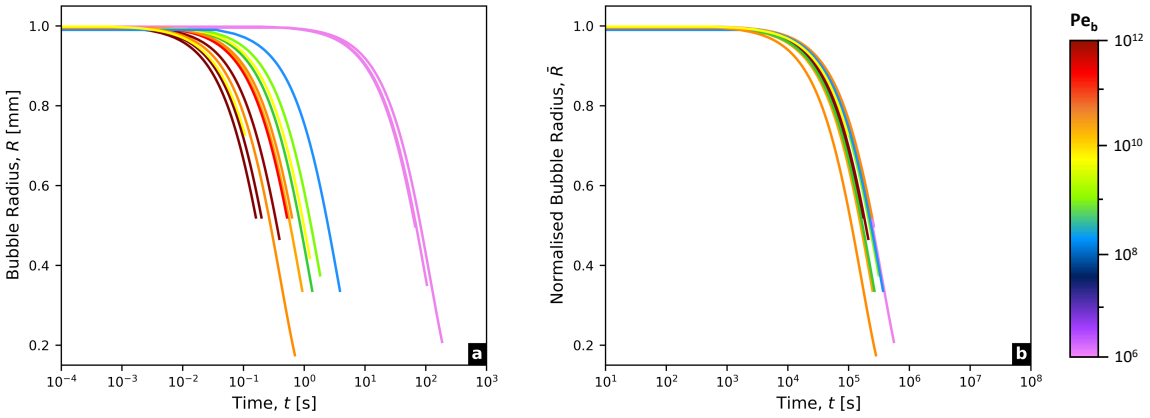

Figure 6.15: A selection of simulations from Pigeonneau et al. (2010) (Figs.3 & 6 in their paper) and Pereira et al. (2020) (all bubbles in glasses R-1.5, I-1.5 and O-1.5) alongside simulations from **Figure 6.14** for an Cristalica glass. Each simulation curve is coloured according to the value of Pe_b for that system shown by the colour bar. **(a)** Normalised bubble radii against diffusion normalised time. There is some ordering of the simulations with values of Pe_b decreasing from left to right, but the curves appear quite randomly spaced with not apparent collapse for curves with a very high Pe_b value. **(b)** Normalised bubble radii against Sherwood normalised time. The simulated curves lie much closer together with no apparent ordering accoriding to Pe_b value. This provides further evidence from **Figure 6.11** that the use of Sherwood number in the data normalisation helps identify the onset of the viscous limited regime.

In **Figure 6.15b** where bubble radius evolutions are instead normalised to the newly proposed Sherwood timescale, the simulation curves collapse much more significantly towards a single solution for bubble radii in dimensionless space. The collapse is not as perfect at that for stationary bubbles in Chapter 5 but it again helps to confirm that the idea of further controls are acting and haven't been accounted for.

Comparing now the normalised simulations with experimental data for a single gas-glass system (glass R-1.5 from Pereira et al. (2020)), it can be seen that the data and modelled curves have an excellent fit **(Fig.6.16)**. This adds to previous supporting evidence for the Pigeonneau (2011) model for decoupled bubble resorption. It also suggests that if a numerical solution can be derived for $\bar{R}$ in terms of $\bar{t}_{Sh}$, bubble radius evolutions will be able to be predicted with reasonable accuracy for system where $Pe_b > 10^7$.

6.4.2.1 Sherwood Normalised Transition Analysis

To better decide which of the two possible conclusions of the transition analysis carried out on experimental data of rising resorbing bubbles is correct **(see section 6.3.2.2)**, the same analysis is completed on the set of simulated curve output from modelling. The value of $\bar{t}_{Sh}$ is again taken when $\bar{R}$ is equal to 0.95, or 95% of the original bubble remains. These values of $\bar{t}_{Sh(0.95)}$ are then plotted against the value of buoyant Péclet number for each system **(Fig.6.17)**. This time, the data points lie much closer to a linear fit than in **Figure 6.12**

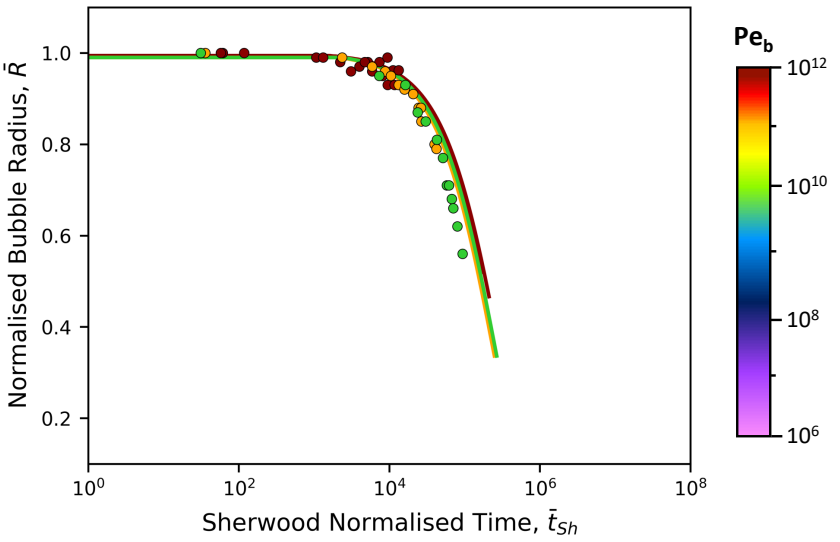

Figure 6.16: Data points from observations of oxygen bubbles in glass R-1.5 from Pereira et al. (2020) compared to simulated curves for bubble radius evolutions in dimensionless space normalised to the Sherwood timescale. Each dataset and curve is coloured according to the value of Pe_b for that system shown by the colour bar. The data and modelled curves have a very good fit, even in non-dimensional space and both similarly collapse towards a single unique solution regardless of the Pe_b value for each system.

indicating that $\bar{t}_{Sh(0.95)}$ has a unique value in the order of 10^4 for all the simulated systems that sit in the high Pe_b regime, (this is the same as one case (1) average estimated from the experimental data) and therefore that these systems sit at some kind of limit, perhaps the diffusive limit.

There is some slight variation in the datapoints which probably stems from the fact that different gas-glass systems are being modelled whereas in the original stationary bubble analysis **(Fig.5.5)**, only a single glass-gas system was used (Cristalica-Helium). The analysis where natural basaltic and rhyolitic melt inputs were used at different temperatures **(Fig.5.10 & 5.12)** did produce some variation like that on **Figure 6.17** suggesting that the exact properties of the materials in the system do indeed play a part in the exact point of regime transition.

Furthermore, the fact that the curves simulated for rising resorbing bubbles don't have a perfect collapse in Sherwood normalised space is also a further factor that would cause slight variations in the transition analysis. Nonetheless, the observations from **Figure 6.17** help to confirm that interpretation (1) from experimental data on **Figure 6.12** is correct and that these high Pe_b systems do sit in a limiting regime but one where controls in addition to diffusion that can be factored in by the use of Sherwood number also act.

Future work should aim to complete simulations of these glass systems at temperatures or with initial bubble radii that mean they sit in lower Pe_b regimes. For these, it would be expected that $\bar{t}_{Sh(0.95)}$ values would become non-constant as Pe_b reduces in value and that $\bar{t}_{Sh(0.95)}$ would get display an inverse relationship as the systems move towards a low Pe_b regime. Confirming this with either more experimental results or model simulations would provide a more comprehensive understanding of the proposed Sherwood normalisation.

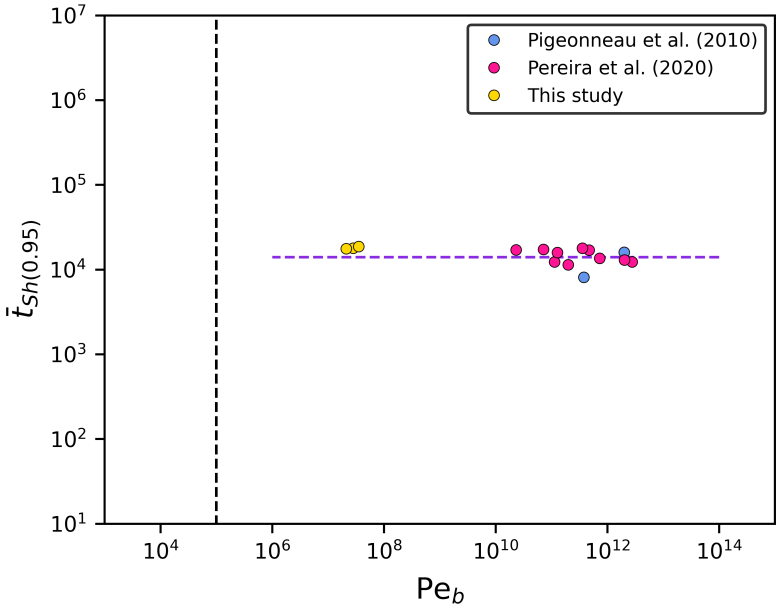

Figure 6.17: Analysis to see if the modelled simulations normalised to the Sherwood timescale enable the onset of the transition between the viscous and diffusive limits to be found more clearly than from experimental data **(Fig.6.12)**. The black dashed line sits at a Pe_b value of 10^5 where it is hypothesised from the work on coupled bubbles that the transition would occur. The figure is plotted on the same scale as **Figure 6.10 & 6.12** to enable comparison. The value of $\bar{t}_{Sh}$ for each dataset taken when the bubble radius falls to 95% of the initial value, $\bar{t}_{Sh(0.95)}$. All datasets again sit to the right of the transition line in the viscous-limited regime but this time sit much closer to a horizontal line, as would be expected for systems with such high Pe_b values that sit in the viscous-limited regime. There is still some slight varition compared with transition analysis for stationary bubbles, which may result from the Sherwood timescale not provided an entirely complete normalisation.

6.5 Buoyant Resorbing Bubbles in Natural Melts

Having comprehensively analysed decoupled bubble resorption through both experimental data and numerical simulations for a series of analogue glass systems, volatile bubble resorption in natural melt systems is now considered. Direct numerical simulations of these bubble-magma systems were not able to be completed within the scope and timescale of this project, however, potential outcomes hypothesized from the work already set out in this project are presented alongside some discussion on the expected bubble behaviours in magmatic melts. The possibility of observing single-bubble resorption experimentally in magmatic material is also discussed to explore the frontier of experimental techniques which could be applied in future work to make directly observing these complex systems a reality.

As alluded to at the beginning of this chapter of work, the buoyant Péclet number regime and all associated analysis is only applicable to basaltic magmas, as bubble sizes required to make it applicable to rhyolitic magmas would place the system in a high Reynolds number regime, in which the numerical theory and model used for simulations would be incorrect.

Therefore, a first hypothesised outcome is that if basalts with high viscosities tending towards those of rhyolitic melts were modelled, bubble radius evolutions would not be appropriately modelled using the Pigeonneau (2011) model used here. For mid-to-low viscosity basaltic melts, however, the model would be suitable, and it is expected that if bubbles were to be modelled, they would display similar trends to those in glass when analysed. Each different

system would have unique bubble radius evolution curves in dimensionless $\bar{R} - \bar{t}_D$ space. Given that it is thought other control act on these decoupled systems, none of the curves will collapse to a single limiting solution, even at very high Pe_b values. However, if analysed in $\bar{R} - \bar{t}_{Sh}$ space, a collapse should be observed at very high Pe_b values with curves then deviating away from this as Pe_b decreases.

To find the exact point at which this deviation occurs, transition analysis could be completed, which would highlight where the limiting regime begins. As with results from analysis of stationary bubbles in natural melt systems, there may be variation in the transition curves between systems of different temperatures or slightly different melt compositions. However, the overall trends would be the same with the order of magnitude estimate of Pe_b where transition occurs also being the same.

A further observation that might be expected is that a second limiting regime is entered as in **Figure 5.13**. This would occur as bubble sizes become increasing small and very low Pe_b regimes are entered. At this point, surface tension forces would play an increasing role in addition to diffusive and buoyant viscous forces.

If there were to be any direct experimental observations of bubbles resorbing in a basaltic melt, it would be expected that larger bubbles would undergo more rapid resorption over time due to have a greater TRV and thus would encounter more melt in a given time period with which to transfer mass. Rates of bubble rise and resorption would also vary greatly with the temperature of the experiment and exact basalt composition used.

Such an experiment would be practically very challenging to complete, not only due to the high temperatures and precise equipment that would be required to melt the rock sample and insert a volatile bubble, but also because of the opaque nature and iridescence of molten volcanic materials. A less direct experimental method could be designed akin to that of Jackson et al. (2022) using entrapment and cycles of heating and cooling to produce samples with a bubble contained inside which could then be sliced and analysed. But then an addition complexity of non-isothermal conditions and further practical complications such as the precision slicing of an opaque sample would have to be accounted for. Entrapped bubble sizes could be estimated from CT scanning of solidified samples such as in studies by Westrich and Eichelberger (1994), but this would come at great cost and only work best if the melt surrounding the entrapped bubble were completely bubble-free, meaning several pre-experimental preparation steps for the basalt sample would have to be applied. A project embarking on attempting to make observations of single-bubble resorption would require significant time, laboratory experience and collaboration that fell largely out of the scope of this project.

Implications of the findings in the chapter to natural magmatic bubble-melt systems are significant. The idea of decoupled resorption being plausible in several volcanic settings as shown through numerical modelling, and exploration of the possible impacts of large bubbles resorbing more rapidly could help to explain more specific magmatic scenarios such as those discussed in the introduction of this thesis. Potential for natural bubble-melt systems to be described by different values of buoyant Péclet number calculated purely from material properties, which could then allow for estimates of bubble radius evolutions with time could prove significant if factored into models for wider volcanic conduit processes or when modelling

eruption phenomenon. This significance and future potential are discussed further in **Chapter 7**.

Discussion

In this chapter, work from the entirety of this thesis is drawn together and considered side-by-side to build up a more holistic picture of the different types of bubble-fluid systems that can exist and the different bubble regimes that can arise within these systems. Developments in understanding from the hypotheses are set out before considerations of findings are made to natural volcanic systems where the bubble-fluid system consists of volatile bubbles in either a basaltic or rhyolitic melt. Differences between bubble behaviours in these two contrasting melt compositions are discussed as well as the effects of bubbles either being coupled or decoupled.

To create a visual, interpretable summary the work from individual chapters on coupled and decoupled resorbing bubbles, regime diagrams are plotted. These display plausible bubble regimes that can occur in natural systems and the physical controls that act to enhance or limit bubble resorption. A complete regime diagram spanning the spectrums of both Stokes number and Péclet number is also presented. On this, examples of bubbles observed or modelled in this study or previously literature are included to demonstrate the types of system represented by each endmember scenario. This gives a comprehensive overview of current understanding on all low-Reynolds number bubble-melt systems, highlighting also where there is need for further work to be completed. Some of these areas for potential future study are briefly discussed to highlight additional complexities that are yet to be accounted for in the modelling of bubble dynamics in volcanology.

7.1 Péclet Number Regime Diagrams

Regime diagrams build a visual picture of different types of behaviour for systems based on two or more numerical values. They are commonly used in fluid dynamics to highlight where different physical effects control a process through dimensionless quantities. A commonly used example applicable to this work is Figure 2.5 in Clift et al. (2005) which shows different bubble shapes interpretable from the values of Reynolds number and Eötvös number for a bubble-fluid system.

In this study, regime diagrams are useful to draw together observations for both coupled and decoupled systems. Using the correct dimensionless numbers, a picture can be built up of

when resorbing bubbles sit in the viscous, diffusion or surface tension limited regime, helping to build conclusions on the regimes that dominate, specifically in magmatic melts.

7.1.1 Coupled Bubble Regimes

In the work presented in **Chapter 5** on coupled, resorbing bubble systems, model simulations have shown that bubble resorption is possible in both basaltic and rhyolitic melts when there is sufficient solubility of the gas species and a large pressure difference between the bubble and surrounding melt. Stationary Péclet number works well to describe these systems with simulations produced for an analogue silicate glass alongside those for natural melts, showing significant trends according to values of Pe_s.

Normalisation of bubble-melt simulations to either the viscous or diffusive timescales leads to the collapse of normalised bubble radius evolutions at both high and low values of Pe_s. These represent the diffusion and viscosity limited regimes respectively, and show that for the majority of bubbles tested, D and μ act as the key controls on the system. As hypothesised, bubbles in a system with larger Pe_s values resorb with greater ease than bubbles in a lower Pe_s system as in the diffusion limited regime, bubble resorption takes place at the rate of diffusion, unimpeded by the viscous effects of the melt. In contrast, bubbles in a lower Pe_s system will be limited by viscosity of the melt such that mass transfer of gas may still occur, but the bubble wouldn't resorb until sufficiently overpressured that it collapses as a result of the large pressure difference.

Both of these regimes have unique solutions in dimensionless space ($\bar{R}-t_D$ or $\bar{R}-\bar{t}_v$) that are well described by numerical solutions. These allow $\bar{R}(\bar{t})$ and by extension $R(t)$ to be found for any bubble in any low Re, low Stk system where the material properties of the gas and melt are known.

The transition between the viscous and diffusive regimes which dictates the appropriate numerical solution is observed around $\mathrm{Pe}_s = 10^5$, five orders of magnitude higher than the hypothesised transition point of $\mathrm{Pe}_s = 1$ and is consistent across multiple simulations of analogue and natural bubble-melt systems.

This analysis also highlights a second limit for simulations of very small bubbles where surface tension becomes the dominant control. In this regime, surface tension effects and a very high gas pressure inside the bubble act to impede resorption. In addition to the numerical solutions for the viscous and diffusion regimes, there are adaptations of the solutions for this surface tension regime, best applicable to bubbles with a radius smaller than 1μm.

To create a better image of these different limiting regimes for coupled resorbing bubbles, a regime diagram of Pe_s against initial bubble radius, R_0 can be plotted. **Figure 7.1** shows a regime diagram for resorbing bubbles of $\mathrm{H_2O}$ in Kilauea basalt and Krafla rhyolitic obsidian melts at both a hotter and cooler temperature akin to an eruptive and storage temperature. There is a much larger difference resulting from temperature for the rhyolitic melt than the basaltic melt. This is likely due to the larger contrast in viscosity for rhyolites between storage and eruption in comparison to basalts which have more consistently low viscosities under both conditions.

The different limiting regimes of diffusion, viscosity and surface tension are also shown on

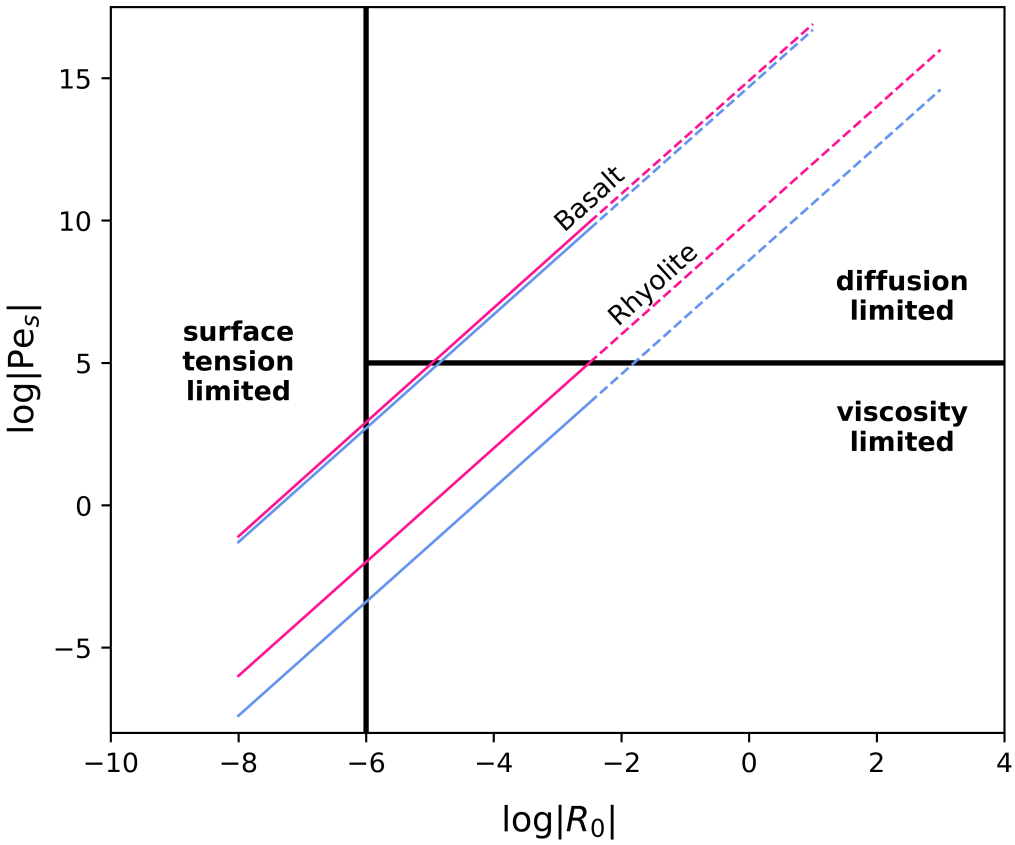

Figure 7.1: Regime diagram showing the three major limiting regimes that stationary, coupled bubble systems may sit within. The boundary between a diffusion and viscous limited regime occurs at $\mathrm{Pe}_s = 10^5$. The onset of the surface tension limited regime occurs for bubble with an initial radius of 10^{-6}m or less. Trendlines are plotted for bubbles of different sizes in a basaltic (Kilauea basalt) and rhyolitic (Krafla obsidian) melt at a hotter and cooler tempreture, denoted by the pink and blue lines respectively. For the basalt, these are 800°C and 900°C, and for the rhyolite, 1050°C and 1150°C. The trendlines are dashed for bubbles with a radius greater then $10^{2.5}$, the Eötvös radius, as these will no longer be spherically stable. Resorbing bubbles in rhyolitic melts sit entirely in the viscous or surface tension limited regimes, where as bubbles in basalt will mainly be limited by diffusion until they are small enough to be affected by surface tension effects.

Figure 7.1. In addition, trendlines are dashed beyond the point of a stable spherical bubble, dictated by the Eötvös radius, Eo which is in the order of $10^{-2.5}$ for both a basaltic and rhyolitic melt. Bubbles with radii greater than this are no longer in the Eo $\ll 1$ regime and have the potential to become geometrically unstable, forming non-spherically shaped bubbles with complex dynamics. Each of these regime spaces corresponds to where the different numerical solutions derived in **Chapter 5** are applicable.

Overall, this diagram enables conclusions to be drawn on the expected behaviours of resorbing bubbles in different magmatic melts. Stable, coupled bubbles resorbing in a basaltic melt will almost always be unaffected by the viscous effects of the melt, with only a small window of bubble sizes sitting in the viscous limited regime before radii are small enough that the surface tension effects dominate. This means that bubbles with a radius greater than 10μm will shrink in direct response to and at the same rate as diffusive mass transfer. They will remain in pressure equilibrium and not experience any collapse due to over or under-pressure. Bubbles between 1-10μm will experience some viscous effects and a pressure

contrast will build between the bubble and melt that could lead to collapse from overpressure. Finally for bubbles smaller than 1μm, surface tension will dictate the rate of resorption. This observation helps to explain the poor fit of the viscous solution in **Section 5.5.2** to simulations of stationary bubble resorption in the Kilauea basalt melt, with the only exception being the system simulated at $Pe_s = 10^4$. It can now be seen from the regime diagram that the is the only simulation that sits in the viscous limited regime and is therefore well described by the viscous solution.

Stable, coupled bubbles resorbing in a much higher viscosity rhyolitic melt sit entirely in the viscous limited regime, with only those that have a radius greater than R_{Eo} experiencing no effects of viscosity during resorption. This is due to the significantly greater viscosity of rhyolites in comparison to basalts that means at all initial bubble radii, values of Pe_s are lower than 10^5. As a result, even for the largest stable bubbles viscosity acts as the key control on bubble resorption, limiting the degree to which a bubble can shrink until the pressure contrast is so great that the bubble collapses. This explains the excellent fit of both the complete and simplified form of the viscous solution derived in **Chapter 5** to simulations of bubbles in rhyolitic obsidian from Krafla. In addition, the onset of the surface tension regime for bubbles smaller than 1μm further justifies the need for the small radius solution that uses the capillary timescale to predict bubble radius evolutions with good accuracy.

7.1.2 Decoupled Bubble Regimes

Work on decoupled resorbing bubble systems in **Chapter 6**, whilst less numerically comprehensive than the work on coupled resorbing bubbles, adds to experimental observations of bubble resorption and presents some model simulations of a previously validated code in a range of high-viscosity analogue fluids. The smaller scope of this work highlights the high level of complexity of trying to model a bubble that is simultaneously rising and diffusively transferring mass. Whilst not complete in its analysis here, advancements in understanding of this type of system have been made, which lay the foundation for future work to continue on with the aim of obtaining comprehensive numerical solutions for decoupled, resorbing bubbles.

An important development from the hypotheses is the interpretation of what a high Pe_b or low Pe_b system mean in terms of bubble resorption. It may be expected from a first glance, as hypothesised earlier on, that in high Pe_b systems bubbles would not undergo large amounts of resorption as the advective rise timescale is much shorter than the diffusive timescale. Hence, the bubbles wouldn't be resident in the melt long enough to diffuse to any significant degree. Oppositely for a low Pe_b system, it might be thought that bubble would undergo resorption with greater ease as residency time in the melt would be much longer and thus there is more opportunity for mass to transfer into the surrounding melt.

However, both new experimental observations measured in gold syrup and those from past studies in molten glasses show that larger bubbles, which yield higher Pe_b values for the systems due to the third order relationship of R_0 and Pe_b, or bubbles in hotter melts where viscosity is reduced, resorb faster than lower Pe_b where bubbles are smaller or the melt cooler.

This contradiction therefore leads to a rethinking in the interpretation of buoyant Péclet number. It is instead that larger bubbles in higher Pe_b systems, will undergo more rapid

resorption due to rising faster through the melt meaning they will encounter more 'new' melt in a given time. Continually rising into this 'new' melt is equivalent to the melt saturation begin kept consistently low, or concentration gradient consistently high so that mass transfer is a favourable process. For smaller bubbles in lower Pe_b systems, rise velocities will be slower meaning the bubble sits in the same region of melt for longer, allowing for it to become saturated or the concentration gradient to drop so that diffusive mass transfer is very slow. In extreme cases where bubble rise velocity is very slow, the system becomes equivalent to a stationary, coupled system marking a limit for the use of Pe_b.

A further key idea introduced in **Chapter 6** is that of Sherwood number, as the use of just buoyant Péclet number, Pe_b and diffusion normalised time, $\bar{t}_D$ is insufficient to capture different regimes of bubble behaviour. For both the experimental data and model simulations, using an adaptation of the diffusive timescale, the Sherwood timescale $\bar{t}_{Sh}$, normalised bubble radius evolutions in very high Pe_b systems begin to collapse towards a single unique solution like those for coupled resorbing bubbles in the diffusive regime. The need for this extra normalisation was not hypothesised and suggests that additional controls act in decoupled systems that are affecting the dynamics of bubble rise and diffusion.

Sherwood number allows the effects of convective mass transfer to be accounted for suggesting this is necessary for systems where there is a relative velocity between the bubble and surrounding fluid. However, use of Sherwood number alone does not yet provide as comprehensive a collapse as would be expected and therefore leave questions remaining about the other controls that could be acting and how they could be accounted for. As a result of this missing link, complete numerical solutions for bubble radius evolutions either in dimensional or dimensionless space have not yet been derived, other than those used in the model developed by Pigeonneau (2011).

Nevertheless, a regime diagram can still be pieced together from the experimental and simulation results, then extended to natural magmatic melt systems to allow for further discussion on additional controls that might be acting and the significance to volcanic systems. **Figure 7.2** shows this regime diagram which has Sherwood number plotted against initial bubble radius. Experimental data is displayed as datapoints and trendlines shown for analogue glass melts and the natural systems of H_2O bubbles in Kilauea basalt and Krafla rhyolitic obsidian. The natural melts are again shown at two different temperatures to represent a hotter eruptive temperature and a cooler storage temperature.

A regime transition line is shown at $Sh = 10$ as this is where the trendlines experience a change to a constant gradient and therefore is where a consistent relationship between Sherwood number and initial bubble radius begins. One interpretation of this is that above this line ($Sh \gg 10$) a system will be diffusion limited, and below this ($Sh \ll 10$) it will be buoyantly limited as viscosity of the surrounding melt is too great for the buoyancy of the bubble to easily overcome.

The radius at which bubbles become spherically unstable, the Eötvös radius, R_{Eo} is again indicated by dashed lines. Since simulations of much smaller bubbles were unable to be complete in this work, only these two major regimes are shown as the onset point of a possible surface tension regime is unknown. The final regime shown on **Figure 7.2** marks where the

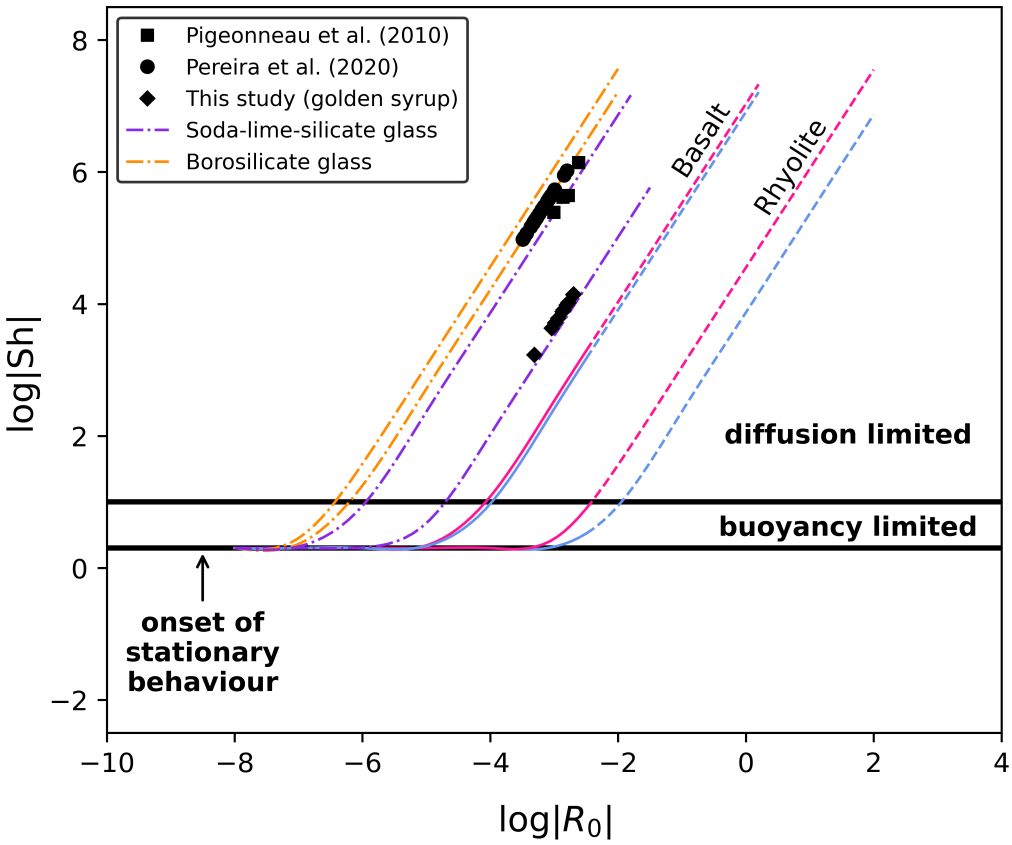

Figure 7.2: Regime diagram showing the three major limiting regimes that buoyant, decoupled bubble systems may sit within. The boundary between a diffusion and buoyancy (viscosity) limited regime occurs at Sh=10. Trendlines are plotted for bubbles of different sizes in a basaltic (Kilauea basalt) and rhyolitic (Krafla obsidian) melt at a hotter and cooler tempreture, denoted by the pink and blue lines respectively. For the basalt, these are 800°C and 900°C, and for the rhyolite, 1050°C and 1150°C. Additional trendlines are shown for some of the analogue glass melts studied in this work as well as data points for systems observed in experimental work. For all trendlines, as Sh approaches $10^{0.3}$, there is a plateau to a constant value regardless of bubble radius. This indicates the onset of where viscous forces are so great that the systems can essentially be considered stationary or coupled. The trendlines for the magmatic melts are dashed for bubbles with a radius greater then $10^{-2.5}$m, the Eötvös radius, as these will no longer be spherically stable. Bubbles in rhyolitic melts sit entirely in the buoyancy limited or stationary regimes, meaning decoupled resorbing spherical bubbles in rhyolitic melts are unlikely in nature. Bubbles in basaltic melts can sit in the diffusion limited regime as well as the buoyancy limited or stationary regimes for smaller bubbles.

movement of decoupled bubbles becomes so minimal that they are effectively stationary in the melt and therefore better described by the stationary Péclet number, Pe_s. This is observed as the value of Sherwood number approaches $10^{0.3}$.

The first thing highlighted by this regime diagram is that stable decoupled bubbles that resorb unimpeded by viscous effects cannot exist in the rhyolitic melt as the limit of bubble stability coincides with the transition to a diffusion limited regime. Therefore, any decoupled bubbles undergoing resorption in a rhyolite will experience large viscous forces that inhibit buoyant rise and prevent bubbles from being able to interact with new melt that can accommodate the transfer of mass. The window of bubble radii that sit between this viscous-diffusive limit and the onset of a stationary regime is relatively small, suggesting that only bubbles with radii on mm or cm scale will be able to buoyantly resorb in a rhyolitic melt. This is

reasonably large for bubbles trapped in such high-viscosity melts, so it is likely that most bubbles found naturally in melts such as obsidian will be effectively stationary.

By contrast, stable decoupled and resorbing bubbles in a basaltic melt can sit in both the diffusion and viscous limited regime. For bubbles larger than 100μm in radius, diffusion becomes the limiting control on the system meaning bubbles will shrink directly in line with the rate of diffusion as viscosity of the surrounding melt has no effect. Bubbles with radii smaller than 100μm, down to around 10μm will experience viscous limiting effects in the melt as buoyancy of the bubble is reduced and therefore rise velocity through the melt gets slower. For bubbles smaller than 10μm, viscous forces are so great and bubble buoyancy so small that they then become stationary in the melt and would instead undergo coupled resorption in the diffusion or surface tension limited regime.

In addition to trendlines for natural melts, experimental data and trends calculated for some of the analogous glass melts referred to throughout this thesis are included for completeness. Some interesting observations from the addition of these is that melt viscosity reduces from right to left, which if extended to natural melts, suggests that trends for higher viscosity melts will sit further to the right than those for lower viscosity melts. Secondly, the trendlines for two different soda-lime-silicate glasses (Cristalica and that used by Pigeonneau et al. (2010)) sit quite separate from one another, indicating that the position of the trendline depends heavily on the exact melt composition and that melts of the same wider category may not always group together. This raises a question about where trends would lie for other natural melt compositions that are more unusual or sit outside the compositions of basalts or rhyolites, such as phonolites or andesites, presenting another topic for future work or discussion.

7.1.3 Significance to Volcanology

The regime diagrams created to show where the onset of different controls lie for magmatic bubble-melt systems give a great insight into the types of behaviour that can expected to occur in natural systems. Furthering from this, the implications of these different behaviours under different conditions can be used to discuss impacts to a wider volcanic system and the plausibility of scenarios where it is thought bubble resorption may be able to take place.

7.1.3.1 Coupled Systems

The key finding of studying coupled bubbles is that in rhyolitic melts, resorbing spherical bubbles will always be affected by the high viscosity of the surrounding magma. From this, it can be interpreted that these bubbles will experience large overpressures that result in them suddenly collapsing in on themselves to leave a regassed bubble-free melt when a threshold overpressure is reached, rather than gradually resorbing as mass is diffusively transferred out into the melt. Considering this in the context of a volcanic scenario, foam collapse following non-explosive silicic eruptions, the confirmation that bubbles trapped in rhyolite are viscously limited at both eruptive and storage temperatures, and shrink due to large pressure contrasts supports the hypothesis of Eichelberger et al. (1986) and experimental work of Westrich and Eichelberger (1994) that showed the decompression of rhyolitic foams could produce samples

reduced in volume by up to 50%.

Whilst the results from this thesis cannot estimate the degree to which resorption would take place, or the final vascularity of a melt sample where resorption had occurred, they provide strong evidence that if bubbles have an internal pressure much lower than the surrounding melt, as occurs following permeable foam collapse, they will be resorbed to some extent and may even undergo complete collapse to leave a bubble-free melt. The smallest bubbles may be preventing the production of bubble-free material forming if surface tension effects are too great to allow for complete collapse. In this case, material with a higher vesicularity may be yielded following foam collapse, as thought by Gardner et al. (2017) or Wadsworth et al. (2020).

It could be useful to produce trends for the regime diagram where pressure is varied instead of temperature. This would allow the bubble regimes at different storage pressures (depths) to be interpreted so that estimations of the required magmastatic pressure for bubble resorption following foam collapse could be made. It could also help to understand if bubble resorption is more plausible under deeper storage conditions, or shallower eruptive conditions.

A second scenario considered for stationary bubble resorption is in densely welded layers of obsidian within pyroclastic deposits. It has been proposed that if these deposits cool slowly enough, there will be sufficiently time for diffusion and for bubbles to resorb. However, as the regime diagram **(Fig.7.2)** shows, it would also require there to be a significant pressure difference between the bubbles and surrounding deposit so that the limiting viscous effects of the obsidian melt can be overcome. Therefore, it could be that bubble resorption in PDC deposits is only possible in very thick, dense deposits that would provide enough overpressure for bubbles to collapse. For the very smallest bubbles that would be dictated surface tension effects, the pressure disequilibrium would have to be large enough to also overcome these. Similarly to the foam collapse scenario, understanding the regimes of bubbles under different system pressures would help determine amount of pyroclastic deposit required to generate sufficient overpressure for bubble resorption.

The two previously hypothesised scenarios for coupled bubble resorption focused on stationary bubbles in a motionless rhyolitic melt phase; basaltic melts were not discussed. **Figure 7.2** shows that coupled bubbles in lower viscosity basaltic melts have the potential to undergo both diffusion and viscous limited resorption. Whilst it is unlikely that bubbles will sit stationary in a basaltic melt due to its lower viscosity, it is possible that bubbles may move simultaneously to the melt as it ascends thus remaining coupled. For resorption to then occur this case, it is likely that saturation of the melt would have to become thermally altered if it is assumed the bubbles are remaining in the same melt they were exsolved from which has therefore already reached its saturation limit. Magmatic melt saturation increases as temperature decreases meaning if the basaltic magma is cooling whilst rising with the bubbles, it may be able to accommodate more volatile mass leading to diffusive mass transfer and resorption. Under these conditions, larger bubbles would resorb at the rate of diffusion and shrinkage of any smaller bubbles would become impeded by either surface tension or viscous effect. However, cooling of a buoyantly ascending bubbly basalt would be quite unusual in a magmatic setting, leading to the conclusion that, despite being able to be modelled, stationary

resorbing bubbles are most likely to occur in rhyolitic melts.

If instead, an extrusive scenario for coupled bubbles in basaltic material is considerd, where bubbles are trapped within a clast of melt ejeted during an eruption, cooling that would result in an increase in volatile saturation is much more plausible. It could be expected in this case that the bubbles would undergo diffusion limited resorption into the cooling clast material, leaving behind halos of increased volatile concentration in the preserved material. However, these halos are not always observed which could lead some to think the bubbles are not diffusion-limited. Taking typical lengthscales for a basaltic pyroclast (10^{-2}m) and values of thermal and volatile diffusivity ($D_T = 10^{-8}\text{m}^2\text{s}^{-1}$ and $D = 10^{-12}\text{m}^2\text{s}^{-1}$), it is found that the cooling timescale ($\lambda_c = a^2/D_T$) is several orders of magnitude longer than the volatile diffusion timescale, λ_D for bubbles μm scale bubbles ($\lambda_c/\lambda_D = 10^4/10^2$). This explains why despite being diffusion-limited, no concentration profiles are observed radiating from trapped bubbles, as the cooling has been so long that the volatiles have equilibrated with the surrounding melt before being 'frozen' into the cooled material. For small bubbles in large clasts, this effect will be even more enhanced, however for bubbles in much smaller clasts, the two timescales become a lot more similar meaning concentration profiles may be observable in field samples.

7.1.3.2 Decoupled Systems

The regime diagram for decoupled bubble systems displays an opposite conclusion to the coupled regime diagram, with resorption of spherically stable rising bubbles only being favourable in basaltic melts rather than rhyolites. This is due to the high viscosity of rhyolites that means bubbles would have to be very large to be sufficiently buoyant that the buoyancy would affect the dynamics of diffusive mass transfer. At this size, the bubbles would no longer be described by the underpinning theory of this thesis which relies on low Reynolds and Eotvos number. Any hypothesised scenario involving decoupled spherical bubbles in rhyolitic melts can therefore be dismissed.

Rising spherical bubbles can resorb in basaltic systems which validates the plausibility of the scenarios set out for this case in **Section 3.1** for bubbles larger than 1μm in radius. This has major significance to volcanic processes and suggests that models or eruptive processes should also take alterations to melt compositions or dynamics as a result of resorption into account. Furthermore, resorption should be considered more widely in studies attempting to explain sequences of processes that produce certain volcanic phenomena.

In respect to interpreting eruptive or intrusive volcanic materials, **Figure 7.2** hints at observations that could expected in preserved magmatic products if dynamic bubble resorption has occurred. If resorption of buoyant bubbles has taken place, rapidly quenched samples of basaltic melt would display different patterns of volatile concentration in the preserved glass depending on the bubble size. Around an originally smaller bubbles would have been viscously limited or effectively stationary, haloes of increased volatile concentration will radiate out from a vesicle or from a point where a vesicle once was. Around originally larger bubble that would have sat in the diffusion limited regime and therefore would've continued to rise

during resorption, streaks or haloes with tails of increased volatile concentration would be preserved in the melt as the bubble leaves behind melt it has transferred mass with. Vesicles in rhyolitic melts where resorption is suspected to have taken place would display haloes of increased volatile concentration around the remaining bubble. In extreme cases of complete resorption, circular patches of increased concentration may be all that remains. Looking for these patterns of regassing in rapidly quenched melt samples could provide a vital piece of observational evidence to support theories of bubble resorption in volcanic systems.

7.2 Péclet Number-Stokes Number Regime Diagram

In addition to regime diagrams for the individual types of bubble system, a further regime diagram can be constructed that draws both systems together to consider a representation of all the work in this thesis. Using Stokes number and Péclet number as the two primary dimensionless quantities, and Sherwood number as a secondary quantity, the different types of bubble-melt system can be shown in relation to one-another **(Fig.7.3)**.

Within the diagram, example studies conducted into each type of system are listed, along with highlighted regions showing where different numerical solutions or models for bubble dynamics are applicable. This diagram therefore provides an overview of the current extent of understanding on the dynamics of bubbles in high-viscosity melts.

Hypothesised transition lines are shown at values of Stk and Pe where a system would change distinctly between two different types of behaviour. For Stokes number this is the transition between a coupled and decoupled system, and for Péclet number the transition between a viscous limited or diffusion limited solution. On the right-hand axis it is shown that bubbles lying in the upper-half of the diagram would be best described by buoyant Péclet number, whereas for those in the lower-half, stationary Péclet number would provide a better description. At the upper limit of the diagram, Sherwood number may need to be considered to better distinguish between buoyant resorbing systems. Regions where different effects act to limit the system are shown, along with depictions of where different solutions for bubble dynamics are applicable. These include some of the specific solutions from this thesis set out in **Chapter 6**, as well as those from previous modelling studies or classical theory *(Hadamard, 1911; Rybczynski, 1911; Prousevitch et al., 1993; Pigeonneau, 2011; Coumans et al., 2020; Jackson et al., 2022)*. Experimental datasets considered throughout this thesis are also plotted for comparison. To use this regime diagram, the material parameters of a system should be used to calculation the value of Stk. If Stk is much greater than one, or bubbles are known to be decoupled, Pe_b should then be calculated from further material parameters of the gas and melt. If Stk is much less than one, or bubbles and melt are known to be coupled, Pe_s should then be calculated in a similar way. From there, the region of **Figure 7.3** in which the system sits in will be apparent and the most applicable model for bubble dynamics can be determined.

Positions of the four main endmember dynamic cases, coupled non-resorbing bubbles, decoupled non-resorbing bubbles, coupled resorbing bubbles and decoupled resorbing bubbles, sit in similar relation to that hypothesised in **Figure 3.1**, but have a more complex configuration than just being situated towards each corner. The main cause of this difference is the

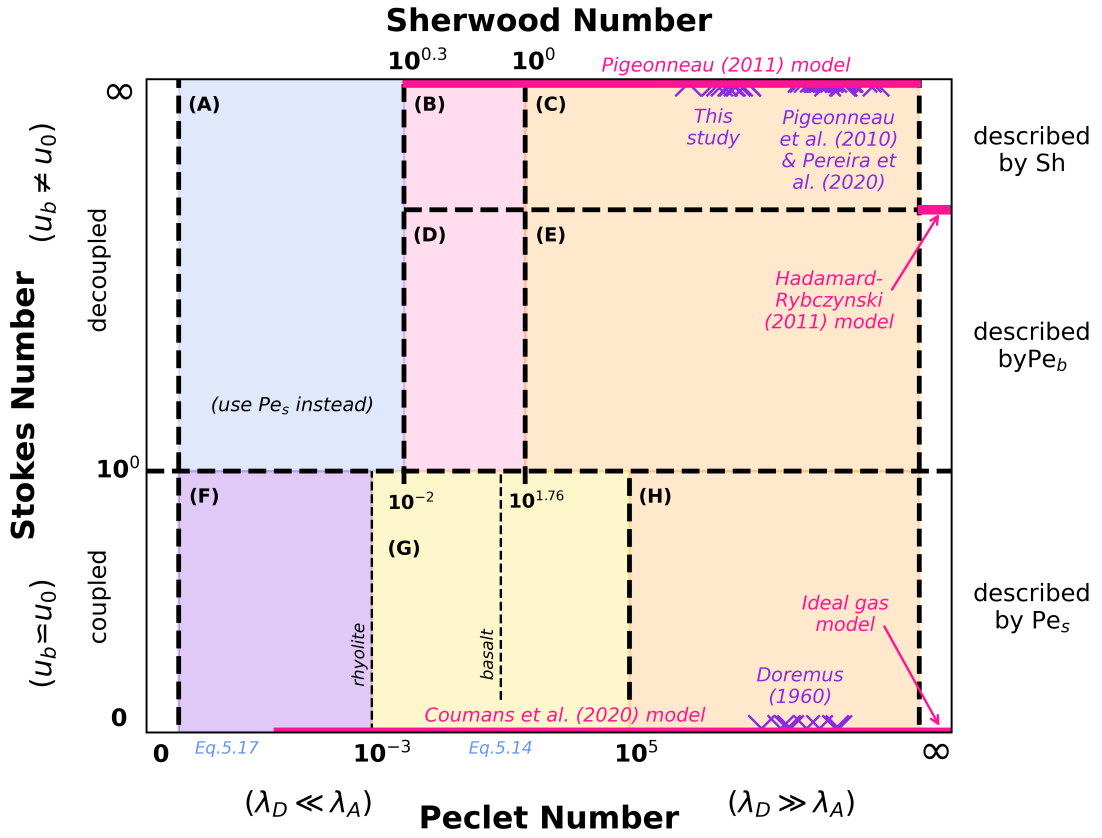

Figure 7.3: Regime diagram covering all of the different regimes of behaviour discussed in this work for both coupled and decoupled bubbles. Degree of bubble coupling is determined by the Stokes number axis, with the transition occurring at Stk=1. Sherwood number or Péclet number is used on the x-axis to determine the regime of behaviour. In areas shaded blue **(A)** bubbles are essentially stationary, in pink areas **(B,D)** they are buoyancy limited, in orange areas **(C,E,H)** diffusion limited, yellow areas **(G)** are viscosity limited and bubbles in purple areas **(H)** are surface tension limited. Two thinner black dashed lines are shown in Area G where the onset of the surface tension regime is observed for both a rhyolitic and basaltic melt. Regions where certain models for bubble dynamics are applicable are shown as bold pink lines. Any datasets observed are shown with purple markers. Regions where numerical solutions presented in this work are applicable are shown with blue text. Overall, the diagram highlights where past work has been able to develop understanding, as well as where there are gaps in knowledge for future work to focus on.

development that more rapidly rising bubbles described by higher values of Péclet number will resorb faster, thus placing them further to the right of the regime diagram. In addition, at low values of buoyant Péclet number (or Sherwood number) bubble rise is so negligible they are better described by stationary Péclet number, nullifying a large area up to the upper-left of the diagram.

One remaining limitation of this Stk-Pe regime diagram is that regions between each endmember are not that well accounted for in terms of experimental data or modelling. This includes, for example, systems where the degree of bubble coupling is less definitive so that bubbles may be moving within a melt that is also moving but at a different velocity. In this case, the system is decoupled but to a lesser extent than if the melt were stationary **(Fig7.3areaG)**. As a result, the ratio of bubble and melt velocities (Stokes number) is neither tending towards an infinitely large or small value and sits somewhere in-between, requiring a different solution to be able to model the bubble dynamics. Nonetheless, the relative position of this bubble system to others in Stk-Pe space and the key control being diffusion rate would be known and

may help to estimate some of the expected bubble behaviours or system dynamics.

It would now be appropriate to collect together further datasets from bubble systems of various gases and melts for plotting onto this diagram to see if any further trends between systems, either magmatic or non-magmatic, become apparent. Some trends that would be expected from the numerical descriptions of Pe and Stk have been shown on **Figure 7.3**, but confirming these with observational evidence has potential for a future study. It would be especially potent to plot datasets or trends from systems with intermediate degrees of coupling to build better understanding of the relationship between Stk and Pe beyond the endmember cases.

Conclusions & Extensions

The aim of this thesis was to build upon existing work on bubbles in high-viscosity fluids with a principal focus on the dynamics of bubble resorption in both coupled and decoupled systems. This was done using dimensionless quantities, principally Péclet numbers, to explore the controls and limits to bubbles of different sizes in different melt compositions, and the boundaries between different bubble regimes. Exploring the topic in this way has enabled a development in understanding from the hypotheses originally set out, as well as some additional findings made along the way to addressing the principal aims of the project. It has also highlighted the extent to which there is room to expand even further on the topic of bubble resorption dynamics, especially in the context of volcanic systems, leaving several avenues for further valuable research.

8.1 Conclusions

After extensive analysis of the four hypothesised endmember of limiting bubble regimes and experimental work to generate new observations of bubble resorption, the following conclusions are drawn:

1. Two different definitions of Péclet number enable regimes of bubble behaviour in coupled or decoupled systems to be better differentiated, as they take into account different definitions of advection for the two types of system. Each system simulated in the study had a unique value of Péclet number based on the input conditions and there were several trends observed based on the order of magnitude of these Péclet number values.

2. The stationary Péclet number proves comprehensive for describing coupled bubble systems, whereas the buoyant Péclet number had limitations. It was found that for systems described by very high values of buoyant Péclet number, the additional factor of Sherwood number became more appropriate to distinguish between different regimes of behaviour.

3. In bubble systems where there is no resorption, bubble growth or shrinkage will be entirely controlled by changes to temperature and pressure.

4. Numerical simulations of coupled resorbing bubble systems show there to be three main regimes of bubble resorption: diffusion limited, viscous limited or surface tension limited. The transition between the diffusion limited regime where resorption occurs at the rate of gas diffusion into the melt and the viscous limited regime where the surrounding fluid is slow to respond to the equilibration of the bubble radius following mass transfer, occurs around $\mathrm{Pe}_s = 10^5$. Therefore typically, larger bubbles are diffusion limited whereas smaller bubbles are viscously limited. For the very smallest bubbles surface tension effects become dominant in limiting the rate of bubble resorption when $\mathrm{Pe}_s \ll 1$ ($R_0 < 10^{-6}$m).

5. Numerical simulations of decoupled resorbing bubble systems show there to be two main regimes of bubble resorption: diffusion limited and buoyancy limited, where viscosity of the surrounding melt restricts the buoyant advection of the bubble. The transition between these two regimes is best captured using Sherwood number, occurring at Sh=10. An additional observation when Sh$\rightarrow 10^{0.3}$ is that bubble buoyancy is reduced so significantly that the bubble can be considered as coupled to the melt and are therefore better described by the stationary Péclet number.

6. Stable spherical bubbles in rhyolitic systems are almost exclusively coupled due to high melt viscosities. As a result, they are also viscously limited and described by lower values of Pe_s and Sh<10.

7. Stable spherical bubbles in basaltic systems can be coupled or decoupled due as melt viscosities are lower. Therefore, they almost always diffusion limited and described by higher values of Pe_s and Sh>10. When coupled, the relative timescales of melt cooling and diffusion means that despite being diffusion limited, neutral volatile concentration profiles are observed extending from the bubble edge. This is due to equilibration with the surrounding melt during slow cooling following mass transfer. When decoupled, tails or streaks of increased volatile concentration may be observable in rapidly quenched material as a result of the bubble rising simultaneously to resorbing.

8. Experiments completed using CO_2 bubbles in golden syrup provides further support for the use of syrup as a laboratory-scale analogue for magma. Observations collected corroborate with existing datasets for decoupled resorbing bubbles, where initially larger bubbles appearing to resorb at a faster rate than initially smaller bubbles. In an improvement to understanding from the hypotheses, this means that in high Pe_b systems, bubble resorption actually occurs faster than in lower Pe_b systems. This is attributed to larger bubbles, rising faster through the surrounding melt and therefore continually encountering new melt equivalent to continually resetting the concentration gradient between the bubble and distal melt or maintaining a consistently high solubility.

9. The four endmember bubble regimes hypothesised can now be expressed in terms of numerical values of Péclet number and Stokes number as shown on the regime diagrams plotted. Whilst endmember cases do exist, the boundaries between them are much more fluid, with a spectrum of both Péclet number and Stokes number being plausible in volcanic systems.

8.2 Topics for Future Study

With this thesis giving a comprehensive overview of current understanding on the different types of bubble-fluid systems that may occur, with focus to those that are plausible in higher viscosity magmatic bubble-melt systems, it has also encountered scenarios where there are limits to understanding and therefore room for future research. The following list, whilst not exhaustive, sets out some of these areas where developing knowledge through further study would be important in working towards a complete understanding of bubble dynamics in volcanic settings.

8.2.1 Developing a Diffusion Limited Solution for Coupled Bubble Resorption

One significant area for future study is the development of a numerical solution for coupled bubbles in the diffusion limited regime. Such solutions have begun to be explored by Doremus (1960) and Clift et al. (2005), but are still far from the solutions presented in this work for the viscous and surface tension regimes, or models such as that by Coumans et al. (2020).

A solution for bubble radius evolutions in this regime are of particular importance to applications in volcanology as it would be applicable to bubbles in basaltic melts, most of which sit in this diffusion limited regime. Being able to calculate bubble radius at any given point in time from input parameters of the system would be invaluable to the wider modelling of eruptive basaltic systems.

8.2.2 Developing Solutions for Decoupled Bubble Resorption

Whilst the model by Pigeonneau (2011) provides an appropriate fit to experimental data from oxygen-molten glass systems, it would be interesting to extend investigations by adapting the model to run with magmatic melt and volatile bubble inputs. In addition, the reactionary sections of the model set up to simulate redox could also be applied or adapted for other reactions that may take place between the bubble gas phase and surrounding melt.

More analytical solutions for dimensionless coefficient, similar to those set out in **Chapter 5** for coupled resorbing bubbles, would be good to develop in addition to a complete numerical model. However, this would require better normalisation of data first. Whilst the Sherwood normalised timescale begins to suggest the effects of convective mass transfer need to be accounted for, there is still room improvement and a more definite normalisation to collapse data from decoupled resorbing systems.

If possible, improved solutions or models would enable bubble radius evolutions for any decoupled bubble-melt system to be simulated from the material parameters and input conditions of the system. This would prove pivotal to the modelling of wider eruptive processes in volcanoes where bubbles play an active part.

8.2.3 Intermediate Stoke Number Systems

Within the development of this decoupled bubble resorption solution for a magmatic setting, it would be important to build in the possible effects of intermediate Stokes number where a bubble may be moving in a melt that also has an ascent velocity. As highlighted in

section 7.2, this is a region of significant unknowns in current understanding, but given it is a likely scenario for a lot of natural volcanic settings, it is important to build it into any new model. In addition to being modelled, collecting observational data of rising bubbles in a non-stagnant melt would also give an insight, as datapoints could be plotted onto **Figure 7.3** to see the relationship between Stk and Pe or Sh as Stk changes as well. It may be that there are further dimensionless quantities that could be expressed to describe the ratio of Stk to Pe, similar to Morton number in the Re-Eo regime space.

8.2.4 Temporal & Spatial Changes

The current definitions of Péclet number set out in this thesis use the initial conditions of a system to define a value of Pe_b or Pe_s. In magmatic systems where there are constant changes to conditions in both time and space, it may be more appropriate to have a Péclet number that changes in line with these conditions. This would mean it is plausible that the Péclet regime of a system is not fixed at a constant value. Different regions of the same system may be in different limiting regimes as things like temperature or pressure vary, meaning that bubbles experience different controls on their behaviour as they migrate through the system, sometimes being diffusion limited and able to freely resorb, other times being viscously limited and experiencing larger amounts of overpressure, or occasionally even being under conditions that don't allow for any resorption.

Furthermore, as the radius of a bubble changes because of resorption, a Péclet number that accounts for these changes would mean the value used to describe the system would change over time. This could be a good way of determining where the onset of different controls may be such as if a bubble resorbs to become so small that surface tension then limits any further resorption. Rather than just determining the initial limiting controls of the system, a dynamic Péclet number would allow changes in these controls over space or time to be observed.

8.2.5 Two-way & Reactive Diffusion

As shown in the numerical solution of Pigeonneau (2011), reactions between bubbles and melt during rise and resorption can be accounted for when modelling bubble radius evolutions. To extend this, the effects of other reaction processes would be good to build into models used specifically for magmatic melts and volatile bubbles.

Another factor which has not yet been considered is the possibility for two-way diffusion, where one gas species moves from the bubble into the melt and a secondary gas species from the melt into the bubble. This would be a simultaneous ragassing and degassing of melt as the gas species are exchanged. In terms of bubble radii, bubbles would not necessarily shrink as mass is being replaced as it is being removed. If replacement with the new species takes place at a slower rate than removal of the original gas, the bubble may shrink, but not to complete resorption. However, the bubble size also depends on the volume that the new gas occupies according to its ideal gas law. Therefore, a smaller mass of the new gas species may actually occupy a greater volume, resulting in bubble growth instead. These complex dynamics began to be discussed by Doremus (1960) in terms of mixed gas or multi-phase bubbles. Some initial modelling of gas exchanges was then carried out in the discussion of Pigeonneau (2011), but a

more comprehensive consideration of two-way diffusion, especially in the context of magmatic systems, is yet to be carried out.

8.2.6 Observations of Bubbles in Natural Melt

Throughout this thesis, extensions to experimental work on bubbles in high-viscosity fluids to melt samples from magmatic systems has been alluded to. To date, bubbles have rarely been observed directly in natural melts such as basalts or obsidian. Those studies that have been able to make observations relied on complex experimental processes to analyse situations before or after a process has taken place. This approach could be extended to try and observe non-reactive bubble rise in magmatic material as suggested in **section 4.3.2** to confirm hypotheses on the use of the Hadamard-Rybczynski equation to describe bubble motions. Furthermore, this type of indirect observation of a process could also be used to observe resorption of a single decoupled bubble in magmatic material using a similar technique.

A gold-standard for observations of bubbles in natural melts would be to directly observe processes as they take place. However, the complex properties of magmatic melts including inherent opaqueness, high temperature working viscosities and iridescence when heated provide particular complexity. Significant advances in experimental practices would be needed to complete such experimental work, if it is even possible at all. Nonetheless it provides an interesting topic for discussion in future work, which should always try to explore experimental options alongside numerical modelling to solve volcanological problems.

Bibliography

Allabar, A., Dobson, K., Bauer, C. and Nowak, M. (2020), 'Vesicle shrinkage in hydrous phonolitic melt during cooling', *Contributions to Mineralogy and Petrology* **175**(3), 1–19. https://doi.org/10.1007/s00410-020-1658-3.

Alletti, M., Baker, D. R. and Freda, C. (2007), 'Halogen diffusion in a basaltic melt', *Geochimica et Cosmochimica Acta* **71**(14), 3570–3580. https://doi.org/10.1016/j.gca.2007.04.018.

Altemose, V. O. (1961), 'Helium diffusion through glass', *Journal of Applied Physics* **32**(7), 1309–1316. https://doi.org/10.1063/1.1736226.

Annen, C., Pichavant, M., Bachmann, O. and Burgisser, A. (2008), 'Conditions for the growth of a long-lived shallow crustal magma chamber below Mount Pelée volcano (Martinique, Lesser Antilles Arc)', *Journal of Geophysical Research: Solid Earth* **113**(B7). https://doi.org/10.1029/2007JB005049.

Bachmann, O. and Bergantz, G. W. (2003), 'Rejuvenation of the Fish Canyon magma body: A window into the evolution of large-volume silicic magma systems', *Geology* **31**(9), 789–792. https://doi.org/10.1130/G19764.1.

Bachmann, O. and Bergantz, G. W. (2006), 'Gas percolation in upper-crustal silicic crystal mushes as a mechanism for upward heat advection and rejuvenation of near-solidus magma bodies', *Journal of Volcanology and Geothermal Research* **149**(1), 85–102. https://doi.org/10.1016/j.jvolgeores.2005.06.002.

Baker, D. R., Dalpé, C. and Poirier, G. (2004), 'The viscosities of foods as analogs for silicate melts', *Journal of Geoscience Education* **52**(4), 363–367. https://doi.org/10.5408/1089-9995-52.4.363.

Balcone-Boissard, H., Villemant, B. and Boudon, G. (2010), 'Behavior of halogens during the degassing of felsic magmas', *Geochemistry, Geophysics, Geosystems* **11**(9).

Bansal, N. P. and Doremus, R. H. (1986), *Handbook of Glass Properties*, Academic Press Inc., London, UK.

Beckett, F. M., Mader, H. M., Phillips, J. C., Rust, A. C. and Witham, F. (2011), 'An experimental study of low-reynolds-number exchange flow of two newtonian fluids in a vertical pipe', *Journal of Fluid Mechanics* **682**, 652–670. https://doi.org/10.1017/jfm.2011.264.

Beerkens, R. (2002), *Chapter 2.1 - Modelling of the melting process in industrial glass furnaces*, *in* Mathematical Simulation in Glass Technology, Springer, Berlin, Germany.

Beerkens, R. (2003), Analysis of advanced and fast fining processes for glass melts, *in* J. Varner, ed., 'Advances in fusion and processing of glass III : proceedings of the 7th International Conference on Advances in Fusion and Processing of Glass, July 27-31, 2003', Ceramic Transactions, American Ceramic Society, Rochester, New York, United States, pp. 1–53.

Behrens, H. and Gaillard, F. (2006), 'Geochemical Aspects of Melts: Volatiles and Redox Behavior', *Elements* **2**(5), 275–280. https://doi.org/10.2113/gselements.2.5.275.

Behrens, H., Misiti, V., Freda, C. and Vetere, F. (2009), 'Solubility of H_2O and CO_2 in ultrapotassic melts at 1200 and 1250°C and pressure from 50 to 500 MPa', *American Mineralogist* **94**, 105–120.

Behrens, H., Zhang, Y. and Xu, Z. (2004), 'H_2O diffusion in dacitic and andesitic melts', *Geochimica et Cosmochimica Acta* **68**(24), 5139–5150. https://doi.org/10.1016/j.gca.2004.07.008.

Bergantz, G. W. and Breidenthal, R. E. (2001), 'Non-stationary entrainment and tunneling eruptions: A dynamic link between eruption processes and magma mixing', *Geophysical Research Letters* **28**(16), 3075–3078. https://doi.org/10.1029/2001GL013304.

Berndt, J., Liebske, C., Holtz, F., Freise, M., Nowak, M., Ziegenbein, D., Hurkuck, W. and Koepke, J. (2002), 'A combined rapid-quench and h_2-membrane setup for internally heated pressure vessels: Description and application for water solubility in basaltic melts', *American Mineralogist* **87**(11-12), 1717–1726. https://doi.org/10.2138/am-2002-11-1222.

Blower, J., Mader, H. and Wilson, S. (2001), 'Coupling of viscous and diffusive controls on bubble growth during explosive volcanic eruptions', *Earth and Planetary Science Letters* **193**(1), 47–56. https://doi.org/10.1016/S0012-821X(01)00488-5.

Bottinga, Y. and Weill, D. F. (1972), 'The viscosity of magmatic silicate liquids: a model for calculation', *American Journal of Science* **272**, 438-475.

Brehens, H. (2010), 'Nobel gas diffusion in silicate glasses and melts', *Reviews in Mineralogy and Geochemistry* **72**(1), 227–267. https://doi.org/10.2138/rmg.2010.72.6.

Brune, S., Williams, S. E. and Müller, D. (2017), 'Potential links between continental rifting, CO_2 degassing and climate change through time', *Nature Geoscience* **10**, 941–946. https://doi.org/10.1038/s41561-017-0003-6.

Burgisser, A. and Degruyter, W. (2015), Chapter 11 - magma ascent and degassing at shallow levels, *in* H. Sigurdsson, ed., 'The Encyclopedia of Volcanoes', 2nd edn, Academic Press, Amsterdam, pp. 225–236. https://doi.org/10.1016/B978-0-12-385938-9.00011-0.

Burgisser, A. and Gardner, J. E. (2004), 'Experimental constraints on degassing and permeability in volcanic conduit flow', *Bulletin of Volcanology* **67**, 42–56. https://doi.org/10.1007/s00445-004-0359-5.

Cable, M. and Frade, J. R. (1986), Diffusion controlled growth and dissolution of spheres of finite initial size, *in* 'Kinetics Mass Transport in Silicate and Oxide Systems', Vol. 7 of *Materials Science Forum*, Trans Tech Publications Ltd, pp. 187–194. https://doi.org/10.4028/www.scientific.net/MSF.7.187.

Cadogan, S. P., Maitland, G. C. and Trusler, J. P. M. (2014), 'Diffusion coefficients of CO_2 and N_2 in water at temperatures between 298.15 K and 423.15 K at pressures up to 45 MPa', *Journal of Chemical & Engineering Data* **59**(2), 519–525. 10.1021/je401008s.

Carey, R. J., Manga, M., Degruyter, W., Gonnermann, H., Swanson, D., Houghton, B., Orr, T. and Patrick, M. (2013), 'Convection in a volcanic conduit recorded by bubbles', *Geology* **41**(4), 395–398. https://doi.org/10.1130/G33685.1.

Carroll, M. R. and Stolper, E. M. (1993), 'Noble gas solubilities in silicate melts and glasses: New experimental results for argon and the relationship between solubility and ionic porosity', *Geochimica et Cosmochimica Acta* **57**(23), 5039–5051. https://doi.org/10.1016/0016-7037(93)90606-W.

Castro, J. M., Bindeman, I. N., Tuffen, H. and Schipper, C. I. (2014), 'Explosive origin of silicic lava: textural and δD–H_2O evidence for pyroclastic degassing during rhyolite effusion', *Earth and Planetary Science Letters* **405**, 52–61. https://doi.org/10.1016/j.epsl.2014.08.012.

Castro, J. M., Burgisser, A., Schipper, C. I. and Mancini, S. (2012), 'Mechanisms of bubble coalescence in silicic magmas', *Bulletin of Volcanology* **74**(10), 2339–2352. https://doi.org/10.1007/s00445-012-0666-1.

Castro, J. M. and Gardner, J. E. (2008), 'Did magma ascent rate control the explosive-effusive transition at the Inyo volcanic chain, California?', *Geology* **36**(4), 279–282. 10.1130/G24453A.1.

Castruccio, A., Rust, A. and Sparks, R. (2010), 'Rheology and flow of crystal-bearing lavas: Insights from analogue gravity currents', *Earth and Planetary Science Letters* **297**(3), 471–480. https://doi.org/10.1016/j.epsl.2010.06.051.

Chernov, A., Pilnik, A., Davydov, M., Ermanyuk, E. and Pakhomov, M. (2018), 'Gas nucleus growth in high-viscosity liquid under strongly non-equilibrium conditions', *International Journal of Heat and Mass Transfer* **123**, 1101–1108. https://doi.org/10.1016/j.ijheatmasstransfer.2018.03.045.

Clift, R., Grace, J. and Weber, M. E. (2005), *Bubbles, Droplets and Particles*, Dover Publications, Inc., New York.

Colombier, M., Vasseur, J., Houghton, B. F., Cáceres, F., Scheu, B., Kueppers, U., Thivet, S., Gurioli, L., Montanaro, C., Soldati, A., Di Muro, A. and Dingwell, D. B. (2021), 'Degassing and gas percolation in basaltic magmas', *Earth and Planetary Science Letters* **573**, 117134.

Corliss, J. B., Baross, J. and Hoffman, S. (1981), 'An hypothesis concerning the relationships between submarine hot springs and the origin of life on Earth', *Oceanologica Acta Special Issue* . 26th lnternational Geological Congress: Geology of oceans symposium, Paris, 7-17 July 7-17.

Coumans, J. P., Llewellin, E. W., Wadsworth, F. B., Humphreys, M. C. S., Mathias, S. A., Yelverton, B. M. and Gardner, J. E. (2020), 'An experimentally validated numerical model for bubble growth in magma', *Journal of Volcanology and Geothermal Research* **402**, 107002. https://doi.org/10.1016/j.jvolgeores.2020.107002.

Cristalica (n.d.), 'Premium Studio Glass Datasheet'. Available at: https://glasscolor.com/media/wysiwyg/InfoSheet_Cristalica_Studio_Glass_COE100__Fahrenheit_.pdf.

Dasgupta, R. (2013), 'Ingassing, storage, and outgassing of terrestrial carbon through geologic time', *Reviews in Mineralogy and Geochemistry* **75**, 183–220.

Degruyter, W., Bachmann, O., Burgisser, A. and Manga, M. (2012), 'The effects of outgassing on the transition between effusive and explosive silicic eruptions', *Earth and Planetary Science Letters* **349-350**, 161–170.

Del Bello, E., Llewellin, E. W., Taddeucci, J., Scarlato, P. and Lane, S. J. (2012), 'An analytical model for gas overpressure in slug-driven explosions: Insights into Strombolian volcanic eruptions', *Journal of Geophysical Research: Solid Earth* **117**(B2). https://doi.org/10.1029/2011JB008747.

Dingwell, D. B. (1990), 'Effects of structural relaxation on cationic tracer diffusion in silicate melts', *Chemical Geology* **82**, 209–216. https://doi.org/10.1016/0009-2541(90)90082-I.

Dingwell, D. B. (1996), 'Volcanic dilemma: Flow or blow?', *Science* **273**(5278), 1054–1055. https://doi.org/10.1126/science.273.5278.1054.

Dingwell, D. B. (2006), 'Transport properties of magmas: Diffusion and rheology', *Elements* **2**(5), 281–286. 10.2113/gselements.2.5.281.

Dingwell, D. B. and Virgo, D. (1988), 'Viscosities of melts in the Na_2O-FeO-Fe_2O_3-SiO_2 system and factors controlling relative viscosities of fully polymerized silicate melts', *Geochimica et Cosmochimica Acta* **52**(2), 395–403.

Doremus, R. H. (1960), 'Diffusion of oxygen from contracting bubbles in molten glass', *Journal of the American Ceramic Society* **43**(12), 655–661.

Dungan, M. A., Bouvet de Maisonneuve, C., Burgisser, A., Bachmann, O. and Moreno, H. (2010), Pahoehoe lavas at arc volcanoes with >50% crystals. How and why?, *in* 'AGU Fall Meeting Abstracts', Vol. 2010, pp. V43B–2375. Provided by the SAO/NASA Astrophysics Data System. https://ui.adsabs.harvard.edu/abs/2010AGUFM.V43B2375D.

Edmonds, M. and Herd, R. A. (2007), 'A volcanic degassing event at the explosive-effusive transition', *Geophysical Research Letters* **34**(21). https://doi.org/10.1029/2007GL031379.

Edmonds, M. and Wallace, P. J. (2017), 'Volatiles and Exsolved Vapor in Volcanic Systems', *Elements* **13**(1), 29–34.

Eichelberger, J., Carrigan, C., Westrich, H. and Price, R. (1986), 'Non-explosive silicic volcanism', *Nature* **323**(6089), 598–602. https://doi.org/10.1038/323598a0.

Engineering Tool Box (n.d.), 'Solubility of gases in water vs. temperature'. Accessed 17 January 2022.
URL: *https://www.engineeringtoolbox.com/gases-solubility-water-d_1148.html*

Fink, J. H., Anderson, S. W. and Manley, C. R. (1992), 'Textural constraints on effusive silicic volcanism: Beyond the permeable foam model', *Journal of Geophysical Research: Solid Earth* **97**(B6), 9073–9083. https://doi.org/10.1029/92JB00416.

Fischer, T. P., Arellano, S., Carn, S., Aiuppa, A., Galle, B., Allard, P., Lopez, T., Shinohara, H., Kelly, P., Werner, C., Cardellini, C. and G, C. (2019), 'The emissions of CO_2 and other volatiles from the world's subaerial volcanoes', *Scientific Reports* **9**(18716). https://doi.org/10.1038/s41598-019-54682-1.

Fogel, R. A. and Rutherford, M. J. (1990), 'The solubility of carbon dioxide in rhyolitic melts; a quantitative FTIR study', *American Mineralogist* **75**(11-12), 1311–1326.

Friedman, I. (1989), 'Are extrusive rhyolites produced from permeable foam eruptions?', *Bulletin Volcanology* **51**, 69–71. https://doi.org/10.1007/BF01086762.

Fulcher, G. (1925), 'Analysis of recent measurements of the viscosity of glasses', *Journal of the American Ceramic Society* **8**(6), 339–355.

Gamsjäger, H., Lorimer, J. W., Salomon, M., Shaw, D. G. and Tomkins, R. P. T. (2010), 'The iupac-nist solubility data series: A guide to preparation and use of compilations and evaluations (iupac technical report)', *Pure and Applied Chemistry* **82**(5), 1137–1159. https://doi.org/10.1351/PAC-REP-09-10-33.

Gardner, J. E., Hilton, M. and Carroll, M. R. (1999), 'Experimental constraints on degassing of magma: isothermal bubble growth during continuous decompression from high pressure', *Earth and Planetary Science Letters* **168**(1), 201–218. https://doi.org/10.1016/S0012-821X(99)00051-5.

Gardner, J. E., Llewellin, E. W., Watkins, J. M. and Befus, K. S. (2017), 'Formation of obsidian pyroclasts by sintering of ash particles in the volcanic conduit', *Earth and Planetary Science Letters* **459**, 252–263. https://doi.org/10.1016/j.epsl.2016.11.037.

Gardner, J., Wadsworth, F., Llewellin, E., Watkins, J. and Coumans, J. (2019), 'Experimental constraints on the textures and origin of obsidian pyroclasts', *Bulletin of Volcanology* **81**, 22. https://doi.org/10.1007/s00445-019-1283-z.

Giordano, D. and Dingwell, D. (2003), 'Viscosity of hydrous etna basalt: implications for plinian-style basaltic eruptions', *Bulletin of Volcanology* **65**, 8–14. https://doi.org/10.1007/s00445-002-0233-2.

Giordano, D., Russell, J. K. and Dingwell, D. B. (2008), 'Viscosity of magmatic liquids: A model', *Earth and Planetary Science Letters* **271**(1), 123–134. https://doi.org/10.1016/j.epsl.2008.03.038.

Glasstone, S., Laidler, K. and Eyring, H. (1941), *The Theory of Rate Process*, McGraw-Hill, New York.

Gonnermann, H. M. and Manga, M. (2007), 'The fluid mechanics inside a volcano', *Annual Review of Fluid Mechanics* **39**(1), 321–356. https://doi.org/10.1146/annurev.fluid.39.050905.110207.

Gonnermann, H. M. and Manga, M. (2013), *Chapter 4: Dynamics of magma ascent in the volcanic conduit*, *in* Fagents, S.A, Gregg, T.K.P. Lopes, R.M.C., eds, Modelling Volcanic Processes: The physics and mathematics of volcanism, Cambridge University Press, Cambridge, UK. https://doi.org/10.1017/CBO9781139021562.004.

Gottsmann, J., Giordano, D. and Dingwell, D. B. (2002), 'Predicting shear viscosity during volcanic processes at the glass transition: a calorimetric calibration', *Earth and Planetary Science Letters* **198**, 417–427. https://doi.org/https://doi.org/10.1016/S0012-821X(02)00522-8.

Greene, C. H. and Gaffney, R. F. (1959), 'Apparatus for measuring rate of absorption of a bubble in glass', *Journal of the American Ceramic Society* **42**(6), 271–275.

Greene, C. H. and Kitano, I. (1959), 'Rate of solution of oxygen bubbles in commercial glasses', *Glastechnische Berichte* **32**(5), 44–48.

Greenland, L. P., Rose, W. I. and Stokes, J. B. (1985), 'An estimate of gas emissions and magmatic gas content from kilauea volcano', *Geochimica et Cosmochimica Acta* **49**(1), 125–129. https://doi.org/10.1016/0016-7037(85)90196-6.

Hadamard, J. S. (1911), 'Mouvement permanent lent d'une sphere liquide et visqueuse dans un liquid visqueux', *Comptes Rendus de l'Académie des Sciences (in French)* **152**(1735).

Halmer, M. M., Schmincke, H.-U. and Graf, H.-F. (2002), 'The annual volcanic gas input into the atmosphere, in particular into the stratosphere: a global data set for the past 100 years', *Journal of Volcanology and Geothermal Research* **115**(3), 511–528. https://doi.org/10.1016/S0377-0273(01)00318-3.

Hamada, M., Laporte, D., Cluzel, N., Koga, K. and Kawamoto, T. (2010), 'Simulating bubble number density of rhyolitic pumices from Plinian eruptions: constraints from fast decompression experiments', **72**, 735–746. https://doi.org/10.1007/s00445-010-0353-z.

Harris, A. J. L. (2008), 'Modeling lava lake heat loss, rheology, and convection', *Geophysical Research Letters* **35**(7). https://doi.org/10.1029/2008GL033190.

Henderson, G. S., Calas, G. and Stebbins, J. F. (2006), 'The structure of silicate glasses and melts', *Elements* **2**, 269–273.

Henderson, P., Nolan, J., Cunningham, G. and Lowry, R. (1985), 'Structural controls and mechanisms of diffusion in natural silicate melts', *Contributions to Mineralogy and Petrology* **89**, 263–272. https://doi.org/10.1007/BF00379459.

Hess, K.-U. and Dingwell, D. (1996), 'Viscosities of hydrous leucogranitic melts: A non-Arrhenian model', *American Mineralogist* **81**(9-10), 1297–1300.

Holtz, F., Behrens, H., Dingwell, D. B. and Johannes, W. (1995), 'H_2O solubility in haplogranitic melts: Compositional, pressure, and temperature dependence', *American Mineralogist* **80**(1-2), 94–108. https://doi.org/10.2138/am-1995-1-210.

Holtz, F., Behrens, H., Dingwell, D. B. and Taylor, R. P. (1992), 'Water solubility in aluminosilicate melts of haplogranite composition at 2 kbar', *Chemical Geology* **96**(3), 289–302. https://doi.org/10.1016/0009-2541(92)90060-I.

Hornyak, E. J. and Weinberg, M. C. (1984), 'Velocity of a freely rising gas bubble in a soda-lime silicate glass melt', *Journal of the American Ceramic Society* **67**(11), 244–246. https://doi.org/10.1111/j.1151-2916.1984.tb19498.x.

Huang, Z., Su, M., Yang, Q., Li, Z., Chen, S., Li, Y., Zhou, X., Li, F. and Song, Y. (2017), 'A general patterning approach by manipulating the evolution of two-dimensional liquid foams', *Nature Communications* **8**(14110). https://doi.org/10.1038/ncomms14110.

Huber, C., Su, Y., Nguyen, C. T., Parmigiani, A., Gonnermann, H. M. and Dufek, J. (2014), 'A new bubble dynamics model to study bubble growth, deformation, and coalescence', *Journal of Geophysical Research: Solid Earth* **119**(1), 216–239. https://doi.org/10.1002/2013JB010419.

Iacovino, K. and Gouard, C. (2021), 'TAS diagram plotter (3.0)'. https://doi.org/10.5281/zenodo.5907859.

Ishii, K., Yokoo, A., Kagiyama, T., Ohkura, T., Yoshikawa, S. and Inoue, H. (2019), 'Gas flow dynamics in the conduit of strombolian explosions inferred from seismo-acoustic observations at aso volcano, japan', *Earth, Planets and Space* **71**(13). https://doi.org/10.1186/s40623-019-0992-z.

Jackson, L. E., Wadsworth, F. B., Mitchell, J., Rennie, C., Llewellin, E. W., Hess, K.-U. and Dingwell, D. B. (2022), 'Bubble rise in molten glasses and silicate melts during heating and cooling cycles', *Journal of the American Ceramic Society* pp. 1–16. https://doi.org/10.1111/jace.18680.

Jambon, A., Weber, H. and Braun, O. (1986), 'Solubility of He, Ne, Ar, Kr and Xe in a basalt melt in the range 1250–1600°C. geochemical implications', *Geochimica et Cosmochimica Acta* **50**(3), 401–408. https://doi.org/10.1016/0016-7037(86)90193-6.

Jaupart, C. and Vergniolle, S. (1988), 'Laboratory models of Hawaiian and Strombolian eruptions', *Nature* **331**, 58–60. https://doi.org/10.1038/331058a0.

Jucha, R. B., Powers, D., McNeil, T., Subramanian, R. S. and Cole, R. (1982), 'Bubble rise in glassmelts', *Journal of the American Ceramic Society* **65**(6), 289–292. https://doi.org/10.1111/j.1151-2916.1982.tb10446.x.

Kavanagh, J. L., Engwell, S. L. and Martin, S. A. (2018), 'A review of laboratory and numerical modelling in volcanology', *Solid Earth* **9**(2), 531–571. https://doi.org/10.5194/se-9-531-2018.

Kilbride, B., Edmonds, M. and Biggs, J. (2016), 'Observing eruptions of gas-rich compressible magmas from space', *Nature Communications* **7**(13744). https://doi.org/10.1038/ncomms13744.

Kloužek, J. and Němec, L. (2003), 'Modelling of glass refining kinetics; Part 2. bubble distribution models and methods of measurement of refining properties', *Ceramics Silikáty* **47**(4), 155–161.

Lautze, N. C., Sisson, T., Mangan, M. and Grove, T. (2011), 'Segregating gas from melt: an experimental study of the ostwald ripening of vapor bubbles in magmas', *Contributions to Mineralogy and Petrology* **161**, 331–347. https://doi.org/10.1007/s00410-010-0535-x.

Lensky, N., Navon, O. and Lyakhovsky, V. (2004), 'Bubble growth during decompression of magma: Experimental and theoretical investigation', *Journal of Volcanology and Geothermal Research* **129**(1), 7–22. https://doi.org/10.1016/S0377-0273(03)00229-4.

Lesher, C. E. and Spera, F. J. (2015), Chapter 5 - thermodynamic and transport properties of silicate melts and magma, *in* H. Sigurdsson, ed., 'The Encyclopedia of Volcanoes', 2nd edn, Academic Press, Amsterdam, pp. 113–141. https://doi.org/10.1016/B978-0-12-385938-9.00005-5.

Lesne, P., Scaillet, B., Pichavant, M., Iacono-Marziano, G. and Beny, J.-M. (2011), 'The h$_2$o solubility of alkali basaltic melts: an experimental study', *Contributions to Mineralogy and Petrology* **162**, 133–151. https://doi.org/10.1007/s00410-010-0588-x.

Levich, V. G. (1962), *Physicochemical Hydrodynamics*, Prentice-Hall, Englewood Cliffs, New Jersey.

Li, K.-W. K. and Schneider, A. (1993), 'Rise velocities of large bubbles in viscous newtonian liquids', *Journal of the American Ceramic Society* **76**(1), 241–244. https://doi.org/10.1111/j.1151-2916.1993.tb03717.x.

Liu, Y. and Zhang, Y. (2000), 'Bubble growth in rhyolitic melt', *Earth and Planetary Science Letters* **181**(1), 251–264. https://doi.org/10.1016/S0012-821X(00)00197-7.

Liu, Y., Zhang, Y. and Behrens, H. (2005), 'Solubility of H_2O in rhyolitic melts at low pressures and a new empirical model for mixed H_2O–CO_2 solubility in rhyolitic melts', *Journal of Volcanology and Geothermal Research* **143**(1), 219–235. https://doi.org/10.1016/j.jvolgeores.2004.09.019.

Llewellin, E. W., Mader, H. M. and Wilson, S. D. R. (2002), 'The rheology of a bubbly liquid', *Proceedings of the Royal Society of London. Series A: Mathematical, Physical and Engineering Sciences* **458**(2020), 987–1016. https://doi.org/10.1098/rspa.2001.0924.

Lv, J., Ren, K. and Chen, Y. (2018), 'CO_2 diffusion in various carbonated beverages: A molecular dynamics study', *The Journal of Physical Chemistry B* **122**(5), 1655–1661. 10.1021/acs.jpcb.7b10469.

Mader, H. M., Llewellin, E. W. and Mueller, S. P. (2013), 'The rheology of two-phase magmas: A review and analysis', *Journal of Volcanology and Geothermal Research* **257**, 135–158. https://doi.org/10.1016/j.jvolgeores.2013.02.014.

Manga, M. and Stone, H. A. (1995), 'Low reynolds number motion of bubbles, drops and rigid spheres through fluid–fluid interfaces', *Journal of Fluid Mechanics* **287**, 279–298. https://doi.org/10.1017/S0022112095000954.

Manley, C. R. and Fink, J. H. (1987), 'Internal textures of rhyolite flows as revealed by research drilling', *Geology* **15**(6), 549–552. https://doi.org/10.1130/0091-7613(1987)15<549:ITORFA>2.0.CO;2.

Markworth, A. J. (1985), 'Comments on foam stability, ostwald ripening, and grain growth', *Journal of Colloid and Interface Science* **107**(2), 569–571. https://doi.org/10.1016/0021-9797(85)90211-5.

Martin, W., Baross, J., Kelley, D. and Russell, M. J. (2008), 'Hydrothermal vents and the origin of life', *Nature Reviews Microbiology* **6**, 805–814. https://doi.org/10.1038/nrmicro1991.

Mathieu, L., van Wyk de Vries, B., Holohan, E. P. and Troll, V. R. (2008), 'Dykes, cups, saucers and sills: Analogue experiments on magma intrusion into brittle rocks', *Earth and Planetary Science Letters* **271**(1), 1–13. https://doi.org/10.1016/j.epsl.2008.02.020.

McIntosh, I. M. (2013), Bubble growth and resorption in magma: insights from dissolved water distributions in volcanic glass, PhD thesis, Durham University. Available at Durham E-Theses Online: http://etheses.dur.ac.uk/8505/.

McIntosh, I. M., Llewellin, E. W., Humphreys, M. C. S., Nichols, A. R. L., Burgisser, A., Schipper, C. I. and Larsen, J. F. (2014), 'Distribution of dissolved water in magmatic glass records growth and resorption of bubbles', *Earth and Planetary Science Letters* **401**, 1–11. https://doi.org/10.1016/j.epsl.2014.05.037.

Mittal, T. and Richards, M. A. (2019), 'Volatile degassing from magma chambers as a control on volcanic eruptions', *Journal of Geophysical Research: Solid Earth* **124**(8), 7869–7901. https://doi.org/10.1029/2018JB016983.

Mostinsky, I. L. (2011), 'Diffusion coefficient'. Accessed 7 January 2022.
URL: *https://www.thermopedia.com/content/696/*

Mourtada-Bonnefoi, C. C. and Laporte, D. (1999), 'Experimental study of homogeneous bubble nucleation in rhyolitic magmas', *Geophysical Research Letters* **26**(23), 3505–3508.

Mueller, S., Llewellin, E. and Mader, H. (2011), 'The effect of particle shape on suspension viscosity and implications for magmatic flows', *Geophysical Research Letters* **38**. https://doi.org/10.1029/2011GL047167.

Mysen, B. O. (1983), 'The structure of silicate melts', *Annual Review of Earth and Planetary Sciences* **11**, 75–97.

National Academies of Sciences, Engineering and Medicine (2017), *Volcanic Eruptions and Their Response, Unrest, Precursors, and Timing*, The National Academies Press, Washington, DC. https://doi.org/10.17226/24650.

Navon, O., Chekhmir, A. and Lyakhovsky, V. (1998), 'Bubble growth in highly viscous melts: theory, experiments, and autoexplosivity of dome lavas', *Earth and Planetary Science Letters* **160**(3), 763–776. https://doi.org/10.1016/S0012-821X(98)00126-5.

Newman, S. and Lowenstern, J. B. (2002), 'Volatilecalc: a silicate melt–h2o–co2 solution model written in visual basic for excel', *Computers Geosciences* **28**(5), 597–604. https://doi.org/10.1016/S0098-3004(01)00081-4.

Oishi, Y., Terai, R. and Ueda, H. (1975), *Oxygen Diffusion in Liquid Silicates and Relation to their Viscosity*, Springer US, Boston, MA, pp. 297–310. https://doi.org/10.1007/978-1-4684-3150-6_20.

Oppenheimer, C., Scaillet, B., Woods, A., Sutton, A., Elias, T. and Moussallam, Y. (2018), 'Influence of eruptive style on volcanic gas emission chemistry and temperature', *Nature Geoscienc* **11**(9), 678–681. https://doi.org/10.1038/s41561-018-0194-5.

Ostwald, W. (1896), *Lehrbuch der Allgemeinen Chemie*, Vol. 2, W. Engelmann, Leipzig, Germany.

Pallister, J. S., Cashman, K. V., Hagstrum, J. T., Beeler, N. M., Moran, S. C. and Denlinger, R. P. (2013), 'Faulting within the Mount St. Helens conduit and implications for volcanic earthquakes', *GSA Bulletin* **125**(3-4), 359–376. https://doi.org/10.1130/B30716.1.

Pan, V., Holloway, J. R. and Hervig, R. L. (1991), 'The pressure and temperature dependence of carbon dioxide solubility in tholeiitic basalt melts', *Geochimica et Cosmochimica Acta* **55**(6), 1587–1595. https://doi.org/10.1016/0016-7037(91)90130-W.

Patankar, S. (1980), *Numerical Heat Trasfer and Fluid Flow*, McGraw-Hill, New York.

Patrick, M. R., Orr, T. R., Swanson, D. A., Elias, T. and Shiro, B. (2018), *Lava lake activity at the summit of Kilauea Volcano*, *in* 2016: U.S. Geological Survey Scientific Investigations Report 2018–5008. https://doi.org/10.3133/sir20185008.

Pereira, L., Kloužek, J., Vernerová, M., Laplace, A. and Pigeonneau, F. (2020), 'Experimental and numerical investigations of an oxygen single-bubble shrinkage in a borosilicate glass-forming liquid doped with cerium oxide', *Journal of the American Ceramic Society* **103**(12), 6736–6745. https://doi.org/10.1111/jace.17398.

Pigeonneau, F. (2007), 'Coupled modelling of redox reactions and glass melt fining processes', *Glass Technology - European Journal of Glass Science and Technology Part A* **48**, 66–72. https://hal.archives-ouvertes.fr/hal-01442935.

Pigeonneau, F. (2009), 'Mass transfer of a rising bubble in molten glass with instantaneous oxidation-reduction reaction', *Chemical Engineering Science* **64**(13), 3120–3129.

Pigeonneau, F. (2011), 'Mechanism of mass transfer between a bubble initially composed of oxygen and molten glass', *International Journal of Heat and Mass Transfer* **54**(7-8), 1448–1455.

Pigeonneau, F., Martin, D. and Mario, O. (2010), 'Shrinkage of an oxygen bubble rising in a molten glass', *Chemical Engineering Science* **65**(10), 3158–3168. https://doi.org/10.1016/j.ces.2010.02.003.

Poppe, S., Holohan, E. P., Galland, O., Buls, N., Van Gompel, G., Keelson, B., Tournigand, P.-Y., Brancart, J., Hollis, D., Nila, A. and Kervyn, M. (2019), 'An inside perspective on magma intrusion: Quantifying 3D displacement and strain in laboratory experiments by dynamic X-Ray computed tomography', *Frontiers in Earth Science* **7**. https://doi.org/10.3389/feart.2019.00062.

Prousevitch, A. A., Sahagian, D. L. and Anderson, A. T. (1993), 'Dynamics of diffusive bubble growth in magmas: Isothermal case', *Journal of Geophysical Research: Solid Earth* **98**(B12), 22283–22307. https://doi.org/10.1029/93JB02027.

Ramos, J. I. (1986), 'Behavior of multicomponent gas bubbles in glass melts', *Journal of the American Ceramic Society* **69**(2), 149–154. https://doi.org/10.1111/j.1151-2916.1986.tb04720.x.

Roselieb, K., Büttner, H., Eicke, U., Köhler, U. and Rosenhauer, M. (1996), 'Pressure dependence of Ar and Kr diffusion in a jadeite melt', *Chemical Geology* **128**(1), 207–216. https://doi.org/10.1016/0009-2541(95)00174-3.

Rossi, S., Petrelli, M., Morgavi, D., Vetere, F. P., Almeev, R. R., Astbury, R. L. and Perugini, D. (2019), 'Role of magma mixing in the pre-eruptive dynamics of the Aeolian Islands volcanoes (Southern Tyrrhenian Sea, Italy)', *Lithos* **324-325**, 165–179. https://doi.org/10.1016/j.lithos.2018.11.004.

Ryan, A. G., Russell, J. K., Nichols, A. R. L., Hess, K.-U. and Porritt, L. A. (2015), 'Experiments and models on H_2O retrograde solubility in volcanic systems', *American Mineralogist* **100**(4), 774–786. https://doi.org/10.2138/am-2015-5030.

Rybczynski, W. (1911), 'Über die fortschreitende bewegung einer flüssigen kugel in einem zähen medium', *Bulletin International de l'Académie des sciences de Cracovie (in German)* **40-46**.

Schaeffer, H. A. (1984), 'Diffusion-controlled processes in glass forming melts', *Journal of Non-Crystalline Solids* **67**(1), 19–33. https://doi.org/10.1016/0022-3093(84)90138-8.

Schellart, W. (2011), 'Rheology and density of glucose syrup and honey: Determining their suitability for usage in analogue and fluid dynamic models of geological processes', *Journal of Structural Geology* **33**(6), 1079–1088. https://doi.org/10.1016/j.jsg.2011.03.013.

Schmidt, B. C. and Keppler, H. (2002), 'Experimental evidence for high noble gas solubilities in silicate melts under mantle pressures', *Earth and Planetary Science Letters* **195**(3), 277–290. https://doi.org/10.1016/S0012-821X(01)00584-2.

Scholze, H. and Mulfinger, H.-O. (1959), *Journal of the German Society of Glass Technology* **32**, 381. .

Shea, T., Gurioli, L. and Houghton, B. (2012), 'Transitions between fall phases and pyroclastic density currents during the AD 79 eruption at Vesuvius: building a transient conduit model from the textural and volatile record', *Bulletin of Volcanology* **74**, 2363–2381. https://doi.org/10.1007/s00445-012-0668-z.

Shelby, J. (1973), *Journal of the American Ceramic Society* **56**, 263. .

Sides, I., Edmonds, M., Maclennan, J., Houghton, B. F., Swanson, D. A. and Steele-MacInnis, M. J. (2014), 'Magma mixing and high fountaining during the 1959 Kīlauea Iki eruption, Hawai'i', *Earth and Planetary Science Letters* **400**, 102–112. https://doi.org/10.1016/j.epsl.2014.05.024.

Silver, L., Ihinger, P. and Stolper, E. (1990), 'The influence of bulk composition on the speciation of water in silicate glasses', *Contributions to Mineralogy and Petrology* **104**, 142–162. https://doi.org/10.1007/BF00306439.

Sparks, R. S. J. (1978), 'The dynamics of bubble formation and growth in magmas: A review and analysis', *Journal of Volcanology and Geothermal Research* **3**(1), 1–37. https://doi.org/10.1016/0377-0273(78)90002-1.

Sparks, R. S. J. (2003), 'Dynamics of magma degassing', *Geological Society, London, Special Publications* **213**(1), 5–22. https://doi.org/10.1144/GSL.SP.2003.213.01.02.

Sparks, R. S. J., Tais, S. R. and Yanev, Y. (1999), 'Dense welding caused by volatile resorption', *Journal of the Geological Society* **156**(2), 217–225.

Spina, L., Cimarelli, C., Scheu, B., Di Genova, D. and Dingwell, D. B. (2016b), 'On the slow decompressive response of volatile- and crystal-bearing magmas: An analogue experimental investigation', *Earth and Planetary Science Letters* **433**, 44–53. https://doi.org/10.1016/j.epsl.2015.10.029.

Srinivasan, R., Gerth, W. and Powell, M. (2003), 'Mathematical model of diffusion-limited evolution of multiple gas bubbles in tissue', *Annals of Biomedical Engineering* **31**, 471–481. https://doi.org/10.1114/1.1561288.

Stevenson, D. and Blake, S. (1998), 'Modelling the dynamics and thermodynamics of volcanic degassing', *Bulletin of Volcanology* **60**, 307–317. https://doi.org/10.1007/s004450050234.

Stevenson, P. (2010), 'Inter-bubble gas diffusion in liquid foam', *Current Opinion in Colloid Interface Science* **15**(5), 374–381. https://doi.org/10.1016/j.cocis.2010.05.010.

Swanson, D. A., Rose, T. R., Mucek, A. E., Garcia, M. O., Fiske, R. S. and Mastin, L. G. (2014), 'Cycles of explosive and effusive eruptions at Kīlauea Volcano, Hawai'i', *Geology* **42**(7), 631–634. https://doi.org/10.1130/G35701.1.

Tammann, G. and Hesse, W. (1926), 'Die abhängigkeit der viscosität von der temperatur bie unterkühlten flüssigkeiten', *Zeitschrift für anorganische und allgemeine Chemie (in German)* **156**(1), 245–257.

Terai, R. and Oishi, Y. (1977), 'Self-diffusion of oxygen in soda-lime silicate glass', *Glastechnische Berichte* **50**(4), 68–73.

Truby, J. M., Mueller, S. P., Llewellin, E. W. and Mader, H. M. (2015), 'The rheology of three-phase suspensions at low bubble capillary number', *Proceedings of the Royal Society A: Mathematical, Physical and Engineering Sciences* **471**(2173). 10.1098/rspa.2014.0557.

USGS (2018), 'Volcanos can affect climate'. Viewed 15 December 2021.
URL: *https://www.usgs.gov/programs/VHP/volcanoes-can-affect-climate*

USGS (2019), 'Volcanic gases can be harmful to health, vegetation and infrastructure'. Accessed 15 December 2021.
URL: *https://www.usgs.gov/programs/VHP/volcanic-gases-can-be-harmful-health-vegetation-and-infrastructure*

Valade, S., Ripepe, M., Giuffrida, G., Karume, K. and Tedesco, D. (2018), 'Dynamics of mount nyiragongo lava lake inferred from thermal imaging and infrasound array', *Earth and Planetary Science Letters* **500**, 192–204.

Vazquez Una, G., Chenlo Romero, F., Pereira Goncalves, G. and Peaguda Lorenzo, J. (1994), 'Solubility of CO_2 in aqueous solutions of saccharose, glucose, fructose, and glycerin', *Journal of Chemical and Engineering Data* **39**(4), 639–642. https://doi.org/10.1021/je00016a002.

Vergniolle, S. and Jaupart, C. (1990), 'Dynamics of degassing at Kilauea volcano, Hawaii', *Journal of Geophysical Research: Solid Earth* **95**(B3), 2793–2809. https://doi.org/10.1029/JB095iB03p02793.

Vogel, H. (1921), 'Das temperaturabhaengigkeitsgesetz der viskositaet von fluessigkeiten', *Physikalische Zeitschrift (in German)* **22**, 645.

Voight, B., Widiwijayanti, C., Mattioli, G., Elsworth, D., Hidayat, D. and Strutt, M. (2010), 'Magma-sponge hypothesis and stratovolcanoes: Case for a compressible reservoir and quasi-steady deep influx at Soufriére hills volcano, montserrat', *Geophysical Research Letters* **37**(19). https://doi.org/10.1029/2009GL041732.

von Aulock, F. W., Kennedy, B. M., Maksimenko, A., Wadsworth, F. B. and Lavallée, Y. (2017), 'Outgassing from open and closed magma foams', *Frontiers in Earth Science* **5**. 10.3389/feart.2017.00046.

Wadsworth, F. B., Llewellin, E. W., Vasseur, J., Gardner, J. E. and Tuffen, H. (2020), 'Explosive-effusive volcanic eruption transitions caused by sintering', *Science Advances* **6**(39). 10.1126/sciadv.aba7940.

Wadsworth, F., Llewellin, E., Rennie, C., Watkinson, C., Mitchell, J., Vasseur, J., Mackie, A., Mackie, F., Carr, A., Schmiedel, T., Witcher, T., Soldati, A., Jackson, L., Foster, A., Hess, K.-U., Dingwell, D. and Hand, R. (2022), 'Using obsidian in glass art practice', *Volcanica* **5**(1), 183–207. https://doi.org/10.30909/vol.05.01.183207.

Wallace, P. J. and Anderson, A. T. (1999), *Volatiles in Magmas*, *in* Sigurdsson, H., Houghton, B., Rymer, H., Stix, J. and McNutt, S. eds, Encyclopedia of Volcanoes, Part I, 1st edn, Academic Press. Accessed at http://www.geo.mtu.edu/EHaz/ConvergentPlatesClass/wallace/Wallace%20&%20Anderson%20%281999%29.pdf 8 March 2022.

Watkins, J. M., Manga, M. and DePaolo, D. J. (2012), 'Bubble geobarometry: A record of pressure changes, degassing, and regassing at Mono Craters, California', *Geology* **40**(8), 699–702. http://doi.org/10.1130/G33027.1.

Watson, B. E. (1991), 'Diffusion of dissolved co_2 and cl in hydrous silicic to intermediate magmas', *Geochimica et Cosmochimica Acta* **55**(7), 1897–1902. https://doi.org/10.1016/0016-7037(91)90031-Y.

Watson, E. B., Sneeringer, M. A. and Ross, A. (1982), 'Diffusion of dissolved carbonate in magmas: Experimental results and applications', *Earth and Planetary Science Letters* **61**(2), 346–358. https://doi.org/10.1016/0012-821X(82)90065-6.

Weaver, J., Lavallée, Y., Ashraf, M., Kendrick, J. E., Lamur, A., Schauroth, J. and Wadsworth, F. B. (2022), 'Vesiculation and densification of pyroclasts: A clast-size dependent competition between bubble growth and diffusive outgassing', *Journal of Volcanology and Geothermal Research* **428**. https://doi.org/10.1016/j.jvolgeores.2022.107550.

Westrich, H. and Eichelberger, J. (1994), 'Gas transport and bubble collapse in rhyolitic magma: an experimental approach', *Bulletin of Volcanology* **56**, 447–458. https://doi.org/10.1007/BF00302826.

Wiesmaier, S., Morgavi, D., Renggli, C. J., Perugini, D., De Campos, C. P., Hess, K.-U., Ertel-Ingrisch, W., Lavallée, Y. and Dingwell, D. B. (2015), 'Magma mixing enhanced by bubble segregation', *Solid Earth* **6**(3), 1007–1023. https://doi.org/10.5194/se-6-1007-2015.

Woods, A. W. and Koyaguchi, T. (1994), 'Transitions between explosive and effusive eruption of silicic magmas', *Nature* **370**, 631–645. https://doi.org/10.1038/370641a0.

Yoshimura, S. and Nakamura, M. (2008), 'Diffusive dehydration and bubble resorption during open-system degassing of rhyolitic melts', *Journal of Volcanology and Geothermal Research* **178**(1), 72–80. https://doi.org/10.1016/j.jvolgeores.2008.01.017.

Yoshimura, S. and Nakamura, M. (2010), 'Chemically driven growth and resorption of bubbles in a multivolatile magmatic system', *Chemical Geology* **276**(1), 18–28.

Zhang, Y. (1999), 'H_2o in rhyolitic glasses and melts: Measurement, speciation, solubility, and diffusion', *Reviews of Geophysics* **37**(4), 493–516. https://doi.org/10.1029/1999RG900012.

Zhang, Y. (2010), 'Diffusion in Minerals and Melts: Theoretical Background', *Reviews in Mineralogy and Geochemistry* **72**(1), 5–59. https://doi.org/10.2138/rmg.2010.72.2.

Zhang, Y., Xu, Z., Zhu, M. and Wang, H. (2007), 'Silicate melt properties and volcanic eruptions', *Reviews of Geophysics* **45**(4). https://doi.org/10.1029/2006RG000216.

Žlutický, J. and Němec, L. (1977), 'Monitoring of the refining process in glass melts during melting', *Glastechnische Berichte* **50**(3), 57–61.

Appendices

Appendix I - Glass & Analogue Datasets

Table of references for datasets used in **Chapter 2.3** to demonstrate the properties of magmatic melts and analogue materials. *Reference number* refers to the indexed number on the figure legends, and *Citation* gives a reference for the data source.

Reference N$^{o.}$	Citation
1	Ryan et al. (2015)
2	Liu et al. (2005)
3	Silver et al. (1990)
4	Holtz et al. (1992, 1995)
5	Berndt et al. (2002)
6	Lesne et al. (2011)
7	Fogel and Rutherford (1990)
8	Pan et al. (1991)
9	Carroll and Stolper (1993)
10	Schmidt and Keppler (2002)
11	Brehens (2010)
12	Roselieb et al. (1996)
13	Zhang (1999)
14	Liu et al. (2005)
15	Behrens et al. (2004)
16	Alletti et al. (2007)
17	Balcone-Boissard et al. (2010)
18	Watson (1991)
19	Watson et al. (1982)
20	Cristalica (n.d.)
21	Jackson et al. (2022)
22	Altemose (1961)
23	Terai and Oishi (1977)
24	Scholze and Mulfinger (1959)
25	Shelby (1973)
26	Schellart (2011)
27	Beckett et al. (2011)

Appendix II - Derivation of the Diffusive Lengthscale λ_D

A full derivation showing the origins of the expression for diffusive lengthscale L in **Equation 2.11**, which is then subsequently used in the definitions of both stationary and buoyant Péclet numbers, Pe_b and Pe_s.

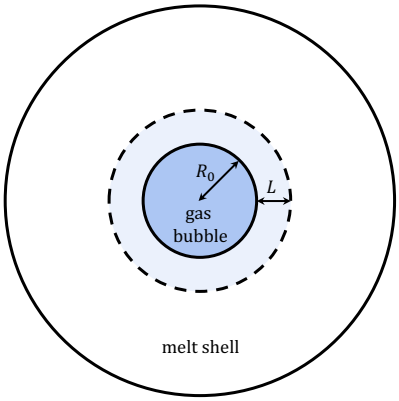

Considering a bubble with initial radius R_0, containing a fixed mass of ideal gas m_b, surrounded by a viscous melt shell into which this mass can transfer diffusively. The initial moles of gas in the bubble n, can be expressed as,

$$n = \frac{m_b}{M_m} = \frac{4}{3}\frac{\pi R_0^3 p_0}{R_g T}$$

where M_m is the molar mass of the gas, R_g the ideal gas constant and p_0 and T the pressure and temperature of the system respectively.

The mass of melt in the surrounding shell required to completely accommodate all of the mass from the gas bubble m_s can be found from the initial solubility of the melt, S_0,

$$m_a = \frac{100}{S_0} m_b$$

where S_0 is in wt.% at the conditions of p_0 and T. The volume of this melt mass, V_m depends on its density ρ_m.

$$V_m = \frac{m_s}{\rho_m}$$

From here, the diffusive lengthscale L, otherwise thought of as the distance the diffusive gas moves into the surrounding melt shell by diffusion, can be expressed as the ratio of melt volume to surface area of the spherical bubble.

$$L = \frac{V_m}{4\pi R_0^2}$$

Expansion and simplification of this ratio to incorporate material properties of the gas and melt, as well as parameters for the system conditions yields the final expression for diffusive lengthscale used in **Equation 2.11**.

$$L = \frac{V_m}{4\pi R_0^2} = \frac{m_s}{4\pi R_0^2 \rho} = \frac{100 m_b}{4\pi R_0^2 \rho S_0} = \frac{100 M_m}{4\pi R_0^2 \rho S_0} n$$

$$L = \frac{100 M_m}{4\pi R_0^2 \rho S_0} \cdot \frac{4}{3}\frac{\pi R_0^3 p_0}{R_g T}$$

$$L \Rightarrow \frac{100 M_m p_0}{3 R_g T \rho S_0} \cdot R_0$$

Appendix III - Pre-experimental Calculations

The sequence of calculations completed prior to experimental work with CO_2 bubbles in golden syrup to investigate the plausibility of the study and estimate the expected outcomes. Using known material properties of the syrup and other similar substances, diffusivity and solubility at room temperature (given in **Table 6.1**) are approximated before calculations of the diffusion and bubble rise timescales are carried out to find the accessible range of buoyant Péclet number regimes.

1. System Conditions

For the designed open system experiment, initial conditions are as follows:

Room pressure = 1 bar ≈ 1 atm = 10^5 Pa
Room temperature = 25^{o}C = 298K
CO_2 density = 1.8393 kgm^{-3}
Undiluted golden syrup density = 1437.59 kgm^{-3}
Undiluted golden syrup viscosity = 77.55 Pa.s

The two missing parameters for the calculation of the diffusive and bubble rise timescales are solubility and diffusivity of CO_2, which can now be estimated from these initial conditions.

2. Solubility

Laws for the solubility of CO_2 in sugar syrups from existing studies *(eg. Vazquez Una et al., 1994)* are unsuitable for use in this work as they are for glucose syrups with significantly different compositions, very diluted syrup mixtures, or occasionally only applicable under higher temperature and pressure conditions.

Therefore the solubility of CO_2 in water is used to approximate its solubility in golden syrup. This is considered valid since golden syrup is diluted to around 20vol.% with pure water and the effects of the predominantly sucrose sugar are thought to be minimal. Given this assumption, 1.5g of CO_2 is soluble in every kilogram of water *(Engineering Tool Box, n.d.)*.

CO_2 Solubility = 1.5x10^{-3} mass fraction
CO_2 Solubility = 6.148x10^{-4} mole fraction

To account for the fact that only 20% of the golden syrup is water, these values for CO_2 solubility in water are divided by five to give a better estimate for the gas solubility in the syrup.

CO_2 Solubility = 3x10^{-4} mass fraction
CO_2 Solubility = 1.2295x10^{-4} mole fraction

The value of solubility in weight percent (0.03wt.%) is used in all further pre-experimental calculations **(Table 6.1)** as well as the post-experimental analysis completed in **Chapter 6**.

3. Diffusion Coefficient

The diffusion coefficient, D of CO_2 in carbonated drinks containing a sugar syrup solution has previously been estimated *(Lv et al., 2018)*. In club soda and colas at room temperature and pressure, D has a value in the order of 1.73x10^{-9}m^{2}s^{-1}. A mean value of 1.535x10^{-9}m^{2}s^{-1} from drinks containing different sugar syrups could be used, however the concentration of syrup in these drinks is around 10% by volume, significantly less than in golden syrup.

Therefore, a similar approximation to solubility is completed, using the diffusion coefficient of CO_2 in water instead of a sugar syrup. Given this, D can be calculated from,

$$\log|D| = -4.410 + \frac{773.8}{T} - \left(\frac{506.4}{T}\right)^2$$

where D is given in cm^2s^{-1} and T in Kelvin *(Cadogan et al., 2014)*. Using this, the value of diffusion coefficient calculated and used in further pre-experimental calculations is $1.9903x10^{-9}m^2s^{-1}$. This value is also used in subsequent analysis of experimental results in **Chapter 6**.

4. Bubble Rise Timescale

Using the Hadamard-Rybczynski equation **(Eq.2.15)**, the terminal rise velocity of different sized bubbles is estimated. From then, the bubble rise timescale for the CO_2 bubble to rise the height of the 50cm glass cylinder used in the experiments is estimated **(Eq:2.2.2.2)**. These estimations show that the timescale of bubble rise will quite slow enough and will therefore be monitorable by eye or time-lapse photography.

Tube Height m	0.5	0.5	0.5	0.5	0.5
Initial Bubble Radius mm	0.1	0.5	1.0	5.0	10
Bubble Rise Velocity ms^{-1}	$1.21x10^{-6}$	$3.03x10^{-5}$	$1.21x10^{-4}$	$3.03x10^{-3}$	$1.21x10^{-2}$
Bubble Rise Timescale s	$4.13x10^{5}$	$1.65x10^{4}$	$4.13x10^{3}$	$1.65x10^{2}$	$4.13x10^{1}$

5. Diffusion Timescale

Using **Equation 2.12**, the timescale for diffusion of CO_2 from the bubble into the syrup is estimated. For this estimation, the standard conditions are used in the calculation of the diffusive length, L. This shows the timescale of diffusion is fairly long, and in all cases, longer than the bubble rise timescale. As a result, bubbles will not undergo complete resorption but some change in the radius may still be evident and measurable.

Initial Bubble Radius mm	0.1	0.5	1.0	5.0	10
Diffusive Length $x10^7$ m	3.83	3.83	3.83	3.83	3.83
Diffusion Timescale m^2s^{-1}	$1.92x10^{8}$	$4.81x10^{9}$	$1.92x10^{10}$	$4.81x10^{11}$	$1.92x10^{12}$

6. Reynolds Number Estimates

Stokes number is calculated for each bubble size to show that in all cases, the system lies in the low-Reynolds number, viscous dominated regime where bubbles will remain spherical.

Initial Bubble Radius mm	0.1	0.5	1.0	5.0	10
Bubble Rise Velocity ms^{-1}	$1.21x10^{-6}$	$1.21x10^{-5}$	$1.21x10^{-4}$	$1.21x10^{-3}$	$1.21x10^{-2}$
Reynolds Number	$2.2x10^{-9}$	$2.8x10^{-7}$	$2.2x10^{-6}$	$2.8x10^{-4}$	$2.2x10^{-3}$

7. Buoyant Péclet Number Estimates

Finally, using **Equation 2.18**, values of buoyant Péclet number are calculated for each bubble system. These range over several orders of magnitude showing that various orders of Pe_b can be tested by varying the bubble radius between 0.1 and 10 mm.

Initial Bubble Radius mm	0.1	0.5	1.0	5.0	10
Bubble Rise Timescale s	$4.13x10^5$	$1.65x10^4$	$4.13x10^3$	$1.65x10^4$	$4.13x10^1$
Diffusion Timescale s	$1.92x10^8$	$4.81x10^8$	$1.92x10^{10}$	$4.81x10^8$	$4.81x10^8$
Buoyant Péclet Number	$4.7x10^2$	$2.9x10^5$	$4.7x10^6$	$2.9x10^9$	$4.7x10^{10}$

Appendix III - Complete Experimental Results

Table containing data from the ten decoupled bubble experiments completed with bubbles of CO_2 in golden syrup used to plot figures in **Section 6.1.3**. Bubble radii measurements complete with positive and negative estimates of error from measurement are given alongside both the time and distance travelled by the bubble at each point. The file number of each image used to take a bubble radius measurement are also listed.

File Number	Time s	Rise Distance mm	Bubble Radius mm	+ve Error mm	−ve Error mm
Bubble Test 1 - Pe_b=2.2x10^8					
7148	0	0	1.56	0.170	0.144
7149	20	4	1.56	0.174	0.140
7150	40	8	1.55	0.174	0.138
7151	60	12	1.53	0.169	0.137
7152	80	15	1.54	0.172	0.137
7153	100	19	1.59	0.178	0.142
7154	120	23	1.57	0.174	0.141
7155	140	27	1.54	0.172	0.137
7156	160	31	1.50	0.168	0.133
7157	180	35	1.55	0.173	0.139
7158	200	38	1.53	0.171	0.137
7159	220	42	1.52	0.169	0.136
7160	240	46	1.58	0.176	0.142
7161	260	50	1.54	0.172	0.137
7162	280	54	1.52	0.181	0.128
7163	300	58	1.47	0.164	0.131
7164	320	62	1.51	0.168	0.136
7165	340	65	1.47	0.164	0.131
7166	360	69	1.49	0.166	0.133
7167	380	73	1.46	0.163	0.131
7168	410	79	1.46	0.191	0.117
7169	440	85	1.50	0.167	0.134
7170	470	90	1.48	0.164	0.132
7171	500	96	1.42	0.159	0.128
7172	530	102	1.47	0.164	0.133
7173	560	108	1.45	0.161	0.131
7174	590	114	1.43	0.167	0.123
7175	620	119	1.49	0.165	0.134
7176	650	125	1.48	0.164	0.133
7177	680	131	1.45	0.161	0.130
7178	710	137	1.45	0.161	0.130
7179	740	142	1.49	0.164	0.134
7180	770	148	1.39	0.156	0.123
7181	800	154	1.45	0.161	0.130
7182	830	160	1.43	0.160	0.128
7183	860	165	1.52	0.169	0.137
7184	890	171	1.45	0.161	0.130
7185	920	177	1.40	0.159	0.123
7186	950	183	1.40	0.161	0.122
7187	980	189	1.38	0.163	0.118
7188	1010	194	1.39	0.158	0.121
7189	1040	200	1.35	0.161	0.114

File Number	Time s	Rise Distance mm	Bubble Radius mm	+ve Error mm	−ve Error mm
7190	1070	206	1.33	0.151	0.117
7191	1100	212	1.29	0.144	0.115
7192	1130	217	1.39	0.155	0.124
7193	1160	223	1.34	0.150	0.119
7194	1190	229	1.28	0.138	0.119
Bubble Test 2 - Pe_b=4.7x10^8					
7195	0	0	2.01	0.233	0.175
7196	30	8	2.02	0.222	0.185
7197	60	15	2.00	0.229	0.176
7198	90	23	2.10	0.230	0.191
7199	120	31	1.99	0.219	0.181
7200	150	38	1.92	0.210	0.176
7201	180	46	2.03	0.222	0.185
7202	210	54	1.90	0.207	0.174
7203	240	61	1.94	0.214	0.176
7204	270	69	1.69	0.187	0.153
7205	300	76	1.98	0.217	0.180
7206	330	84	1.92	0.211	0.175
7207	360	92	1.91	0.215	0.170
7208	390	99	1.87	0.206	0.170
7209	420	107	1.89	0.208	0.171
7210	450	115	1.83	0.202	0.167
7211	480	122	1.83	0.198	0.168
7212	510	130	1.83	0.207	0.162
7213	540	138	1.87	0.202	0.173
7214	570	145	1.73	0.191	0.156
7215	600	153	1.76	0.193	0.160
7216	630	161	1.78	0.195	0.162
7217	660	168	1.74	0.192	0.158
7218	690	176	1.78	0.202	0.158
7219	720	183	1.86	0.205	0.169
7220	750	191	1.75	0.202	0.153
7221	780	199	1.56	0.178	0.138
7222	810	206	1.62	0.185	0.142
7223	840	214	1.53	0.173	0.136
7224	870	222	1.48	0.170	0.129
7225	900	229	1.47	0.169	0.129
7226	930	237	1.42	0.166	0.123
Bubble Test 3 - Pe_b=4.5x10^8					
7232	0	0	1.99	0.213	0.185
7233	4	1	2.04	0.217	0.192
7234	49	12	1.95	0.209	0.181
7235	64	16	1.99	0.212	0.186
7236	109	28	1.91	0.204	0.180
7237	124	32	1.94	0.208	0.181
7238	169	43	1.96	0.209	0.184
7239	184	47	1.92	0.205	0.180
7240	229	58	1.91	0.202	0.180
7241	244	62	1.94	0.207	0.182
7242	289	74	1.88	0.200	0.176

File Number	Time s	Rise Distance mm	Bubble Radius mm	+ve Error mm	−ve Error mm
7243	304	77	2.17	0.231	0.203
7244	349	89	1.92	0.203	0.181
7245	364	93	1.87	0.199	0.175
7246	409	104	1.89	0.203	0.177
7247	424	108	1.80	0.193	0.167
7248	469	119	1.88	0.201	0.175
7249	484	123	1.82	0.192	0.172
7250	529	135	1.79	0.191	0.167
7251	544	139	1.80	0.193	0.168
7252	589	150	1.81	0.196	0.167
Bubble Test 4 - Pe_b=1.4x10^8					
7253	0	0	1.35	0.148	0.123
7254	45	5	1.44	0.154	0.134
7255	50	5	1.37	0.149	0.126
7256	105	11	1.35	0.147	0.124
7257	120	12	1.33	0.144	0.123
7263	300	30	1.31	0.144	0.119
7265	360	37	1.32	0.143	0.121
7269	480	49	1.33	0.143	0.123
7273	726	74	1.31	0.141	0.121
7277	846	86	1.28	0.140	0.117
7279	906	92	1.23	0.136	0.111
7283	1026	104	1.29	0.140	0.118
7284	1307	133	1.30	0.143	0.119
7287	1382	140	1.20	0.134	0.109
7291	1502	153	1.24	0.134	0.114
7295	1622	165	1.25	0.136	0.115
7299	1742	177	1.18	0.132	0.106
7303	1862	189	1.15	0.126	0.105
7307	1979	201	1.08	0.122	0.096
Bubble Test 5 - Pe_b=1.6x10^8					
7308	0	0	1.40	0.157	0.125
7309	15	2	1.36	0.149	0.125
7313	135	14	1.37	0.148	0.125
7317	255	26	1.33	0.145	0.122
7321	375	38	1.38	0.150	0.127
7325	495	51	1.32	0.144	0.121
7326	540	55	1.36	0.152	0.122
7329	672	69	1.40	0.152	0.129
7332	777	79	1.38	0.149	0.127
7336	897	92	1.37	0.148	0.126
7340	1017	104	1.32	0.144	0.121
7344	1137	116	1.29	0.140	0.119
7347	1212	124	1.31	0.141	0.122
7348	1276	131	1.32	0.145	0.121
7352	1396	143	1.25	0.138	0.112
7356	1516	155	1.21	0.131	0.111
7360	1636	167	1.23	0.135	0.112
7365	1816	186	1.19	0.133	0.106
7368	1916	196	1.20	0.131	0.111

File Number	Time s	Rise Distance mm	Bubble Radius mm	+ve Error mm	−ve Error mm
Bubble Test 6 - Pe_b=8.7x10^7					
7374	0	0	1.15	0.126	0.104
7375	44	2	1.12	0.127	0.099
7376	48	2	1.13	0.127	0.099
7377	66	3	1.13	0.129	0.098
7381	180	9	1.15	0.131	0.100
7385	300	15	1.09	0.123	0.095
7389	420	21	1.03	0.119	0.089
7393	540	27	1.09	0.125	0.094
7397	660	32	1.11	0.127	0.097
7401	780	38	1.05	0.120	0.091
7405	900	44	1.10	0.125	0.095
7408	1005	49	1.05	0.121	0.091
7409	1069	53	1.02	0.116	0.089
7414	1204	59	1.03	0.117	0.090
7418	1324	65	1.02	0.116	0.090
7422	1444	71	1.00	0.113	0.087
7426	1564	77	1.07	0.123	0.093
7430	1684	83	0.96	0.111	0.083
7434	1804	89	1.03	0.118	0.090
7436	1921	94	1.00	0.114	0.087
7440	2161	106	1.05	0.119	0.092
7444	2401	118	1.02	0.116	0.089
7448	2641	130	0.99	0.114	0.085
7452	2881	142	1.05	0.120	0.092
7456	3121	153	1.02	0.117	0.088
7460	3361	165	0.98	0.112	0.085
7464	3601	177	0.97	0.111	0.085
7468	3841	189	0.99	0.114	0.086
7472	4081	201	0.97	0.112	0.083
7476	4321	212	0.94	0.109	0.081
7480	4561	224	1.00	0.118	0.086
7484	4801	236	0.96	0.114	0.081
Bubble Test 7 - Pe_b=2.6x10^8					
7502	0	0	1.66	0.187	0.146
7503	22	5	1.57	0.177	0.138
7504	74	15	1.54	0.172	0.138
7506	179	37	1.52	0.171	0.136
7508	254	53	1.47	0.165	0.131
7510	359	75	1.50	0.170	0.132
7512	434	90	1.44	0.163	0.128
7514	539	112	1.49	0.168	0.133
7516	614	128	1.51	0.167	0.136
7518	719	150	1.49	0.167	0.132
7520	794	165	1.47	0.164	0.132
7522	908	189	1.49	0.168	0.133
7524	983	205	1.46	0.163	0.131
7526	1088	227	1.47	0.164	0.131
7528	1163	242	1.45	0.164	0.127
7529	1253	261	1.44	0.166	0.125

File Number	Time s	Rise Distance mm	Bubble Radius mm	+ve Error mm	−ve Error mm
7530	1328	277	1.41	0.164	0.121
7532	1343	280	1.36	0.165	0.114
Bubble Test 8 - Pe_b=6.3x10^7					
7501	0	0	1.03	0.139	0.080
7503	60	5	1.01	0.118	0.087
7504	112	9	1.03	0.120	0.088
7505	165	13	0.99	0.116	0.084
7507	240	19	1.04	0.122	0.089
7510	397	31	1.03	0.123	0.087
7514	577	45	1.02	0.122	0.085
7518	757	59	0.99	0.118	0.082
7521	885	69	0.94	0.113	0.078
7524	1021	79	0.99	0.118	0.082
7527	1178	92	0.97	0.115	0.082
7531	1358	106	1.00	0.118	0.084
7535	1538	120	0.97	0.114	0.081
7539	1718	134	0.97	0.116	0.081
7541	1793	139	1.00	0.120	0.083
7543	2024	157	0.99	0.117	0.084
7546	2204	171	0.95	0.114	0.079
7549	2384	185	0.97	0.116	0.081
7552	2564	199	0.96	0.114	0.081
7555	2744	213	0.94	0.109	0.080
7559	2984	232	0.99	0.116	0.083
7561	3104	241	0.95	0.114	0.079
7563	3224	251	0.93	0.112	0.078
7564	3345	260	0.96	0.117	0.079
Bubble Test 9 - Pe_b=4.4x10^7					
7501	0	0	0.91	0.111	0.075
7502	38	2	0.90	0.110	0.074
7503	60	3	0.89	0.107	0.074
7506	217	11	0.90	0.108	0.076
7508	232	12	0.90	0.108	0.074
7510	397	20	0.90	0.106	0.075
7515	600	31	0.85	0.102	0.070
7520	832	43	0.89	0.107	0.074
7526	1126	58	0.86	0.104	0.070
7531	1358	70	0.85	0.103	0.070
7536	1561	80	0.89	0.107	0.074
7541	1793	92	0.87	0.105	0.072
7542	1972	101	0.88	0.105	0.072
7547	2264	116	0.84	0.101	0.069
7551	2504	128	0.88	0.105	0.072
7555	2744	141	0.83	0.102	0.067
7559	2984	153	0.87	0.106	0.070
7563	3224	165	0.86	0.104	0.070
7566	3464	178	0.84	0.101	0.069
7570	3704	190	0.82	0.100	0.067
7574	3944	202	0.86	0.104	0.070
7578	4184	215	0.86	0.102	0.072

File Number	Time s	Rise Distance mm	Bubble Radius mm	+ve Error mm	−ve Error mm
7581	4316	221	0.84	0.103	0.069
7582	4616	237	0.85	0.104	0.069
7583	4916	252	0.87	0.105	0.071
7584	5216	268	0.86	0.103	0.071
7585	5516	283	0.85	0.103	0.071
Bubble Test 10 - Pe_b=6.8x10^6					
7501	0	0	0.49	0.068	0.035
7502	38	1	0.47	0.065	0.033
7503	60	1	0.50	0.067	0.036
7504	112	2	0.49	0.063	0.037
7505	165	3	0.44	0.058	0.032
7508	292	6	0.46	0.061	0.033
7509	345	7	0.48	0.062	0.035
7510	397	8	0.48	0.062	0.036
7515	600	12	0.46	0.060	0.034
7521	885	17	0.49	0.064	0.036
7528	1201	23	0.48	0.064	0.035
7534	1486	29	0.45	0.060	0.032
7541	1793	35	0.48	0.063	0.036
7544	2084	40	0.46	0.060	0.034
7549	2384	46	0.43	0.057	0.031
7554	2684	52	0.47	0.061	0.035
7559	2984	58	0.42	0.057	0.030
7564	3344	65	0.41	0.055	0.029
7569	3644	70	0.41	0.055	0.029
7574	3944	76	0.44	0.058	0.032
7579	4244	82	0.42	0.056	0.030
7582	4604	89	0.41	0.055	0.029
7583	4904	95	0.44	0.059	0.031
7584	5204	101	0.40	0.055	0.027
7585	5504	106	0.44	0.059	0.032
7586	5804	112	0.40	0.054	0.027
7587	6104	118	0.39	0.052	0.027